2018

Design of High Efficiency Brushless Permanent Magnet Machines and Driver System

Chengyuan He
University of Central Florida

DESIGN OF HIGH-EFFICIENCY BRUSHLESS PERMANENT-MAGNET MACHINES AND DRIVER SYSTEM

by

CHENGYUAN HE
M.S. Wright State University, 2013

A dissertation submitted in partial fulfilment of the requirements
for the degree of Doctor of Philosophy
in the Department of Electrical and Computer Engineering
in the College of Engineering and Computer Science
at the University of Central Florida
Orlando, Florida

Fall Term
2018

Major Professor: Lei Wei

ABSTRACT

In recent years, renewable green energy has increased the demand associated with the development of high efficiency electrical permanent magnet synchronous machinery. The electrical motors consume more than half of all electrical energy in the state according to the U.S. Department of Energy. Therefore, designing a high-efficiency energy conversion device and its control system becomes critical. Permanent magnet synchronous motor (PMSM) and Permanent mag-net synchronous generator (PMSG) can be such energy conversion device. This dissertation is concerned with the high-efficiency permanent magnet synchronous machinery, and their control system design.

The dissertation first talk about the design method of high- efficiency electrical machinery. The advantage of the design method is that it can increase the high load capacity at no cost of increasing the total machine size. A much smaller torque angle δ than that in the traditional design at relating load is selected, which is between about 2 degrees and about 10 degrees. The most import part of the design is to determine the air-gap and permanent magnet size. According to the design method relating to the much smaller torque angle, which will result in the larger air-gap size and larger magnet thickness. The larger air-gap size contributes to reducing the windage loss and noise level. The increase magnet thickness helps to avoid demagnetization. Both them contribute to high efficiency and high overload capability. Based on the design method, all the parameters will be related to the torque angle, working point of a permanent magnet, and the permanent magnet embrace, which is easier for the designer to make a new design.

The control methods of the permanent magnet machinery are introduced. There is two class of brush-less PM motor control: AC and DC. The design requirements are totally different, and this is related to the back-EMF waveform and the rotor-position sensing. For DC control, the back

EMF is trapezoidal and hall-sensor board is used to detect the switching positions, substantial field weakening is not required. For AC control, the back EMF is sinusoidal, and an encoder or resolver is used to get rotor position. In order to avoid to use encoder or resolver, sensor-less control such as sliding mode observer algorithm can be used.

A permanent magnet brushless DC motor for electric impact wrench and a Surface permanent magnet synchronous generator (SPMSG) have been designed with good performance and high-efficiency base on the design method. Using brush-less DC motor (BLDC) instead of brushed DC motor for electric impact wrench has been a world worldwide trend because of its high reliability, good control performance, small size, and environmental protection. Maxwell 2D model is built to optimize the design and the control board is designed using Altium Designer. Bother the motor and control board have been fabricated and tested to verify the design.

A 2kw high-efficiency alternator system and its control board system are also designed, analyzed and fabricated applying to the truck auxiliary power unit (APU). The alternator system has two stages. The first stage is that the alternator three-phase outputs are connected to the three-phase active rectifier to get 48V DC. An advanced Sliding model control (SMO) is used to get an alternator position. The buck is used for the second stage to get 14V DC output. The whole system efficiency is much higher than the traditional system using induction motor.

This thesis work is dedicated to my parents, Chunnan Zhu and Cuanghui He, who have always loved me unconditionally and taught me to work hard deligently. This work is also dedicated to my advisor Lei Wei and Thomas Wu for their constant support and encouragement during the challenges of my graduate life.

ACKNOWLEDGMENTS

I would like to express my sincere gratitude to my advisors Lei Wei and Thomas Wu, for their con-tinuous support of my Ph.D study and related research. Their guidance helped me in all the time of research and writing of this thesis. Moreover, I acknowledge support from advanced electrical machinery lab team.

Besides my advisors, I would like to thank the rest of my thesis committees: Dr. Kalpathy Sundaram, Dr. Qun Zhou, Dr. Yier Jin, Dr. Shengli Zou, for their insightful comments and encouragement.

I also would like to take this opportunity to thank Dr. Louis Chow, Dr. WeiWu, Dr. Zhigang Gao and my master degree adviser Dr. Marian K. Kazimierczuk for their guidance on my research. Additionally, I thank my lab mates, Xiaoyi Zhao, Anthony Camarano, and many other friends for the discussions and for all the fun we have had in the last few years.

Eventually, I would like to thank my parents and other family members for their selfless dedication and sacrifices.

TABLE OF CONTENTS

LIST OF FIGURES

LIST OF TABLES

CHAPTER 1: INTRODUCTION

Permanent magnet (PM) motor and generator [17] [51] [5] [28] [83] [33] have been widely used in industry by demand for increased functionality, precision, increased energy efficiency and better utilization of primary energy sources. The development of ferrite magnets, Samarium-Cobalt magnets (in the late 1960s) and Neodymium-Iron-Boron magnets [59] are the most important driver of application of brushless PM machines. Soft iron materials [4] have also made significant contribution in the development of brush-less PM machines. Thin gauges, improved chemical composition, heat-treatment and improved core-plate insulation are used to reduce loose in electrical lamination steels. High-strength non-magnetic materials such as inconel and carbon-fiber make big contribution in the design of high-speed brush-less PM machines [99] [65] [3], where they are used in retaining sleeves that extend the range of operation to much higher speed. Due to the developments of power electric, the PM machines control systems [79] [22] [9] become more efficiency, reliability and cheaper, which permit a wider range of affordable application. These technical development made the PM machines become a trend in industry.

Brushless PM machines generally fall into two classification : AC and DC. Both AC and DC PM machines can be design as Interior permanent magnet (IPM) machine or Surface permanent magnet (SPM) machine. There are different requirements when designing them, and this is related to the back-Electromotive Force (EMF) waveform and rotor-position sensing. For DC PM machine [68] [71] [45] [69] [54], the back EMF is trapezoidal and low-resolution shaft-position sensor is used to synchronize the switching of the drive transistors with the rotor position, substantial field weakening is not required. For AC PM machine [73] [72] [27] [105] [7], the back EMF is sinusoidal, and encoder or resolver [92] [13] [1] is used to get rotor position. The following are the characteristics of DC PM machine operation:

- concentrated windings and full pitched;
- trapezoidal back EMF;
- hall sensor board is used to detect the correct switching position;
- higher power density;
- tolerating some torque ripple and no extra field weak required;
- suitable for power drives;

The following are the characteristic of AC PM machine operation:

- distributed and fractional-slot winding;
- sinusoidal back EMF;
- smooth operation and extended field weaken;
- shaft encoder or resolver to get the position;
- suitable for servo derives, electric vehicles drives requiring extra field-weaken capabilities at high speed.

SPM and IPM are two basic topologies for the rotor. For SPM, the direct- and quadrature-axes inductance are the same, there is essentially no reluctance torque generated by SPM machines, although flux-weaking mode is possible if appropriately designed. For IPM machines, they have q-axis saliency that comes from the shape of steel lamination, which called reluctance torque. The total torque is the combination of reluctance torque and magnet torque. The air-gap of IPM is usually designed smaller then that of a SPM, which tends to increase the flux per pole, the

reluctance torque and the inductance.If an extended field-weakening rang is required, then the IPM should be used.

Permanent magnet synchronous machines have no brushes, no slip-rings, and no mechanical commutator, and they use permanent magnets to replace the rotor winding which leads to higher efficiency compared to other machines. Permanetn magnet synchronous motor (PMSM) can maintain a high efficiency when its output power varies from 50-120% of the rated power. The following are the advantages of PMSM :

- high efficiency and power density;
- small output torque;
- reliable at high speed;
- advanced control topology;
- lighter weight and good heat performance.

Researchers try to develop new methods to increase the efficiency of PMSM, reduce the harmonic and torque ripple, making the machines have better and better performance.

For Electric tool application, brush-less DC motor (BLDC) is a most suitable choice. The motors should be tolerate some torque ripple and do not require extra field weakening at higher speed. The hall sensor board is used to get the correct current switching position. For example BLDC designed for the electric impact wrench requires high reliability, good control performance, small size, less bolting time, low cost and easy mass industrial production. An interior permanent magnet synchronous motor with concentrated winding has large torque to volume ration and high efficiency, so It is suitable for battery-powered impact wrench [84] [91] [10].

High-efficiency alternator system is commonly equipped with the heavy-duty truck. The three-phase outputs from the alternator are processed through a three-phase rectifier [107] [95] [47] to get the DC bus voltage. DC bus output will be used to charge the auxiliary power unit and battery whenever the truck is operating. There are two stages outputs in our alternator system: 48V DC and 14V DC. The 48V DC is directly got from the three-phase active rectifier, and 14V DC is obtained through a buck converter. The battery is charged by 48V DC, and some 14V devices are powered by 14V DC. High current is required if we want to charge the battery quickly, which require good heat dissipation performance of the converter board. The PCB structure using PCB board, aluminum board, and copper bars is designed to satisfy the requirement. The Sliding model control (SMO) method is used to get the alternator shaft position. The disadvantage of SMO can be avoided because the alternator doesn't need to start by itself, otherwise, at the low speed, we need to use the open loop. The alternator is controlled by FOC [100] [96] [97] [26], and the DC output is connected to the buck converter. In order to get a fast pulse-by-pulse response and good over-current protection, the peak current control [30] [11] [12] [20] is applied to control buck converter.

Dissertation Organization

Chapter two will introduce the key design method of permanent magnet machinery. The motor dynamic modeling and control method will be presented in Chapter Three. Base on Chapter Two and Chapter Three, Chapter Four will present the Brush-less dc motors design and control system applying to the electric impact wrench. Chapter Five will focus on the high-efficiency alternator design and the control system, which is equipped to the heavy-duty trucks. In Chapter Six, the contribution of this dissertation and research conclusion will be highlighted.

CHAPTER 2: ADVANCED DESIGN METHODS OF BRUSH-LESS PERMANENT MAGNET MACHINES [1]

Introduction

Permanetn magnet synchronous motor (PMSM) is a new type of motor and has many advantages in comparing with the traditional machines with electromagnetic excitation. It has small inertia moment, large power density, high efficiency, and high reliability, therefore is very suitable for the high-performance application [75] [60]. Due to no excitation winding, PMSM significantly reduces the volume, weight, winding losses and electric heating and it saves energy. PMSM is gradually replacing dc motor and induction motor [110] [101] [102].

This chapter is concerned with key design methodology, which has to do with the configuration, the size of the stator, rotor, permanent magnet, winding, shaft, housing, etc. Some popular materials and their characteristics for machine design applications are also presented. Winding configuration and how to determine the coil pith and winding sequence will be discussed. The different types of magnetization [35] [36] of the Permanent magnet (PM) and performances will be presented. At last, the power losses of PMSM will be introduced.

Key Design Procedure of PMSM

When starting to design the PMSM, it is the several important decisions must be made at the early stage. The following list covers most aspects of most cases:

[1] The content in this chapter was partly published at *ICEM, 2016 XXII International Conference* [38], *IECON* 2017 [41] and journal Energies [40].

- decide the configuration of the PM machines and Its control;
- select numbers of phases, poles, and slots;
- estimate the volume of the machine;
- choose materials;
- design slot;
- design permanent magnet;
- design rotor, shaft, and housing;
- winding configuration.

Firstly, the slots, poles number, control topology and the materials will be decided; then the initial size of all parts of the machine will be obtained using our PMSM design method based on the rotating speed, power lever, maximum tolerance and cooling type.

Finite element analysis (FEA) will be used to confirm the initial design and analyze electromagnetic variation and distribution, which can provide a detailed analysis of the performance of the design. The obtained result waveforms will be compared with some standard waveforms. The torque and flux density of the machine will also be analyzed. Maxwell 2D FEA will be repeated until optimize parameters are obtained. Comprehensive consideration will be taken when we do optimum design. Also, thermal analysis and mechanical analysis need to be done to make sure the mechanical satisfies the requirements.

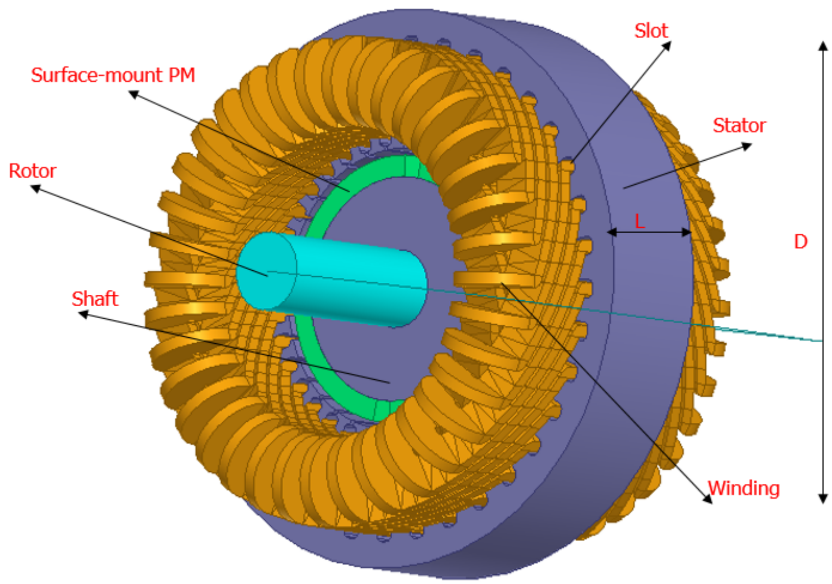

Figure 2.1: 3D structure of the PMSM

Figure 2.1 shows a surface-mounted permanent magnet motor structure including a stator with winding, a rotor with magnets and a shaft.

Drive Configuration

There are two types of brush-less PM motor control: the square-wave drive and the sine-wave drive, which is related to the back-EMF waveform and the rotor position sensing, and their characteristics are summarized here.

Square-wave Drive

The motor should have a trapezoid EMF waveform, and this tends toward the use of concentrated windings. Hall-sensor board is used to detect the switching positions; substantial field weakening is not required. Chopping regulates the current. Phase advance can be used to increase speed but at the expense of torque ripple and power factor. The following are the characteristics of DC PM machine operation:

- concentrated windings and full pitched;
- trapezoidal back Electromotive Force (EMF);
- hall sensor board is used to detect the correct switching position;
- higher power density;
- tolerating some torque ripple and no extra field weakening required;
- suitable for power drives.

Sine-wave Drive

Ideally, the current and EMF of this kind of PM machines are both sinusoidal. Continuous position feedback using encoder or resolver is assumed, although sensor-less control is also available. It can be designed with distributed or concentrated winding with integral or fractional slots/pole. The following are the advantages of PMSM :

- high efficiency and power density;
- small output torque;

- reliable at high speed;
- advanced control topology;
- lighter weight and good heat performance.

Numbers of Slots and Poles

The combinations of poles number and slots number of a PM motor [14] [93] have a profound effect not only on the winding layout but also on the space-harmonics of the resulting ampere-conductor distribution and the peak value of cogging torque waveform, thus choosing poles and slots number are very critical for motor design.

The least common multiplier (LCM) between the slot number and the pole number and the greatest common divider (GCD) between the slot and pole number are two factors, which can be used to find the combination of the number of poles and slots. The value of the LCM traduces the value of the first harmonic of the cogging torque, so the higher the LCM value is, the lower the cogging torque. The GCD value illustrates the balanced radial forces applied to the rotor, the smaller the GCD value is, the lesser the cogging torque will be.

Machine Volume

The stator size is the foundation of the design. We can get the general size of the motor from

$$\frac{D^2L}{T_m} = \varpi_0 T_m = \frac{P_r}{\omega} \tag{2.1}$$

Where D is stator bore diameter, L is stator core length, T_m is related mechanical torque, which is determined by the required output power P_r and the rotor rotational speed ω. ϖ_0 is a coefficient.

The value of ϖ_0 depends on the cooling method. Typically, for air cool , the value of ϖ_0 is around 5-7 $in^3/(ft \cdot lb)$ for $10hp$ output power or less; for water or other liquid cool methods, the value of ϖ_0 is around 2-5 $in^3/(ft \cdot lb)$ for 10 hp output power or less. The better the cooling method, the smaller the motor size. Otherwise, The larger size is required for adequate heat dissipation. The proper size fo the machine can be determined using Eqn. 2.1 based on the design specifications and thermal requirement. For initial design, assuming the diameter-to-axial-length ratio to be close to unity. The diameter of some high-pole-number machinery is much larger than the length, and it will make the machinery move from a long cylindrical shape to disk shape, which means high-pole-number machines' diameter tend to be much higher compared with the axial length. The machinery will be more compact and high-efficiency if high-energy magnets such as Nd-Fe-B and SmCo are used. It is a crude size approximation for radial-flux machines over a wide power range. The flux per pole determines the stator yoke thickness; therefore, the thickness decreases as the pole number increase.

Magnetic Materials

Introduction

There are two types of materials: soft and hard material. Soft materials are easy to magnetize and demagnetize so that they can transfer or store magnetic energy in circuits with AC waveforms. Therefore, Softer materials are widely used as stator and rotor materials. Hard materials are materials which retain their magnetism and are difficult to demagnetize and thus are used as permanent magnets in applications such as PMSM and Permanent magnet synchronous generator (PMSG). The following are the major parameters of magnetic materials :

- relative permeability μ_{rc};

- saturation magnetic flux density B_s;
- Curie temperature T_c and operating temperature T_w;
- resistivity ρ_c;
- eddy-current and hysteresis losses per unit volume P_v;
- bandwidth BW.

PM motor's stator and rotor are made of soft magnetic materials. The relative permeability μ_r of soft magnetic materials is from 1 to 10^5. If the motor working temperature is below $100\,^{\circ}\mathrm{C}$, steels will be chosen in the design. The saturated magnetic flux density of steels is 1.7 Tesla (T). The performance of steels will be reduced when temperature increase, so if machines require high working temperature, Hiperco50 (an iron-vanadium soft magnetic alloy) can be used as the soft magnetic material. The saturation magnetic flux density of Hiperco50 is 2.3T, and it has high DC maximum permeability, low DC coercive force, and low AC core loss.

Neodymium iron boron (NdFeB) and Samarium-cobalt (SmCo) are most popular permanent magnet materials. NdFeB is the strongest rare-earth material, but the Curie and operating temperature of NdFeB are slow, for example, the curl and operating temperature of NdFeB-28 are $310\,^{\circ}\mathrm{C}$ and $150\,^{\circ}\mathrm{C}$ respectively. The performance of it will weaken when the temperature increase. NdFeB will demagnetize when cure temperature reached. SmCo has much higher curl and operating temperature. The price of SmCo is high compared with NdFeB. If a PM motor needs to work under wide temperature, SmCo will be used in the design.

Hysteresis

The magnetization curve [58] [80] [15] [56] is called the hysteresis. It describes the relationship between the magnetic flux density B and the magnetic field density H. A ferromagnetic material remains magnetized after the external field is removed. It is only practically reversible in the process of repeated magnetization and demagnetization. We can see from Fig. 2.2, the $B - H$ curve is a multi-valued function, is nonlinear and exhibits saturation. The shape and size of the $B - H$ curve depend on the properties of the ferromagnetic materials and the magnitude of the applied field H. For hard material, it is difficult to move the magnetic wall, so the hysteresis loop is wide. For soft material, it is easy to move the magnetic wall, so the hysteresis loop is narrow. The $B - H$ loop area is equal to the hysteresis energy loss per volume for one cycle. When the magnitude of the amplitude of the AC component of magnetic flux density is increased, so is the area of the the $B - H$ loop. It will increase hysteresis energy loss. The $B - H$ loop will become wider when the frequency increase due to eddy currents.

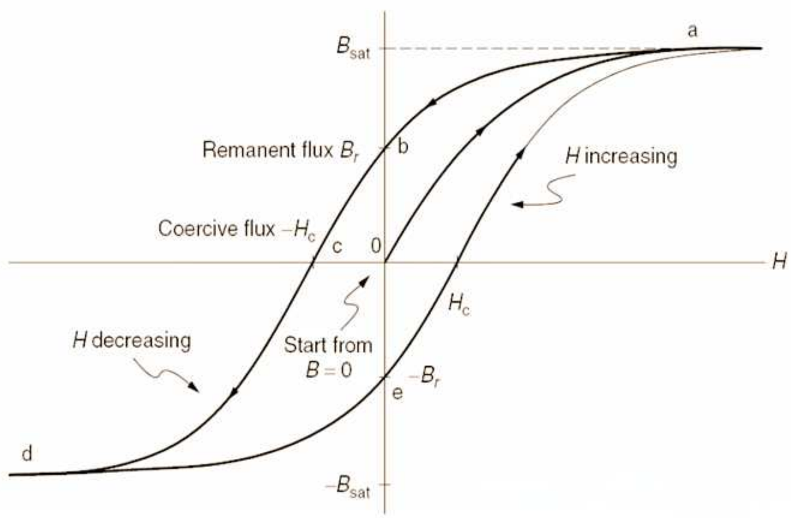

Figure 2.2: Hysteresis loop

Stator Slot and Winding Designing

Before we design the stator slot size, we define slot pitch τ_s as:

$$\tau_s = \frac{\pi D}{N_s} \tag{2.2}$$

where N_s represents the number of the stator slots. Typically, we use the experienced equations to determine the stator slots size. Schematic structural view of the stator slot is shown in Figure 2.3.

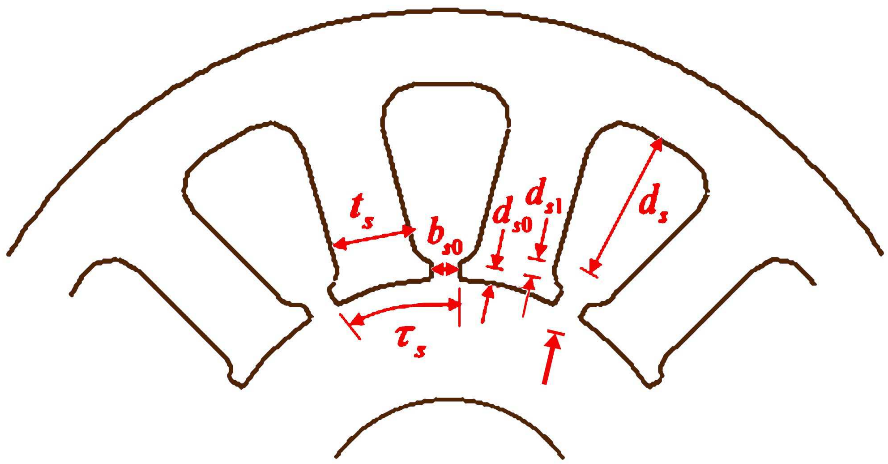

Figure 2.3: 2D structure of the PMSM stator

$$\begin{cases} 0.4\tau_s \leq t_s \leq 0.6\tau_s \\ 3t_s \leq d_s \leq 7t_s \\ b_{s0} \approx (0.1 - 0.5)b_s \\ d_{s0} \approx (0.1 - 0.5)b_s \\ d_{s1} \approx (0.1 - 0.5)b_s \end{cases} \tag{2.3}$$

where $b_s = \tau_s - t_s$.

The fellowing equation is used to determine the rated phase voltage:

$$V_{\Phi,rated} = \sqrt{2}\pi f_e \hat{N}_a \Phi_{g,pk} \approx 4.44 f_e \hat{N}_a \Phi_{g,pk}, \tag{2.4}$$

where f_e is electrical frequency, $\Phi_{g,pk} = \frac{2B_{g,pk}Dl_i}{P}$ is the peak flux of air-gap, $\hat{N}_a = k_w N_a / k_{ls}$ is the effective number of series turns per phase, k_w is winding factor, and number of series turns per phase $N_a = PqN_c/C$. If the number of parallel turns of armature winding $C = 1$, then $N_a = PqN_c$. We add assumed coefficient k_{ls} to compensate for the leakage flux. Finally, the number of turns per coil can be expressed as

$$N_c = \frac{k_{ls} V_{\phi,rated} C}{2\sqrt{2}\pi f_e q k_w B_{g,pk} D l_i}. \tag{2.5}$$

The phase current can be determined regarding current density and slot parameters as

$$I_{p,rated} = \frac{\varphi_s \pi D r_s}{2 N_c N_s} J_s \tag{2.6}$$

where J_s is the current density, N_s is the number of slots, r_s is the ratio of slot width and slot pitch, and φ_s is the slot pitch. We can use the current density equation to choose reasonable slot dimensions. It also provides some restriction of motor design, which is determined by cooling condition and thermal conductivity. The input power is related to phase voltage and phase current of the motor, which can be calculated as

$$P_{in} = 3 V_{\phi,rated} I_{p,rated} \cos\theta. \tag{2.7}$$

Stator Core Design

The flattened view of a motor is shown in Fig. 2.4.

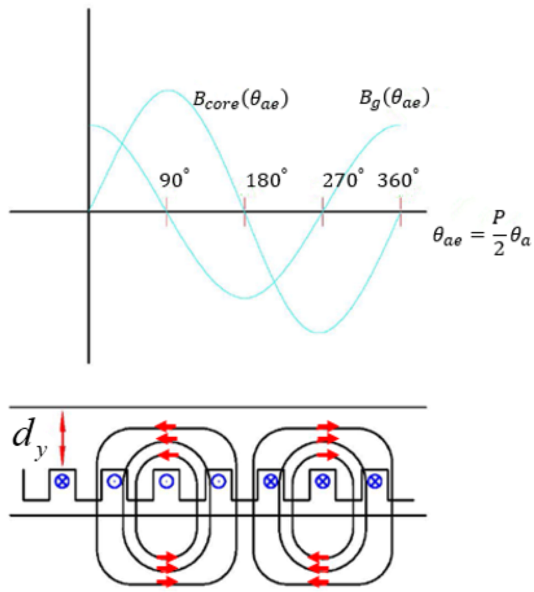

Figure 2.4: Flux density curve and flux of one pole pair

It can be seen that the total flux through the yoke is equal to the flux in the air-gap vier a half pole pitch from the Fig 2.4. Therefore, the flux in the core can be calculated by integrating the air-gap flux.

$$\begin{aligned}
\Phi_{core} &= \Phi_{gap,perhalfpolepitch} \\
&= l_e \int_0^{\pi/N_p} B_g(\theta_a) r_{is} d\theta_a \\
&= \frac{D}{2} l_e \frac{2}{P} \int_0^{\pi/N_p} B_{g,pk} \cos(\theta_{ae}) d_{\theta_{ae}} \\
&\approx \frac{D}{N_p} l_e B_{g_pk}
\end{aligned} \tag{2.8}$$

where l_e is the stator effective length, N_p is number of poles. Then the core flux density can be calculated:

$$B_{core,pk} = \frac{\Phi_{core}}{d_y k_i l_i} = \frac{DB_{g,pk} l_{eff}}{P d_y k_i l_i} \tag{2.9}$$

where d_y is yoke thickness. Assuming the flux density across one stator tooth is constant because the slot pitch is much smaller than pole pitch. The flux through one stator tooth is gained by integrating the air-gap flux over the whole slot pitch. Its value is approximately equal to the peak flux density.

$$\Phi_{tooth} = l_{eff} \int_0^r B_g(\theta_{ae} r_i d\theta_{ae}) \approx B_{g,pk} \tau_s l_{eff} \tag{2.10}$$

where τ_s is slot pitch. The relationship between back iron and tooth flux density can be got after some derivation

$$\frac{B_{core,pk}}{B_{tooth}} = \frac{Dt_s}{P d_y \tau_s} \tag{2.11}$$

Assuming $t_s \approx 0.5\tau_s$, $B_{core} \approx 0.8 B_{tooth}$, the yoke thickness can be expressed as :

$$d_y = \frac{D}{1.6 N_p} \tag{2.12}$$

This equation has physical meaning, it means if we pick up the larger number of poles in the design, yoke thickness will be smaller, we don't need that much yoke thickness to finish the design.

Design of Air-gap and Permanent Magnet

For a multi-pole surface mount rotor as shown in Fig. 2.5.

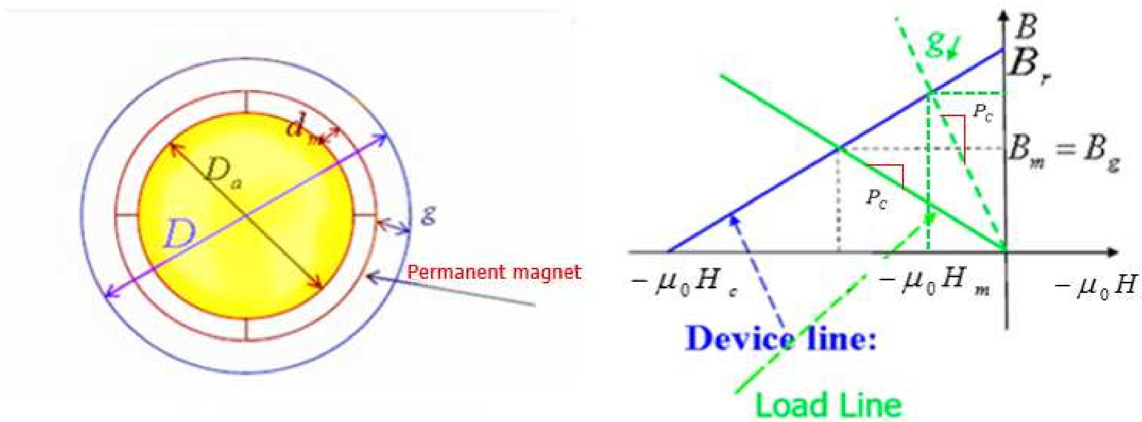

Figure 2.5: Rotor with multi-pole surface-mounted magnets

According to the magnetic circuit analysis:

$$2H_g + 2H_m d_m = 0, \tag{2.13}$$

where H_g is the air gap magnetic field, g is the air gap size, H_m is the PM magnetic field and d_m is the magnetic thickness. We use magnetic flux density B to replace magnetic filed H, than the Eqn. 2.13 becomes $gB_g + \mu_0 H_m d_m = 0$, the relationship between the magnet thickness and air-gap size can be obtained:

$$\frac{d_m}{g} = -\frac{B_m}{\mu_0 H_m} \frac{A_m}{A_g}. \tag{2.14}$$

When designing the magnet and air-gap, a working point for permanent magnetics should be selected. Firstly, we are going to get maximum energy point. B can be got from Fig. 2.5 easily:

$$B = \frac{B_r}{H_c}(H + H_c), \tag{2.15}$$

letting B multiply H, BH equation can be obtained as:

$$BH = \frac{B_r}{H_c}(H + H_c)H. \tag{2.16}$$

In order to get maximum energy point, we get BH derivative:

$$\frac{\partial(BH)}{\partial H} = 0, \tag{2.17}$$

after some derivation, the $(BH)_{max}$ can be got, which is located in $B_m = \frac{B_r}{2}$, $H_m = -\frac{H_c}{2}$. It is in the middle of device line. It can be seen that there are two lines in Fig. 2.5 : device line and load line. Device line equation can be easily got:

$$B_m = (\frac{B_r}{H_c})(H_m + H_c) = \mu_0\mu_r + H_B, \tag{2.18}$$

P_c is called pemeance coefficient, which is equal to:

$$P_c = \frac{d_m}{g}\frac{A_g}{A_m} = \frac{A_g/g}{A_m/d_m} \approx \frac{R_m}{R_g} \approx \frac{\rho_g}{\rho_m}. \tag{2.19}$$

From magnetic circuit:

$$F_m + F_g = 0, \tag{2.20}$$

where $F_m = H_m d_m$, and $F_g = H_g g$, put them to Eqn. 2.20, than we can get $H_g = -\frac{d_m}{g}H_m$, finally, we get:

$$B_g = \mu_0 H_g = -\mu_0\frac{d_m}{H_m}, \tag{2.21}$$

from $\Phi = B_g A_g = B_m A_m$, we get $B_m = B_g\frac{A_g}{A_m}$, replace B_g using Eqn. 2.21, the load line

equation can be obtained:

$$B_m = -\mu_0 \frac{d_m}{g} \frac{A_g}{A_m} H_m = -P_c(\mu_0 H_m). \tag{2.22}$$

We define $B_m = \alpha_m B_r$, $H_m = -(1-\alpha_m)H_c$, where α_m is called working point of permanent magnetics,We can get the maximum energy by choosing $\alpha_m = 0.5$. However, in order to avoid demagnetization and knee effect, we always choose working point higher than 0.5. Now we are going to determine the air-gap magnetic field from PM rotor based on the parallel magnetization magnet.

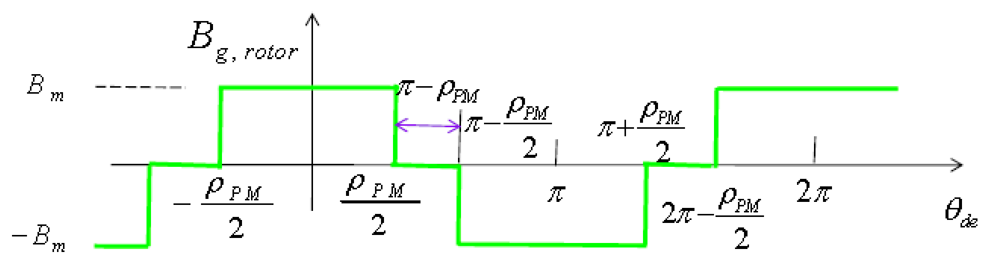

Figure 2.6: The parallel magnetization waveform

Fig. 2.6 shows the parallel magnetization waveform, after doing Fourier expansion, we can get:

$$B_{rh} = \frac{2}{2\pi}\Big[\int_{-\rho_{PM}/2}^{\rho_{PM}/2} B_m \cos(h\theta_{ae})d\theta_{ae} + \int_{\pi-\rho_{PM}/2}^{\pi+\rho_{PM}/2} (-B_m)\cos(h\theta_{ae})d\theta_{ae}\Big] = \frac{4}{\pi}\frac{\sin(h\frac{\rho_{PM}}{2})}{h} B_m \tag{2.23}$$

where ρ_{PM} is the electrical angle of permanent magnet, can be calculated by $\rho_{PM} = e_m\pi$, where e_m represents the embrace of the permanent magnet. Its value varies from 0.5 to 1. It affects the air-gap magnetic field, peak flux density of the teeth and yoke,cogging torque,etc, k_{ph} is pitch factor for the h^{th} harmonic, $k_{ph} = \sin\left(h\frac{\rho_{PM}}{2}\right)$. The peak air gap magnetic field $B_{r,pk}$ can be

approximately calculated by:

$$B_{r,pk} \approx \frac{4}{\pi} \sin\big(\frac{\rho_{PM}}{2}\big) B_m. \tag{2.24}$$

Typically, power angle θ is approximate 0 at full-load for the design of PMSM. The torque angle δ for PMSM is usually designed to be in the range of 15-30 degree. The phase diagram and relationship between torque angle and the output power are shown in Fig. 2.7.

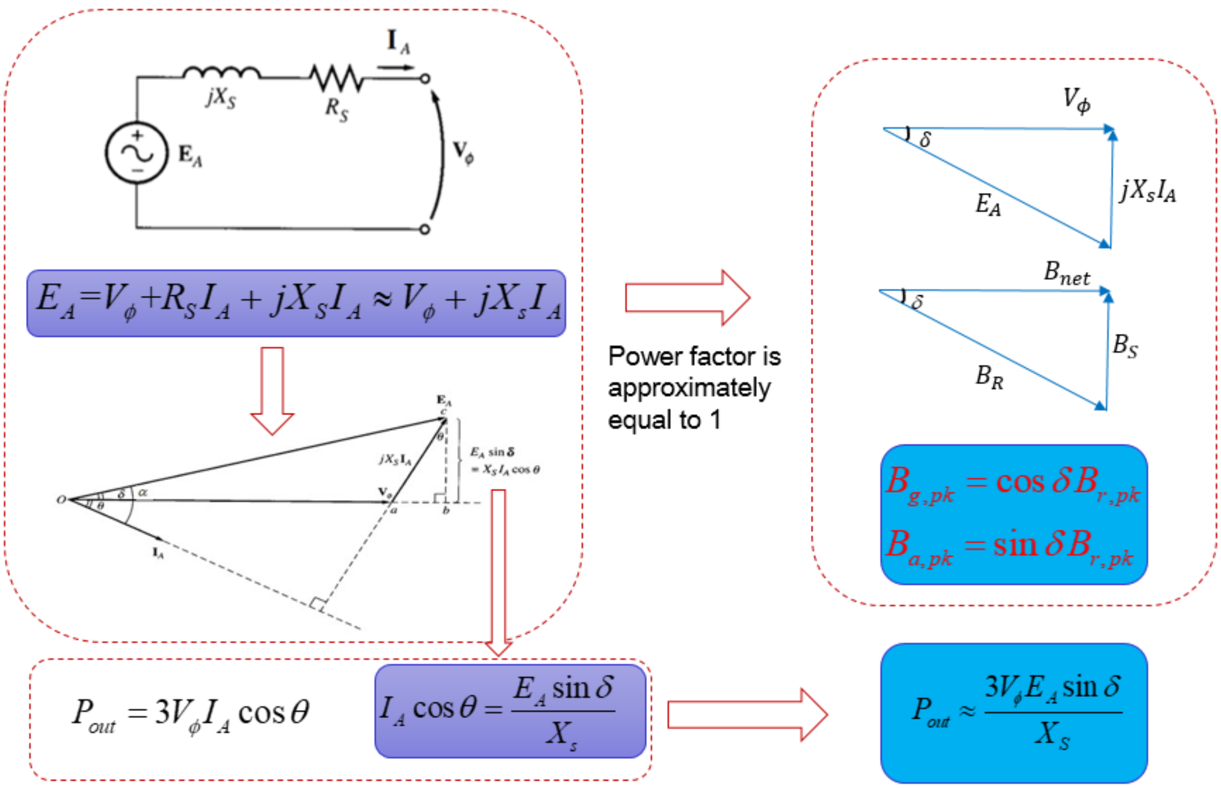

Figure 2.7: The phase diagram and relationship between torque angle and the output power for SPMSM

Normally, R_s is very small, we can neglect, then the phase A inducted back EMF $E_A \approx= V_\phi + jX_s I_A$. When selecting power factor is approximately to one. The peak value of the net magnetic

filed $B_{g,pk}$ and peak winding magnetic field $B_{a,pk}$ are defined:

$$B_{g,pk} = B_{r,pk} \cos \delta B_{a.pk} = B_{r,pk} \sin \delta. \tag{2.25}$$

The output power $P_{out} = 3V_\phi I_\phi \cos \theta$, after some derivation based on Fig. 2.7, we can get the output power equation related to the torque angle as shown below,

$$P_{out} \approx \frac{3V_\phi I_\phi \sin \theta}{X_s}, \tag{2.26}$$

where X_s is inductance phase winding. It is obviously shown that If we choose a smaller torque angle for the machinery at the related power in the design, the machinery will haver more power handling capability and pull out torque. Our design method will based on the much smaller torque angle compared with the traditional value, which will increase the magnets thickness and air-gap size. The larger air-gap size contributes to reducing the windage loss and noise level. The increase magnet thickness helps to avoid demagnetization.

If air-gap is small, the peak winding magnetic field can be calculated from:

$$B_{a,peak} = \frac{4}{\pi} \frac{\mu_0}{\hat{g}_{total}} \frac{\hat{N}_a}{N_p} 1.5\sqrt{2} I_{p,rated}. \tag{2.27}$$

We can get the initial total effective air-gap size based on Eqn. 2.27

$$\hat{g}_{total} = \frac{4}{\pi} \frac{\mu_0}{g_{a,peak}} \frac{\hat{N}_a}{N_p} 1.5\sqrt{2} I_{p,rated}, \tag{2.28}$$

where $\hat{g}_{total}$ also can be calculated as:

$$\hat{g}_{total} = k_c g'_{total} \tag{2.29}$$

where k_c is called cater's coefficient and can be determined by:

$$k_c = \frac{\tau_s}{\tau_s - \frac{2b_{s0}}{\pi}\left[\arctan\frac{b_{s0}}{2g'_{total}} - \frac{g'_{total}}{b_{s0}}\ln\left(1+(\frac{b_{s0}}{2g'_{total}}^2)\right)\right]} \approx \frac{\tau_s}{\tau_s - \frac{b_{s0}^2}{5g'_{total}+b_{s0}}} \tag{2.30}$$

where $g'_{total} = g + d_m/\mu_{rm}$. We know $\frac{d_m}{g} \approx P_c$ and $P_c = \frac{\alpha_m}{1-\alpha_m}\mu_{rm}$, after some derivation, we get:

$$\begin{cases} g = (1-\alpha_m)g'_{toatl} \\ d_m = \alpha_m g'_{toatl}\mu_{rm}. \end{cases} \tag{2.31}$$

If the designed air gap is large, which will needed to calculated the MMF from the permanent magnet and MMF generated from the air gap. The total MMF from the two parts can be added up and expressed by :

$$F_{total} = \frac{r_g B_{r,pk}}{\mu_0}\left[\frac{1}{\mu_{rm}}\ln(\frac{r_a+d_m}{r_a}) + \ln(\frac{r'_{is}}{r_a+d_m})\right], \tag{2.32}$$

where $r'_{is} = r_a + d_m + g_{eff}$, r_g is the radius of the actual air gap, r_a represents the inner radius of the rotor. According Eqn. 2.32, g_{eff} can be calculated, then the actual air gap and magnet thickness can be obtained.

Rotor Size

Total rotor diameter including magnet is:

$$D_r = D - 2g. \tag{2.33}$$

Rotor inner diameter can be determined by:

$$D_i = D_r - 2d_m. \tag{2.34}$$

Double layer lap Winding Scheme

There are numerous winding schemes in a PM motor such as single-layer concerting lap winding, single-layer distributing winding, two-layer concerting lap winding, two-layer distributing winding, etc. The two-layer winding scheme is widely used in different kinds of PM machinery.The number of the conductors per coil N_c is determined by using:

$$N_c = \frac{1.1 V_{\phi,rated}}{2\sqrt{2}\pi f_e q k_w B_{g,pk} DL} \tag{2.35}$$

Where $V_{\phi,rated}$ represents the rated phase voltage, f_e is the electrical frequency, q is the number of the winding groups per pole, k_w describes the winding factor including pitch factor, distribution factor and winding skew factor. Similarly, the effective turns per phase is determined by:

$$N_{eff} = \frac{N_p q N_c K_w}{1.1} \tag{2.36}$$

Where N_p is the number of poles. Next, we will introduce a method step by step to show how to determine two-layer winding coil pitch and connection.

Step 1. Find the nominal coil span(S_c) in slots

- If Slot numbers (N_s) / Pole numbers(N_p) is an integer $\qquad S_c = \frac{S}{N_p} - 1$
- If N_s/N_p is not an integer $\qquad S_c = max\Big(fix(\frac{N_s}{N_p}), 1\Big)$.

Step 2. Calculate the relative electric angle of in slots of all coils

The relative electrical angle(expressed in the range of $-180\,^\circ$ to $180\,^\circ$ of the kth slot is :

$\theta_{slot}(k) = mod\big[(k-1)\gamma + 180\,^\circ, 360\,^\circ\big] - 180\,^\circ.$

The relative electrical angle of in slot of the kth coil is also:

$\theta_{coil}(k) = mod\big[(k-1)\gamma + 180\,^\circ, 360\,^\circ\big] - 180\,^\circ.$

Step 3. Readjust in slot angles if their magnitude are greater than $90\,^\circ$. It means that if the magnitude of coil angles are great than $90\,^\circ$, we need to reverse the coil direction; thereby changing the angle by $180\,^\circ$.

Step 4. Picking up $\big(N_s$/phase number$(m)\big)$ coils for Phase A. For the angles calculated in the last step, we pick up those (S/m) close to $0\,^\circ$ as phase A coils.

Step 5. Calculate the slot offsets to other wind phases. From $mod[S_{off}\gamma, 360\,^\circ]$ and $\gamma = \frac{N_p}{2}\frac{360\,^\circ}{S}$, we can get:

$S_{off} = 2\frac{N_s}{mP}(1+mn) = 2q(1+mn)$

where n is a integer value that makes S_{off} also an integer. Phase B will star from slot$\big(mod(S_{off}, S)+1\big)$.

Step 6. Check to find out whether the winding is valid. The winding is valid if all slots contain two coil sides each. If it is not valid, go back to Step 4 and pick up coil for Phase A.

Power losses

Power losses [109][44][2][29] [108] are the key point to know the motor performance because they determine the machine's efficiency and temperature-rise. There are three types of losses: Copper loss, Core loss, and Mechanical loss. Mechanical loss contains windage and friction loss typically

is very small and can be ignored compared to the other two types of losses. The copper losses are generally the largest component of power loss in brush-less PM motors. They can be calculated by:

$$P_{copper} = mI^2_{p,rated}R_s \tag{2.37}$$

where m is the number of phases; $I^2_{p,rated}$ is the RMS phase current and R_s is the phase resistance and can be determined by $R_s = \rho_{copper}\frac{l}{s}$, ρ_{copper} represents the resistivity of the copper and can be calculated as $\rho = \rho_{20}[1 + \alpha(T - 20)]$ ohm-m, where $\rho_{20} = 1.724 \times 10^{-8}$ ohm-m is the resistivity at $20\,^{\circ}\mathrm{C}$ $\alpha = 0.0393/^{\circ}\mathrm{C}$; and α is the the temperature coefficient of resistivity.The winding temperature affects the resistivity of the windings. Normally, the winding temperature increase $50\,^{\circ}\mathrm{C}$, the resistivity of the windings rise by 20%, the winding temperature increases $135\,^{\circ}\mathrm{C}$, the resistivity of the windings rise by 53%, the $I^2_{p,rated}R_s$ losses increase the same if the current remains the same. A useful formula can be derived from the resistivity of the copper equation to scale the resistance from one temperature to another:

$$R_{s2} = \frac{234.5 + T_2}{234.5 + T_1} \times R_{s1} \tag{2.38}$$

The effect of eddy-current in the stator conductors must be taken in to account when the machines run in high speed or machines operating with an inverter having a high switch frequency. The density of the current flowing in a conductor tends to a thin skin on its surface, which make the individual strands of wire small compared to the skin-depth.In general, the proximity effects occur in neighbution conductors cause a time-varying magnetic field and induces a circulating current inside the windings, usually with the same slot. Litz wire is helpful in spurring effect proximately.

Core losses are generally the second largest component of power loss in the brush-less PM motor, which can be subcategories as the hysteresis and eddy current losses. The hysteresis loss in the energy used to align and rotate magnetic domains. The loss per BH cycle is proportional to the

enclosed loop area, suggesting that the mean power loss due to hysteresis is proportional to the frequency f. We can use C.P.Steinmetz formula to determine the hysteresis loss:

$$P_h = K_h f B_{pk}^n [W/kg] \tag{2.39}$$

where K_h is the coefficient of the hysteresis loss.

Induced current causes the eddy-current loss by an alternating magnetic field induces a voltage. This voltage generates circulating currents in a conducting core, called eddy currents. Whenever there is a change in a magnetic field, an eddy current is induced. The higher the resistivity of the soft materials of the stator and rotor, the lower the eddy-current loss. The eddy-current loss can be determined using the classical formula:

$$P_e = K_e B_{pk}^2 f^2 [W/kg] \tag{2.40}$$

whereK_e is the coefficient of eddy-current loss and can be calculated from an idealized theory as:

$$K_e = \frac{\pi^2 t_{lam}^2 \sigma}{6\rho_m} \tag{2.41}$$

where t_{lam} is the lamination thickness, σ is the conductivity, and ρ_m is the mass density. From Eqn. 2.40 and Eqn. 2.41, we can know that the eddy-current loss can be reduced in two ways: using a high-resistivity material and using laminations. Using a high-resistivity material will increase the skin depth, which will make the distribution of magnetic flux density more uniform. Dividing the core into a large number of thin slices that ate electrically insulated from each other by an oxide film. These thin insulted sheets, called lamination. The thinner lamination steels, the lower value of K_e; for example, if t_{lam} is reduced from 0.5mm to 0.35mm, K_e decrease by half. The total core

loss we can calculated by:

$$P_c = K_h f B_{pk}^n + C_e f^2 B_{pk}^2 \tag{2.42}$$

Summary

This section talks about the design method of high-efficiency electrical machinery. The advantage of the design method is that it can increase the high load capacity at no cost of increasing the total machine size. A much smaller torque angle than that in the traditional design at relating load is selected, which is between about 2 degrees and about 10 degrees. The most import part of the design is to determine the air-gap and permanent magnet size. According to the design method relating to the much smaller torque angle, which will result in the larger air-gap size and larger magnet thickness. The larger air-gap size contributes to reducing the windage loss and noise level. The increase magnet thickness helps to avoid demagnetization. Both them contribute to high efficiency and high overload capability. Based on the design method, all the parameters will be related to the torque angle, working point of a permanent magnet, and the permanent magnet embrace, which is easier for the designer to make a new design.

CHAPTER 3: PERMANENT MAGNET MACHINERY CONTROL

Introduction

Typically, there are two types of the diver for the PMSM: square-wave drive and sin-wave drive. In the square-wave system, the back EMF is a flat-topped waveform, and the ampere-conductor distribution of the stator ideally remains constant and fixed in space for a predetermined commutation interval while the magnet rotates past it. Hall sensor board is used to detect the correct current switching position. The transistors turn on or off based on the commutation stable In the sine-wave system, the back EMF is sinusoidal, and the ampere-conductor distribution of the stator rotates ate the synchronous speed fixed by the frequency and the number of poles. The torque is produced by the interaction between the stator and rotor magnetic field. The angle between the rotor magnetic field and stator magnetic field should be controlled well to get the maximum torque performance. For PMSM, we need to control the magnetic field generated from the stator winding. It is complicated to control motor on a three-phase reference frame directly, so we need to transfer the three-phase abc quantities into dq quantities. The critical point of this transfer is the rotor position that is a significant factor of the all PMSM control system. People usually use the encoder or resolver to get the rotor position information. We also can use sensor-less control based on Sliding model control (SMO) to estimate rotor position.

dq Theory of Permanent Magnet Synchronous Machines

To simply the PMSM equation and control the motor, people always to use $dq0$ frame to model and analyze PMSM. It divides the PMSM armature quantities into two rotating components, one aligned with the field-winding axis (the direct-axis component), and one in quadrature with the

field-winding axis(the quadrature-axis component), which is called park's transformation.

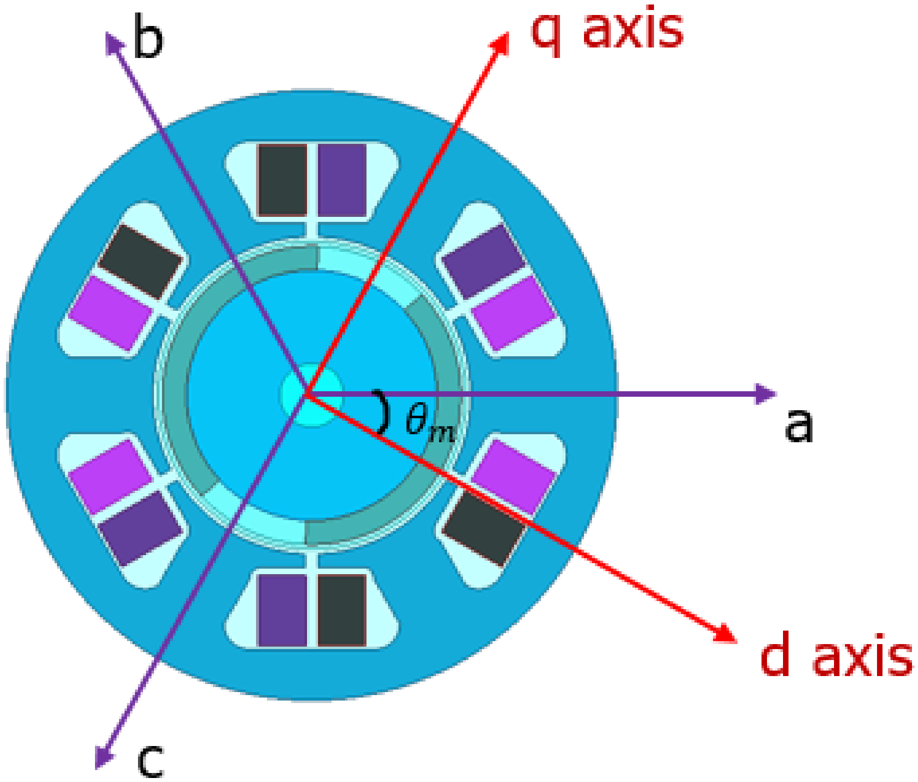

Figure 3.1: $d - q$ axis on synchronous machine

Letting S represent a stator quantity to be transfered and $\theta_{me} = \frac{N_p}{2}\theta_m$. This conversion comes through the $\boldsymbol{K}$ matrix.

$$\boldsymbol{S_{dqo}} = \boldsymbol{K}\boldsymbol{S_{abc}}, \tag{3.1}$$

and its inverse format is

$$\boldsymbol{S_{abc}} = \boldsymbol{K^{-1}} \boldsymbol{S_{dqo}}. \tag{3.2}$$

The $\boldsymbol{K}$ and $\boldsymbol{K^{-1}}$ matrix in the MIT's notation can be expressed as:

$$\boldsymbol{K} = \frac{2}{3} \begin{bmatrix} \cos(\theta_{me}) & \cos(\theta_{me} - 2\pi/3) & \cos(\theta_{me} - 2\pi/3) \\ -\sin(\theta_{me}) & -\sin(\theta_{me} - 2\pi/3) & -\sin(\theta_{me} - 2\pi/3) \\ 1/2 & 1/2 & 1/2 \end{bmatrix} \tag{3.3}$$

$$\boldsymbol{K^{-1}} = \frac{2}{3} \begin{bmatrix} \cos(\theta_{me}) & -\sin(\theta_{me}) & 1 \\ \cos(\theta_{me} - 2\pi/3) & -\sin(\theta_{me} - 2\pi/3) & 1 \\ \cos(\theta_{me} + 2\pi/3) & -\sin(\theta_{me} + 2\pi/3) & 1 \end{bmatrix} \tag{3.4}$$

In the Purdue's notation system, $\theta_r = \theta_{me} + \frac{\pi}{2}$ is used to replace θ_{me}. The $\boldsymbol{K}$ and $\boldsymbol{K^{-1}}$ matrix in the Purdue's's notation can be expressed as:

$$\boldsymbol{K} = \frac{2}{3} \begin{bmatrix} \sin(\theta_r) & \cos(\theta_{me} - 2\pi/3) & \sin(\theta_{me} + 2\pi/3) \\ \cos(\theta_r) & \cos(\theta_{me} - 2\pi/3) & \cos(\theta_r + 2\pi/3) \\ 1/2 & 1/2 & 1/2 \end{bmatrix} \tag{3.5}$$

$$\boldsymbol{K^{-1}} = \frac{2}{3} \begin{bmatrix} \sin(\theta_r) & \cos(\theta_r) & 1 \\ \sin(\theta_r - 2\pi/3) & \cos(\theta_r - 2\pi/3) & 1 \\ \sin(\theta_r + 2\pi/3) & \cos(\theta_r + 2\pi/3) & 1 \end{bmatrix} \tag{3.6}$$

In our system, all the derivations will be based on MIT's notation system. Here dq means direct and

quadrature. Direct axis is aligned with the rotor's pole. Quadrature axis refers to the axis whose electrical angle is orthogonal to the electric angle of direct axis. A third component S_0 is called the zero-sequence component, which is also included. Under balanced-three-phase conditions, there is no zero-sequence component.

Transformation of the stator winding voltage equations can be presented by:

$$\boldsymbol{V_{abc}} = \boldsymbol{R_s i_{abc}} + \frac{d}{dt}\boldsymbol{\lambda_{abc}}, \tag{3.7}$$

after some derivation, we can get:

$$\boldsymbol{V_{dq0}} = \boldsymbol{R_s i_{dq0}} + \frac{d}{dt}\boldsymbol{\lambda_{dq0}} + \boldsymbol{K}\left(\frac{d}{dt}\boldsymbol{K^{-1}}\right)\boldsymbol{\lambda_{dq0}}, \tag{3.8}$$

where $\boldsymbol{R_s} = \begin{bmatrix} R_s & 0 & 0 \\ 0 & R_s & 0 \\ 0 & 0 & R_s \end{bmatrix}$. In order to get the $\boldsymbol{V_{dq0}}$, we derive the derivation of $\boldsymbol{K^{-1}}$,

$$\frac{d}{dt}\boldsymbol{K^{-1}} = -\omega_{me} \begin{bmatrix} \sin(\theta_{me}) & \cos(\theta_{me}) & 0 \\ \sin(\theta_{me} - 2\pi/3) & \cos(\theta_{me} - 2\pi/3) & 0 \\ \sin(\theta_{me} + 2\pi/3) & \cos(\theta_{me} + 2\pi/3) & 0 \end{bmatrix}, \tag{3.9}$$

then, we can get:

$$\boldsymbol{K}\left(\frac{\boldsymbol{dK^{-1}}}{dt}\right) = \begin{bmatrix} 0 & -\omega_{me} & 0 \\ \omega_{me} & 0 & 0 \\ 0 & 0 & 0 \end{bmatrix}. \tag{3.10}$$

Finally, the $\boldsymbol{V_{dq0}}$ can be obtained :

$$\begin{bmatrix} V_d \\ V_q \\ V_0 \end{bmatrix} = \begin{bmatrix} R_s i_d + \frac{d}{dt}\lambda_d - \lambda_q \omega_{me} \\ R_s i_q + \frac{d}{dt}\lambda_q - \lambda_d \omega_{me} \\ R_s i_0 + \frac{d}{dt}\lambda_0 \end{bmatrix}. \tag{3.11}$$

For salient pole rotor, the inductance can be approximately expressed as:

$$\boldsymbol{L_{abc}} = \begin{bmatrix} L_{aa} & L_{ab} & L_{ac} \\ L_{ba} & L_{bb} & L_{bc} \\ L_{ca} & L_{cb} & L_{cc} \end{bmatrix}. \tag{3.12}$$

The self-inductance can be expressed as:

$$\begin{cases} L_{aa} = L_{ls} + L_1 + L_2 \cos(2\theta_{me}) \\ L_{bb} = L_{ls} + L_1 + L_2 \cos 2(\theta_{me} - \frac{2\pi}{3}) \\ L_{cc} = L_{ls} + L_1 + L_2 \cos 2(\theta_{me} + \frac{2\pi}{3}) \end{cases}, \tag{3.13}$$

where L_{ls} is the winding leakage inductance, L_1 is the inductance corresponding to the constant component of the air-gap permeance and L_2 is the magnitude of the inductance which corresponds to the component of air-gap permeance which varies with rotor angle. The mutual-inductance can be expressed as:

$$\begin{cases} L_{ab} = L_{ab} = -\frac{1}{2}L_1 + L_2 \cos(2\theta_{me} - \frac{2\pi}{3}) \\ L_{bc} = L_{CB} = -\frac{1}{2}L_1 + L_2 \cos(2\theta_{me}) \\ L_{aC} = L_{ca} = -\frac{1}{2}L_1 + L_2 \cos(2\theta_{me} + \frac{2\pi}{3}) \end{cases}. \tag{3.14}$$

Therefor, we can get the following inductance matrix in $dq0$ frame:

$$\boldsymbol{L_{dq0}} = \boldsymbol{K L_{abc} K^{-1}} \begin{bmatrix} L_d & 0 & 0 & 0 \\ 0 & L_q & 0 & 0 \\ 0 & 0 & L_0 & 0 \end{bmatrix}, \tag{3.15}$$

where $L_d = L_{ls} + L_{md}$, $L_q = L_{ls} + L_{mq}$, $L_0 = L_{ls}$, and $L_{md} = \frac{3}{2}(L_A + L_B)$, $L_{mq} = \frac{3}{2}(L_A - L_B)$.

The flux-linkage of PMSM in the abc frame is:

$$\boldsymbol{\lambda_{abc}} = \boldsymbol{L_{abc} i_{abc}} + \boldsymbol{\lambda_{PMabc}}, \tag{3.16}$$

where $\boldsymbol{\lambda_{PMabc}}$ is the permanent magnet flux-linkage in the abc frame, the matrix is equal to:

$$\boldsymbol{\lambda_{PMabc}} = \lambda_{PM} \begin{bmatrix} \cos(\theta_{me}) \\ \cos(\theta_{me} - \frac{2\pi}{3}) \\ \cos(\theta_{me} - \frac{2\pi}{3}) \end{bmatrix}. \tag{3.17}$$

The flux-linkage of PMSM in the abc frame can be transformed into $dq0$ frame as:

$$\boldsymbol{\lambda_{dq0}} = \boldsymbol{L_{dq0} i_{dq0}} + \boldsymbol{\lambda_{PMdq0}}, \tag{3.18}$$

where $\boldsymbol{\lambda_{PMdq0}} = \boldsymbol{K \lambda_{PMabc}} = \begin{bmatrix} \lambda_{PM} \\ 0 \\ 0 \end{bmatrix}$, $\lambda d = L_d i_d + \lambda_{PM}$, $\lambda q = L_q i_q$, and $\lambda_0 = L_{ls} i_0$.

For the linear model $\frac{d\lambda_{PMdq0}}{dt} = V$ and $\boldsymbol{\lambda_{PMabc}} = \lambda_{PM}$, we can get:

$$\frac{d\boldsymbol{i_{dq0}}}{dt} = \boldsymbol{L_{dq0}^{-1}} \boldsymbol{V}. \tag{3.19}$$

Finally, the dynamical equation in terms of current can be obtained as:

$$\frac{d}{dt}\begin{bmatrix} i_d \\ i_q \\ i_0 \end{bmatrix} = \begin{bmatrix} \frac{1}{L_d}(v_d - R_s i_d + \omega_{me} L_q i_q) \\ \frac{1}{L_q}(v_q - R_s i_q + \omega_{me} L_d i_d - \omega_{me}\lambda_{PM}) \\ \frac{1}{L_0}(v_0 - R_s i_0) \end{bmatrix} \tag{3.20}$$

If the winding is Y connected, i_0 is equal to zero, only need to consider i_d and i_q.

Electrical instantaneous input power on stator can also be expressed through dq0 theory,

$$P_{in} = \frac{3}{2}R_s(i_d^2 + i_q^2 + 2i_0^2) + \frac{3}{2}(i_d\frac{d\lambda_d}{dt} + i_q\frac{d\lambda_q}{dt} + 2i_0\frac{d\lambda_0}{dt}) + \frac{3}{2}\frac{P}{2}\omega_m(\lambda_d i_q - \lambda_q i_q), \tag{3.21}$$

where $\frac{3}{2}R_s(i_d^2 + i_q^2 + 2i_0^2)$ is copper loss, $\frac{3}{2}(i_d\frac{d\lambda_d}{dt} + i_q\frac{d\lambda_q}{dt} + 2i_0\frac{d\lambda_0}{dt})$ is magnetic power in windings, and $\frac{3}{2}\frac{P}{2}\omega_m(\lambda_d i_q - \lambda_q i_q)$ is mechanical power. We use P_{mecg} to express the mechanical power, so the electromagnetic torque on rotor can be expressed by:

$$T_e = \frac{P_{mecg}}{\omega_m} = \frac{3}{2}\frac{P}{2}(\lambda_d i_q - \lambda_q i_d), \tag{3.22}$$

putting λ_d and λ_q into electromagnetic torque equation, then we can get

$$T_e = \frac{P_{mecg}}{\omega_m} = \frac{3}{2}\frac{N_p}{2}(\lambda_{PM} i_q + (L_d - L_q)i_q i_d) = K_T i_q, \tag{3.23}$$

where $K_T = \frac{3N_p}{2}(\lambda_{PM} i_q + (L_d - L_q) i_d)$ is called torque constant. For round rotor machine $(L_d = L_q)$, the torque constant $K_T = \frac{3N_p}{\lambda_{PM} i_q}$.

After the dq frame analysis, we can describe the motor's non-linear behavior based on the dynamic equation. Four dynamic equations are used to built the PMSM or PMSM modeling.

$$\frac{di_d}{dt} = \frac{1}{L_d}(v_d - R_s i_d + \omega_{me} L_q i_q) \tag{3.24}$$

$$\frac{di_q}{dt} = \frac{1}{L_q}(v_q - R_s i_q + \omega_{me} L_d i_d - \omega_{me} \lambda_{PM}) \tag{3.25}$$

$$\frac{d\omega_m}{dt} = \frac{1}{J}(T_e - T_L - c\omega_m) \tag{3.26}$$

$$\frac{d\theta_m}{dt} = \omega_m \tag{3.27}$$

where v_d is input voltage on d axis, v_q is input voltage on $q$axis, T_L is load torque, J is initial moment of rotor, and c is coefficient of firection.

The fellowing Fig shows the motor modeling built by MATLAB based on the dynamical equation.

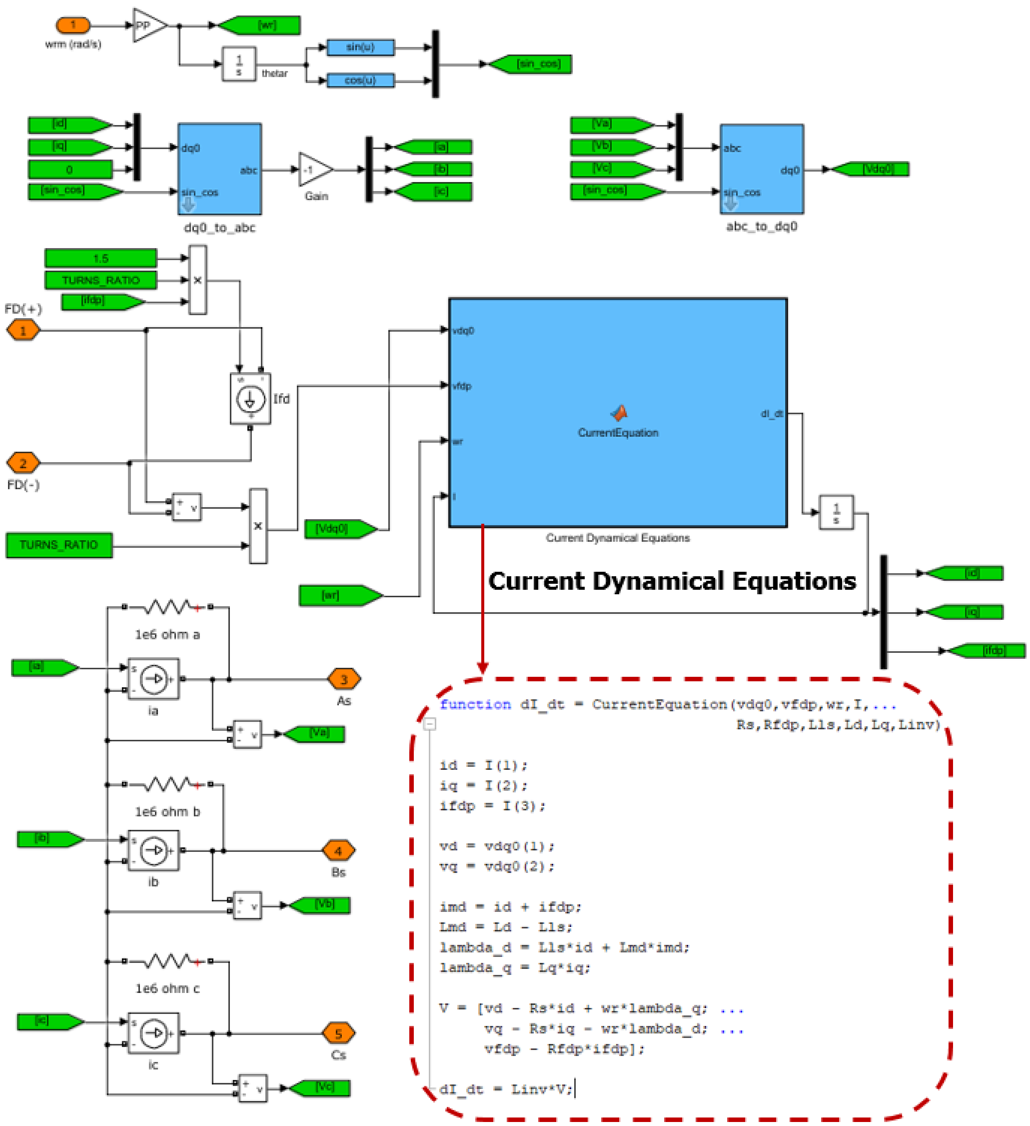

Figure 3.2: Motor modeling

Space Vector Pulse Width Modulation (SVPWM) is popular for controlling motor drivers or three-phase rectifier because it offers good utilization of the DC-link voltage, low current ripple, and reduced switching losses compared to conventional PWM modulation.

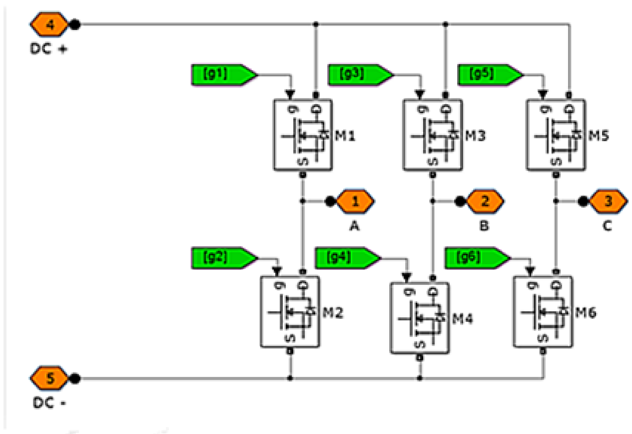

Switching State	On-state Switch
[1 1 1]	S_1, S_2, S_3
[0 0 0]	S_2, S_4, S_6
[1 0 0]	S_1, S_4, S_6
[1 1 0]	S_1, S_3, S_6
[0 1 0]	S_2, S_3, S_6
[0 1 1]	S_2, S_3, S_5
[0 0 1]	S_2, S_4, S_5
[1 0 1]	S_1, S_4, S_5

Figure 3.3: Three phase switching states

As we can see from Fig. 3.3, there are 8 possible switching states, for witch two of them are zero switching states and six of them are active switching states.They can be represented by active vector $(V_1 - V_6)$ and zero vector (V_0). Active vectors are stationary and not rotating, zero vectors are placed in the axis origin.

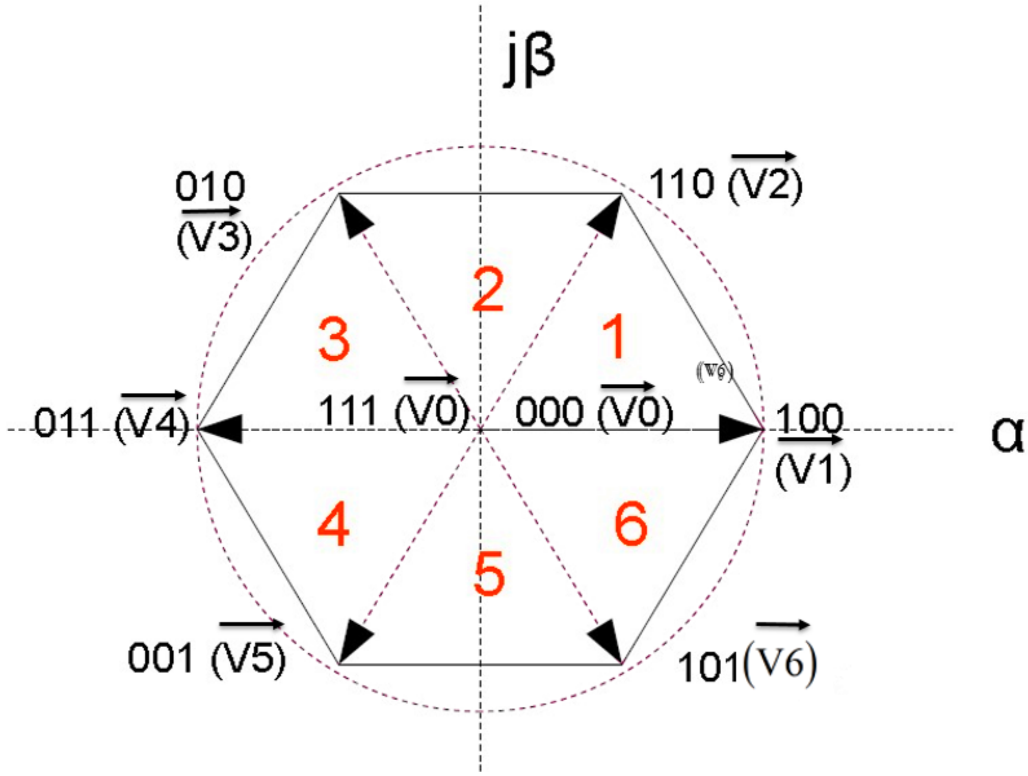

Figure 3.4: Space voltage vectors in different sectors

Assuming the reference voltage space vector $\overrightarrow{V_{ref}}$ falls between two adjacent base vectors in sector I as shown in the below picture.

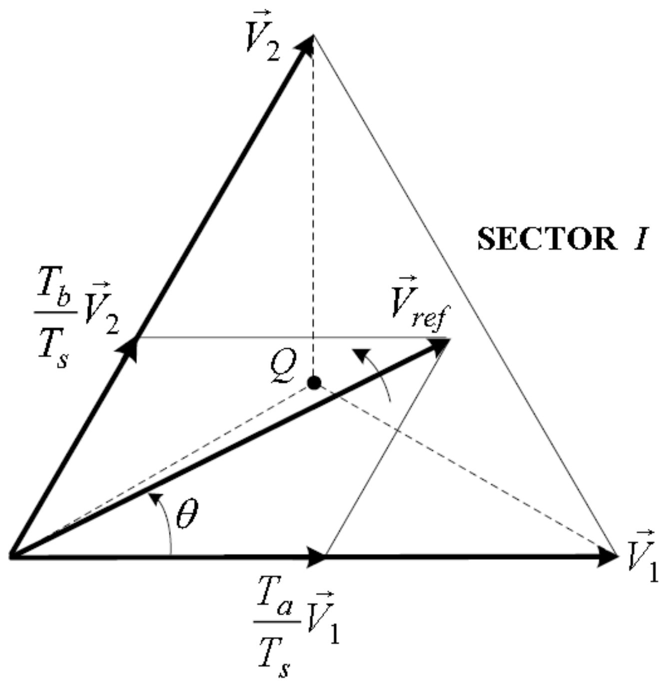

Figure 3.5: Approximation of an arbitrary voltage space vector using base voltage

According volt-second balancing, we can get the fellowing equation.

$$\begin{cases} \overrightarrow{V_{ref}}T_s = \overrightarrow{V_1}T_a + \overrightarrow{V_2}T_b + \overrightarrow{V_0}T_0 \\ T_s = T_a + T_b + T_c \end{cases}, \tag{3.28}$$

where T_a,T_b and T_0 are dwell times for $\overrightarrow{V_1}$,$\overrightarrow{V_2}$ and $\overrightarrow{V_0}$, T_s is sampling period, space vector $\overrightarrow{V_{ref}} = V_{ref}e^{j\theta}$, $\overrightarrow{V_1} = \frac{2}{3}V_d$, $\overrightarrow{V_2} = V_d e^{j\frac{\pi}{3}}$ and $\overrightarrow{V_0} = 0$, then we can get the real part and imag part of the reference vector,

$$\begin{cases} \overrightarrow{V_{ref}}T_s = \overrightarrow{V_1}T_a + \overrightarrow{V_2}T_b + \overrightarrow{V_0}T_0 \\ T_s = T_a + T_b + T_c \end{cases}. \tag{3.29}$$

After some derivation we can get three time durations

$$\begin{cases} T_a = \frac{\sqrt{3}T_s V_{ref}}{V_d}\sin(\frac{\pi}{3}-\theta) \\ T_b = \frac{\sqrt{3}T_s V_{ref}}{V_d}\sin(\theta) \\ T_0 = T_s - T_a - T_b \end{cases}, \tag{3.30}$$

where $0 \leq \theta \leq \pi/3$. These equations mean that an arbitrary space vector within the triangle defined by the two adjacent base vectors, between which the expected vector is located, can be represented by the sum of these two vectors. This is realized by timely activating the two vectors combined with zero vectors sequentially. If the switching process is fast enough, meaning the period T_s is short, the approximation can precisely represent the reference vector.

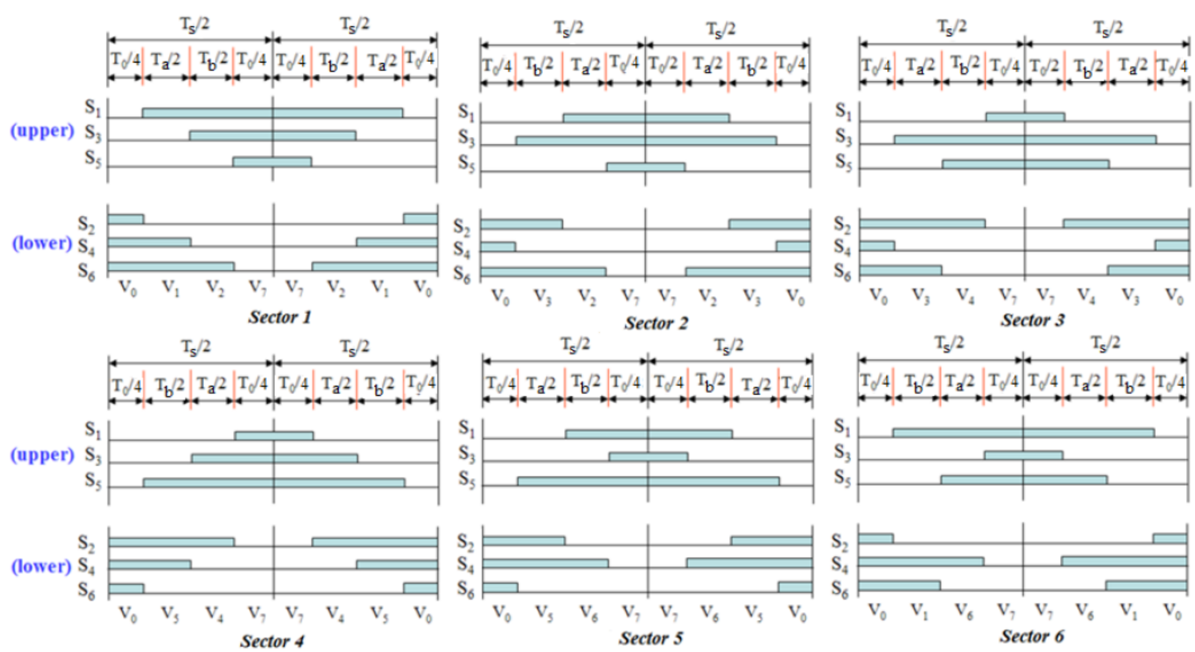

Figure 3.6: Duty time for each sector

As we can see from Fig. 3.6, there are seven switching states for each sector within one cycle. It always starts and ends with a zero vector. This also means that there is no additional switching state needed when changing the sector. The uneven numbers travel counterclockwise in each sector, and the even segments go clockwise.

Shaft Position

The shaft position is very important for field orientation control. Optical encoder and resolver are normally used to get the rotor position. They are stalled on the shaft and expensive, which will require the designer to make the driver board bigger and limit the PMSM application. Based on these disadvantage, the sensor-less control technique based on the SMO is necessary to replace the resolver and encoder. The SMO control is a strategy of variable structure control. The stability of the system entirely depends on the sliding surface. In order to make suer the system error can be controlled and stable, the gain factor should be choose big enough. Normally, a discontinuous sign function is used as a switching function, which caused the chattering issue. In order to reduce the chattering problem, sigmoid function is selected as a switching function to build the SMO model. The PMSM model in the Alpha-beta reference frame can be expressed as:

$$\begin{cases} L_s(\frac{di_\alpha}{dt}) = -R_s i_\alpha - e_\alpha + u_\alpha \\ L_s(\frac{di_\beta}{dt}) = -R_s i_\beta - e_\beta + u_\beta \end{cases} , \tag{3.31}$$

where i_α, i_β, u_α, u_β are the phase currents, phase voltages, and back EMF in the Alpha-beta frame, respectively, R_s is the stator phase resistance and L_s is the stator phase inductance.

The electromotive force in Alpha-beta frame is related to the flux linkage, electrical velocity and

electrical rotor position, which can be calculated as:

$$\begin{cases} e_\alpha = -\psi_f \omega_r \sin\theta_m \\ e_\beta = -\psi_f \omega_r \cos\theta_m \end{cases}, \tag{3.32}$$

where ψ_f is the flux linkage of the PMSM, ω_r is the electrical angular velocity of the shaft, and θ_m is the electrical rotor rotating angle. The back EMF equations contain the rotor position information, that means if we can know the PMSM back EMF, the rotor position can be obtained.

Design of SMO

The sigmoid function SMO model in Alpha-beta frame is built as:

$$\begin{cases} \frac{d\hat{i}_\alpha}{dt} = H\hat{i}_\alpha + u_\alpha - kF(\hat{i}_\alpha - i_\alpha) \\ \frac{d\hat{i}_\beta}{dt} = H\hat{i}_\beta + u_\beta - kF(\hat{i}_\beta - i_\beta) \end{cases}, \tag{3.33}$$

where $H = -\frac{\hat{R}_s}{L_s}$, $[\hat{i}_\alpha \hat{i}_\beta]^T$ is the desired Alpha-beta frame current value and $[i_\alpha i_\beta]$ is the measured current value in the Alpha-beta frame. The sigmoid switching function is represented as:

$$F(x) = \left[\frac{s}{a + |s|}\right]. \tag{3.34}$$

The sliding surface of the sigmoid SMO model is chosen as:

$$S(X) = \begin{bmatrix} s_\alpha & s_\beta \end{bmatrix}^T = \begin{bmatrix} \hat{i}_\alpha - i_\alpha & \hat{i}_\beta - i_\beta \end{bmatrix}^T. \tag{3.35}$$

The estimation errors should become zero when estimation errors of the SMO mode reach the sliding surface. The Lyapunov function is selected to verify the stability of the sigmoid function SMO model.

$$\Gamma = \frac{1}{2} S(X)^T S(X) + \frac{1}{2}(\hat{R}_s - R_s)^2, \tag{3.36}$$

where $\frac{1}{2}(\hat{R}_s - R_s)^2$ is used to estimate the stator resistance which is a variable parameter. The stability condition of the SMO is as fellow:

$$\dot{\Gamma} = S(X)^T \dot{X} + (\hat{R}_s - R_s)\dot{\hat{R}}_s \leq 0. \tag{3.37}$$

The sliding condition is obtained by subtracting Eqn. 3.31 from Eqn. 3.33 as

$$\begin{aligned} \dot{\Gamma} \quad = \quad & \begin{bmatrix} \dot{\bar{i}}_\alpha & \dot{\bar{i}}_\beta \end{bmatrix} \begin{bmatrix} (\hat{H} - H)\hat{\alpha} + H(\hat{\alpha} - i_\alpha) + \frac{1}{L_s}\left[e_\alpha - kH(\dot{\bar{i}}_\alpha)\right] \\ (\hat{H} - H)\hat{\beta} + H(\hat{\beta} - i_\beta) + \frac{1}{L_s}\left[e_\beta - kH(\dot{\bar{i}}_\beta)\right] \end{bmatrix} \\ & + \bar{R}_s \dot{\hat{R}}_s \leq 0, \end{aligned} \tag{3.38}$$

where $H = -\frac{\hat{R}_s}{L_s}$, $\hat{H} = -\frac{\hat{R}_s}{L_s}$, and $\bar{R}_s = \hat{R}_s - R_s$. To satisfy the condition $\dot{\Gamma} \leq 0$, Eqn. 3.38 is decomposed into two equations as follows:

$$\begin{bmatrix} \dot{\bar{i}}_\alpha & \dot{\bar{i}}_\beta \end{bmatrix} \begin{bmatrix} (\hat{H} - H)\hat{\alpha} \\ (\hat{H} - H)\hat{\beta} \end{bmatrix} + \bar{R}_s \dot{\hat{R}}_s = 0, \tag{3.39}$$

$$\begin{bmatrix} \dot{\bar{i}_\alpha} & \dot{\bar{i}_\beta} \end{bmatrix} \begin{bmatrix} H(\hat{\dot{\alpha}} - i_\alpha) + \frac{1}{L_s}\left[e_\alpha - kH(\dot{\bar{i}_\alpha})\right] \\ H\hat{\dot{\beta}} + A(\hat{\dot{\beta}} - i_\beta) + \frac{1}{L_s}\left[e_\beta - kH(\dot{\bar{i}_\beta})\right] \end{bmatrix} = 0. \tag{3.40}$$

The estimation of the stator resistance can be obtained from Eqn. 3.39

$$\dot{\hat{R}_s} = \frac{1}{L_s}(\bar{i_\alpha} \cdot \hat{i_\alpha} + \bar{i_\beta} \cdot \hat{i_\beta}). \tag{3.41}$$

Using this estimated value of stator resistance in the current control can improve the stability of the system. In order to keep the SMO stable, the observer gains should satisfy the inequality condition found in Eqn. 3.38. As a result

$$k > max(\mid e_\alpha \mid\mid e_\beta \mid). \tag{3.42}$$

Therefore, if k is selected is large enough, which can make suer the stability of this kind of sliding motion. The back EMF can be obtained once the system reaches the sliding surface.

$$\begin{bmatrix} e_\alpha \\ e_\beta \end{bmatrix} = \begin{bmatrix} kF(\hat{i_\alpha} - i_\alpha) \\ kF(\hat{i_\beta} - i_\beta) \end{bmatrix}. \tag{3.43}$$

Position and Velocity Estimation of the Rotor

The equivalent back EMF still contains the high-frequency components. A first-order low-pass filter can be used for filtering, but it will cause phase delay. In order to get the real-time angular velocity information without using the low-pass filter and phase compensation part, we built an observer to extract the back EMF signal. The changer rate of the shaft angular velocity is far lower than that of stator current, then we can assume the shaft angular velocity $\dot{\omega_r} = 0$. The back EMF

model of PMSM can be express as:

$$\begin{cases} \frac{de_\alpha}{dt} = -\omega_r e_\beta \\ \frac{de_\beta}{dt} = \omega_r e_\alpha \end{cases} . \tag{3.44}$$

A back EMF is constructed

$$\begin{cases} \frac{d\hat{e_\alpha}}{dt} = -\hat{\omega}_r \hat{e_\beta} - p(\hat{e_\alpha} - e_\alpha) \\ \frac{d\hat{e_\beta}}{dt} = -\hat{\omega}_r \hat{e_\alpha} - p(\hat{e_\beta} - e_\beta) \\ \frac{d\hat{e_\omega}}{dt} = (\hat{e_\alpha} - e_\alpha)\hat{e_\beta} - (\hat{e_\beta} - e_\beta)\hat{e_\alpha} \end{cases} \tag{3.45}$$

where p is the gain of observe, whose value is greater than zero. By subtracting Eqn. 3.44 from Eqn. 3.45 and doing further consolidation, the error equation of the observer is determined as

$$\begin{cases} \frac{d\tilde{e_\alpha}}{dt} = -\tilde{\omega_r}\hat{e_\beta} - \omega_r \tilde{e_\beta} - p\tilde{e}_\alpha \\ \frac{d\tilde{e_\beta}}{dt} = -\tilde{\omega_r}\hat{e_\alpha} + \omega_r \tilde{e_\alpha} - p\tilde{e}_\beta \\ \frac{d\tilde{e_\omega}}{dt} = \tilde{e_\alpha}\hat{e_\beta} - \tilde{e_\beta}\hat{e_\alpha} \end{cases} . \tag{3.46}$$

The Lyapunov function is defined to verify the stability of the observer.

$$\Gamma = \frac{\tilde{e_\alpha}^2 + \tilde{e_\beta}^2 + \tilde{\omega_r}^2}{2}. \tag{3.47}$$

Differentiating the Eqn. 3.47

$$\dot{\Gamma} = \tilde{e_\alpha}\dot{\tilde{e_\alpha}} + \tilde{e_\beta}\dot{\tilde{e_\beta}} + \tilde{\omega_\alpha}\dot{\tilde{\omega_\alpha}}. \tag{3.48}$$

Substituting Eqn. 3.46 into the above equation yields

$$\dot{\Gamma} = -p(\tilde{e_\alpha}^2 + \tilde{e_\beta}^2) \leq 0. \tag{3.49}$$

We can see from Eqn. 3.49 that the back EMF observer is asymptotically stable. The position signal can be obtained through the observer without phase delay.

$$\tilde{\theta_m} = -\arctan(\frac{\tilde{e_\alpha}}{\tilde{e_\beta}}) \tag{3.50}$$

Sensor-less Field Oriented Control of PMSM

As we know, the rotor of PMSM has a constant flux magnitude because of permanent magnets and the stator winding of PMSM create a rotating electromagnetic field when it is being energized. The rotating magnetic field can be controlled by controlling the stator currents. In order to get better dynamic performance, it is necessary to decouple the torque generation and the magnetization functions in PMSM, which is called Field Oriented Control (FOC). Doing park transformation based the shaft angle that is obtained using the advanced SMO, i_d and i_q can be obtained. The i_d is related to the flux component and i_q is related to the torque component, so we only need to control the dq current. In order to get the maximum torque, the referenced d axis current i_{dref} should be set to 0 for surface permanent magnet motor. We should give a negative referenced d axis current i_{dref} when flux weakening operation is required. The output of the speed regulator will be used as the torque command i_{qref}. We will use this control for our alternator control system. For the Wrench BLDC motor, hall sensor board is used to help the motor start at the begin, then the sensor-less FOC will be used to control the motor. The sensor-less field oriented control of PMSM is shown below

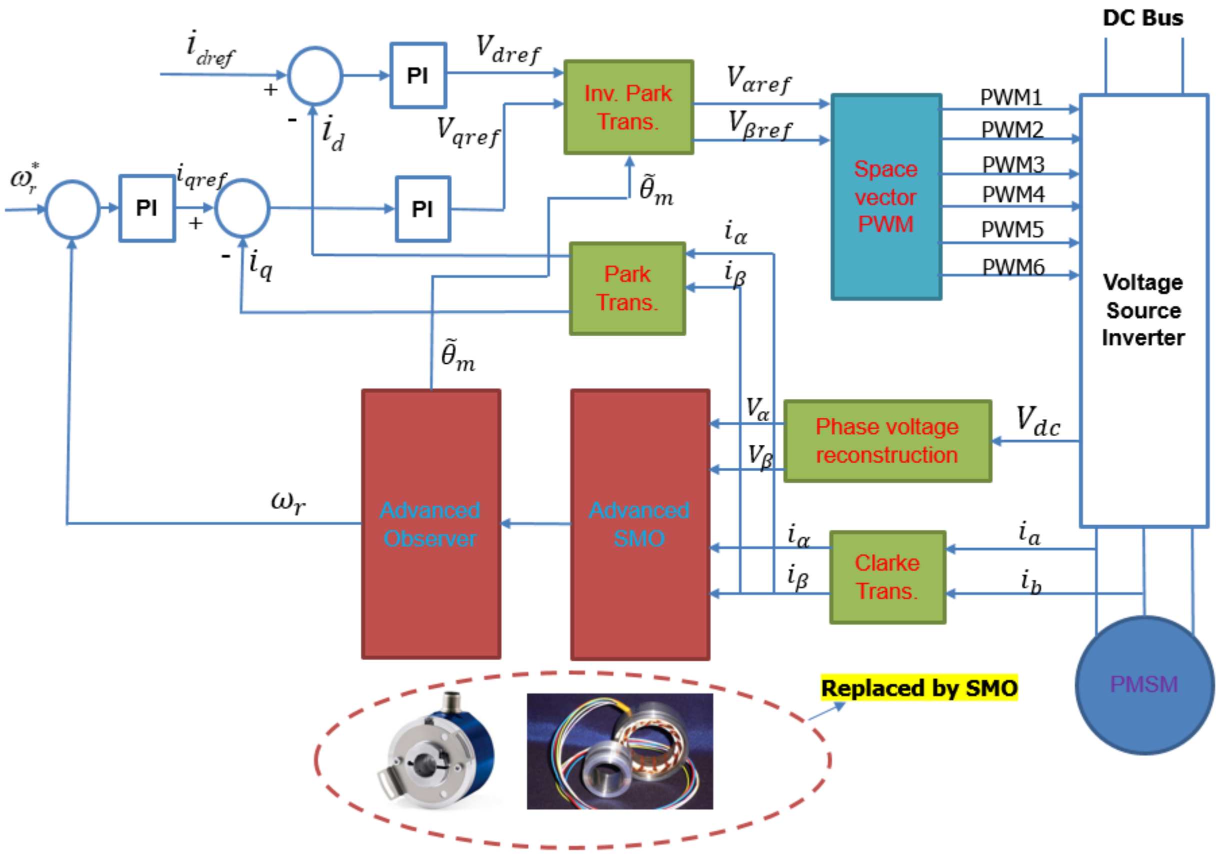

Figure 3.7: Overall block diagram of sensor-less field oriented control of PMSM

Summary

In this chapter, the dynamic modeling and control methods of the permanent magnet machinery are introduced. The shaft position is key for the PMSM control based on FOC. In order to avoid using resolver or shaft, a sigmoid function SMO is built to reduce chattering issue. This kind of SMO is verified using Lyapunov function and it shows that the large factor k value can ensure the system stable. We also built an observer to replace the low-pass filter to extract the back EMF signal, which can avoid the phase delay. The observer also was verified by Lyapunov function.

CHAPTER 4: PERMANENT MAGNET BRUSH-LESS DC MOTOR AND MECHANICAL STRUCTURE DESIGN FOR THE ELECTRIC IMPACT WRENCH SYSTEM [1]

Introduction

Brushless dc motors are popular in a wide range of industrial applications, such as computer peripherals, servo control systems and electrical tools due to their robustness, simplicity, large torque to volume ratio and high-efficiency[46] [41] [88] [25] [64] [6] [57] [55]. Interior permanent magnet brushless DC (IPMBLDC) electric motor [53] [62] [98] [70] [81] [89] [87] [40] is an important category of these motors, constructed with the permanent magnets inserted into the steel rotor core and does not need to be glued such as in surface mounted permanent magnet motors. The leakage path of interior magnet motors usually includes a saturable magnetic bridge and the web, which will make the coefficient of flux leakage variable. In the previous chapter, we have described the key points of how to design a PM motor. In this chapter, we apply the methodology to the design of a IPMBLDC [24] [21] [78] [104] [52] [42] [76] for the electric impact wrench. The differences between designing a IPM motor and SPM motor is that we need to assume a flux leakage coefficient in the initial design and built an advanced equivalent magnetic circuit of IPMBLDC to calculate the modify the coefficient of flux.

Using an electric impact wrench instead of the traditional wrench has been a worldwide trend. Car and other automatic machines purchases number are rapidly increasing every year indicating that there will be a big market for an electric impact wrench. Brush-less DC motor design for the electric impact wrench requires high reliability, good control performance, small size, losing

[1]This chapter has been published at journal Energies [40].

bolting time, low cost and easy industrial mass production. The motor connects to planetary gear reducer with a transmission ration to get high output torque. The speed of impact wrench will be reduced and the bolting time is related to motor speed, main pressure spring as well as shock block. High pull out torque is required to get high load capability and improve motor lifetime.

A permanent interior magnet synchronous motor (IPMSM) with concentrated windings is chosen in the design. Because IPMSM usually has the large torque to volume ratio and high efficiency. The motor of electric impact should be able to tolerate some torque ripple and does not require extra field weakening at higher speed. Based on these requirements, we choose the dc control drive for the brush-less DC motor (BLDC) design. Hall sensor board was designed and fabricated to detect the correct current switching position at the low speed to help the motor start, then advanced SMO is used to control the BLDC.

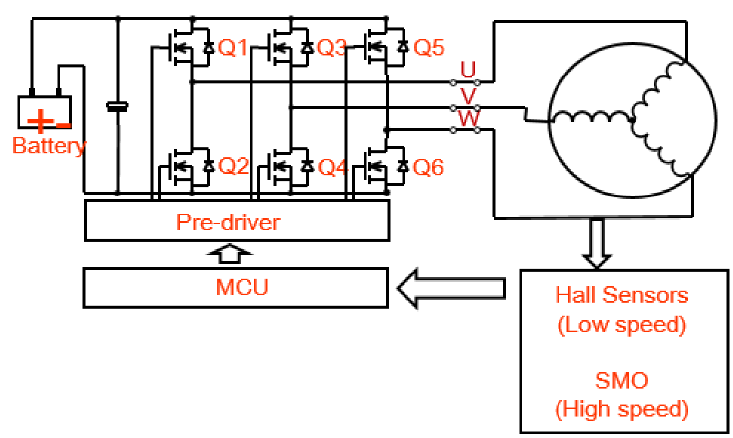

Figure 4.1: Simple block of BLDC control topology

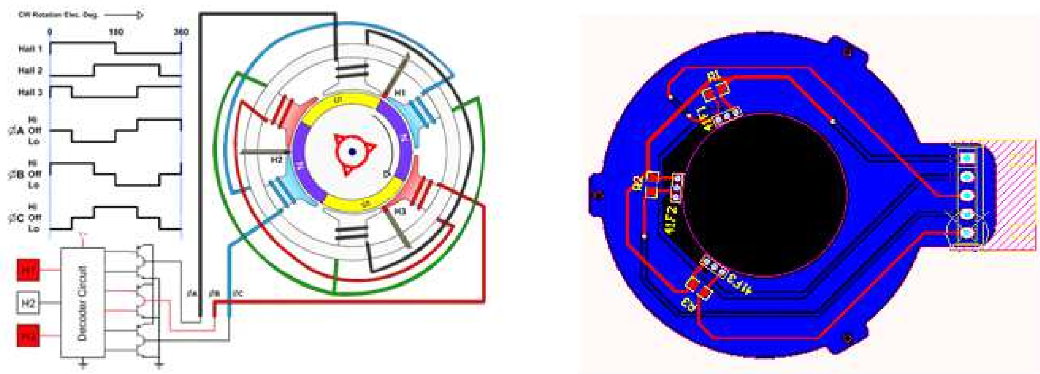

(a) BLDC motor dc control configuration (b) Hall sensor board designed by Altium Designer

Figure 4.2: BLDC motor dc control configuration and hall sensor board at low speed

Assumed flux leakage coefficient and selected working point of a permanent magnet were used in the initial design. An advanced equivalent magnetic circuit was developed to verify the total flux leakage and the quiescent operating position based on initial design parameters. Key design method points are considered and analyzed. Thermal analysis is given to simulate the temperature rise of all parts of the motor. The new impact wrench mechanical structure is designed, and its working principle analyzed. An electromagnetic field analysis based on MATLAB and MAXWELL 2D FEM was used in the design to verify the equivalent magnetic circuit and optimize the IPMBLDC parameters. Experimental results are obtained to confirm the configuration. The electrical and mechanical models are combined and provides an analytical IPMBLDC design method. We also show an innovative and reasonable mechanical dynamical calculation method for the impact wrench system.

Magnetic Bridge and Rib

The magnetic bridge (Fig. 4.3) affects the leakage coefficient of the interior permanent magnet motor [76] as shown in Eqn. 4.1. Flux density around the magnetic bridge is very high, which results in low permeability and high reluctance, thus magnetic flux leakage is small. If we would like to obtain stronger magnetism isolating effect, the size of the magnetic bridge should be smaller, but the mechanical strength will be reduced when the motor runs at high speed. Comprehensive consideration should be taken when choosing the size of the magnetic bridge.

$$\Phi_0 = \frac{\alpha_m B_r A_m}{k_{ls}} \tag{4.1}$$

where Φ_0 is no-load main flux, k_{ls} is leakage coefficient, α_m is working point of a permanent magnet, B_r is residual magnetization density and A_m is cross-sectional area providing the magnetic flux per pole.

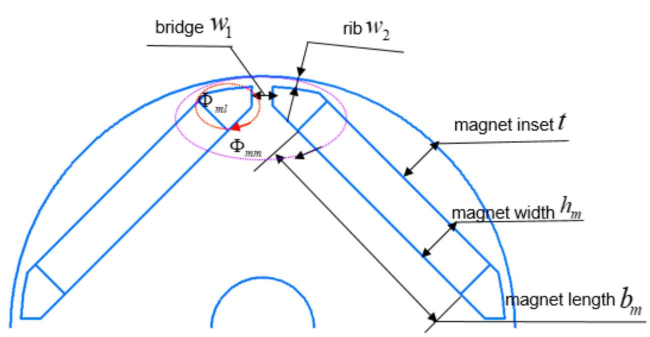

Figure 4.3: Magnet and flux guide dimensions

Pull Out Torque

Pull-out torque is the largest torque that a motor can operate under synchronism in case of momentary overload with. It can can be calculated by traditional power angle equation ignoring the effects of the stator resistance of the torque.

$$T = \frac{1/2mN_p}{\omega_s^2}\left[\frac{e_{PM}U}{L_d}\sin(\delta) + \frac{U^2}{2}(\frac{1}{L_q} - \frac{1}{L_d})\sin(2\delta)\right] \tag{4.2}$$

where m is the number of phase, ω_s is the angular frequency of the stator current, L_d and L_q are the direct axis inductance and quadrature axis inductance, e_{PM} is the permanent magnet flux linkage induced back EMF and δ is the torque angle.

$$e_{PM} = \frac{\xi_1 N_a \omega_s \phi_\sigma}{\sqrt{2}} \tag{4.3}$$

where ξ_1 is the fundamental winding factor, N_a is the number of series turns of each phase and ϕ_σ is air gap magnetic flux.

$$\phi_\sigma = \frac{H_c d_m}{\frac{d_m}{\mu_r \mu_0} + R_\sigma + R_{Fe}} \tag{4.4}$$

where H_c is the magnet coercive field strength, d_m is the magnetic thickness, μ_r is the magnet relative permeability, μ_0 is the vacuum permeability and R_{Fe} is the iron reluctance.

$$L_{md} = \frac{m}{2}\frac{4}{\pi}\alpha\mu_0\frac{1}{2p}\frac{\tau_p}{g_{eff} + d_m}\ell(\xi_1 N)^2 \tag{4.5}$$

where m is phase number, α is the arithmetic average of the flux density distribution in one pole area, τ_p is the pole pith, g_{eff} is the effective air gap length (excluding the magnets), ℓ is the stack electromagnetic length. We can know from Eqn. 4.2 that the first part of Eqn. 4.2 is the magnetic torque, and the second part represents the reluctance torque due to saliency. The inductance in

q-direction is higher than in d-direction because of inverse saliency. For surface-mounted PMSM, direct axis inductance is equal to the quadrature axis inductance, so there is no saliency, which means the torque will proportional to the load angle.

When the thickness of the magnets increases, also the back-EMF increase as we can see from Eqn. 4.3 and Eqn. 4.4, while the direct-axis inductance decrease as shown in Eqn. 4.5, which result in increased torque production capability of the PMSM. The pull-out torque increases and the rated torque is obtained at lower load anger.

Typically, we choose the power factor angle equal to 0 at the full-load for PMSM. If we want to get a high pull-out angle in the design, we can select the torque angle as our reference to design the motor, the smaller torque angle we choose, the more significant pull-out torque we will get when the full-load torque is known.

Size of the Permanent Magnet

After we get the air-gap size, we can use Eqn. 4.6, Eqn. 4.7 based on to determine the size of the permanent magnet. Assumed flux leakage coefficient and selected permanent magnet working point are used in the equations.

$$h_m = \frac{K_s K_\alpha \alpha_m}{(1-\alpha_m)k_{ls}} g \tag{4.6}$$

$$b_m = \frac{2k_{ls} B_{g,pk} \tau_1}{\pi \alpha_m B_r K_\phi} \tag{4.7}$$

where h_m is magnet length, b_m is magnet width, g is air gap length, K_s is motor saturation factor with values ranging from 1.05 to 1.3, K_α is rotor structure factor whose value range is between 0.7 and 1.2, $B_{g,pk}$ is peak value of air gap fundamental wave, K_ϕ is air gap flux waveform factor, which

is related to the pole arc coefficient. The air gap flux waveform of an ideal BLDC is a square wave, so the value of pole arc coefficient should be big enough with reference to [94]. For IPMBLDC, we can calculate the pole arc coefficient approximately using

$$\alpha_p \approx \frac{b}{\tau_p} \tag{4.8}$$

where b is pole shoe arc length, and τ_p is pole pitch

Improved Magnet Circuit Model of BLDC

A commonly used half of BLDC configurations is shown in flowing picture.

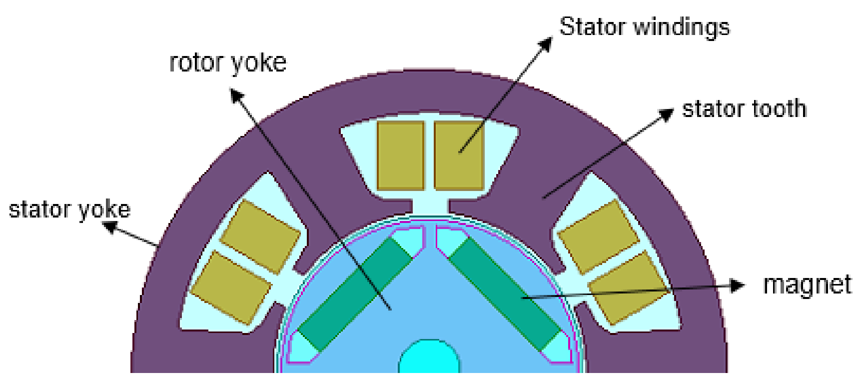

Figure 4.4: Half of BLDC configuration

The route of main flux loop goes through the magnet, rotor yoke, air gap, stator tooth, and stator yoke. Taking the flux linkage of the magnet to magnet and magnet end flux linkage into consideration, the improved equivalent magnetic circuits of BLDC, which is composed of a half-pole pair for which the symmetry is considered, as shown in Fig. 4.5 (a).

Where R_{sy}, R_{st}, R_g, R_{rya}, R_{ryb}, R_σ, R_{mo}, R_{ml}, R_{mm} are the reluctances of stator yoke, stator tooth, air-gap, rotor yoke above the magnet, rotor yoke below the magnet, assembly gap between magnets and laminations, the magnet, the magnet end flux leakage, magnet to magnet flux leakage, respectively.

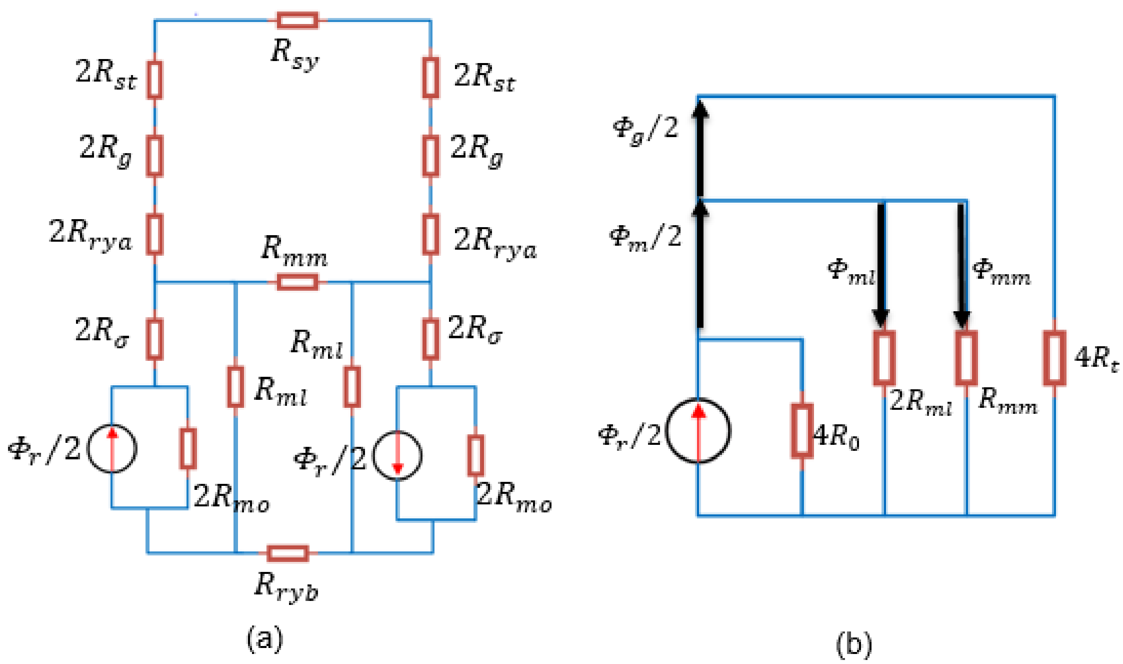

Figure 4.5: The improved equivalent magnetic circuits of BLDC

Fig. 4.5 (a) can be simplified as shown in Fig. 4.5 (b). R_z is the total reluctances of air-gap, stator tooth, rotor tooth, stator yoke, rotor yoke above and below the magnet, which can be calculated as

$$R_z = R_{sy}/4 + R_{st} + R_g + R_{rya} + R_{ryb}. \tag{4.9}$$

The magnet end flux leakage reluctances can be expressed as

$$R_{\sigma} = \frac{d_{\sigma}}{\mu_0 A_{\sigma}}, \tag{4.10}$$

where d_{σ} is the distance between the magnet and the duct, A_{σ} is the cross-sectional area of the air-gap between the magnet and the duct. The magnet reluctances is equal to

$$R_{mo} = \frac{h_m}{\mu_0 \mu_r A_m} \tag{4.11}$$

where h_m is the length of the permanent magnet, A_m is the cross-sectional area of magnet. R_0 is sum of magnet end flux leakage reluctances and magnet reluctance. Thus,

$$R_0 = R_{\sigma} + R_{mo}. \tag{4.12}$$

To calculate the rationality of the point of the operation and the coefficient of the flux leakage, we need to analyze the equivalent of the magnet circuit, estimate the main magnetic circuit as shown in the Fig. 11, analyze the magnet end flux leakage ϕ_{ml} and the magnet to magnet flux leakage ϕ_{ml}. We assume the bridges and webs are saturated, which can be replaced by a flux-source. We also assume the magnet web flux density is 1.8 Tesla. Therefore, we can calculate the magnet end flux leakage Φ_{mi}. The flux density of the magnet depth can be limited to 2 Tesla. Therefore, we can calculate the magnet to magnet flux leakage ϕ_{mm}. Comparing the calculated total flux leakage value to the value of the assumption, some structural parameters will be adjusted based on errors using computer-aided tools. We do the same to the operating point α_m. All these repeated calculation will be done with the aid of Matlab.

A flowchart of the procedure of the calculation can be obtained shown in Fig. 4.6. Some magnetic circuit calculation equations are listed in Table. 4.1.

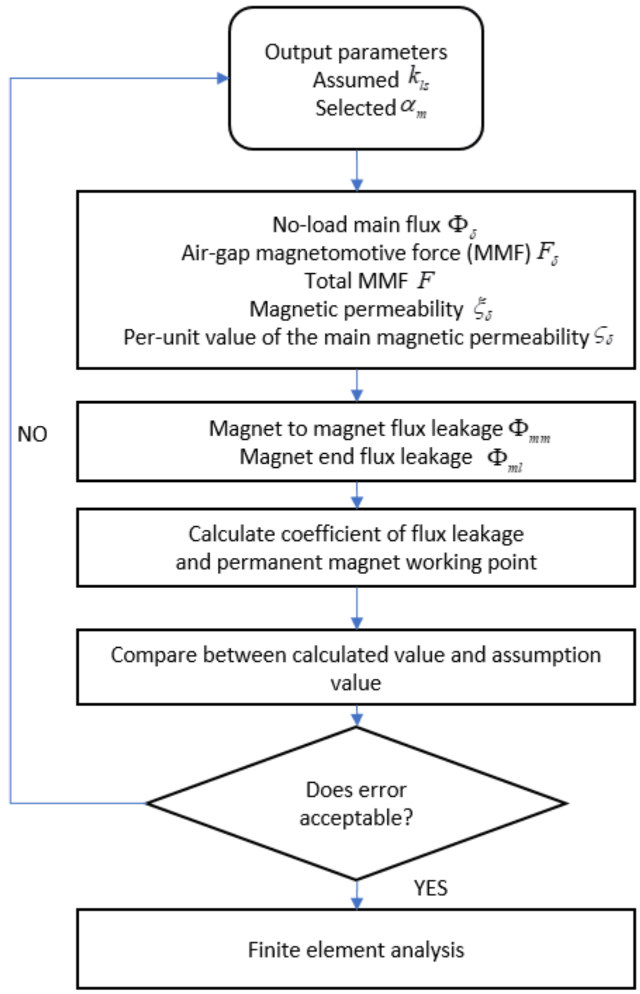

Figure 4.6: The flowchart of the procedure of the design calculation

Table 4.1: Magnetic circuit calculation

No-load main flux	$\Phi_0 = \frac{\alpha_m B_r A_m}{k_{ls}}$
Average air-gap flux density	$B_g = \frac{\Phi_0}{\alpha_p \tau_1 L_e}$
Air-gap MMF	$F_g = \frac{2B_a(d_\sigma + k_c)}{\mu_0}$
Total MMF	$\Sigma F = F_g + F_{st} + F_{sy} + F_{ry}$
Main magnetic permeability	$\lambda_\delta = \frac{\Phi_\delta}{\Sigma F}$
Per-unit value of the main magnetic permeability	$\xi_\delta = \frac{2\xi_\delta h_m}{\mu_0 \mu_r A_m}$
Magnet to magnet flux leakage	$\Phi_{mm} = B_{w1} w_1 L_e / 2$
Magnet end flux leakage	$\Phi_{ml} = B_{w2} w_2 L_e$
Total flux leakage	$\Phi_\sigma = \Phi_{mm} + \Phi_{ml}$
Flux leakage coefficient	$k_{ls} = \frac{\Phi_\delta}{\Phi_\delta + \Phi_\sigma}$
Magnet operating point	$\alpha_m = \frac{k_{ls}\xi_\delta}{k_{ls}\xi_\delta + 1}$

The Design and Calculation of Impact Wrench

Working Principle

An electric impact wrench includes a motor, planetary gear, main pressure spring and shock block. The new mechanical structure makes the planetary gear retarding mechanism as the main transmission mechanism, which can guarantee small volume, lightweight, simple structure, high torque and power, and simple control requirement of IPMBLDC. The motor output force is transmitted by the planetary reducer to the mandrel, and then by the ball, driven by the main pressure spring to make the shock block rotate. Shock block uses its two convex claws to impact shock rod. The impact rod drives the bolt through the sleeve under the action of impact force. When the resistance torque of the bolt exceeds the torque transmitted by the main spring to the impact head, the impact head is retracted along the v-groove of the mandrel under the restriction of the ball, resulting in impact shock block and shock rod convex shoulder tripping. The shock block will continue to rotate under the motor driven at this time. The pawl crosses the shoulder and produces an additional angular

velocity under the main pressure spring, which pushes the pawl against the shoulder and generates an impact torque. The torque is then passed through the sleeve to the bolt or nut, which will make the bolt or nut rotate by an angle. The cycle of shock will continue until the completion of the bolt loading and unloading works. The mechanical structure is shown in Fig. 4.7.

Figure 4.7: Mechanical structure of impact wrench

Planetary Gear Ration Calculations and Design

Our planetary gear for electrical impact wrench is made of one sun gear, one ring, and three planet gears. The sun gear works as the active part, three planet gears are the followers, and the ring is fixed to the housing. The simple planetary gear mechanism is shown in Fig. 4.8.

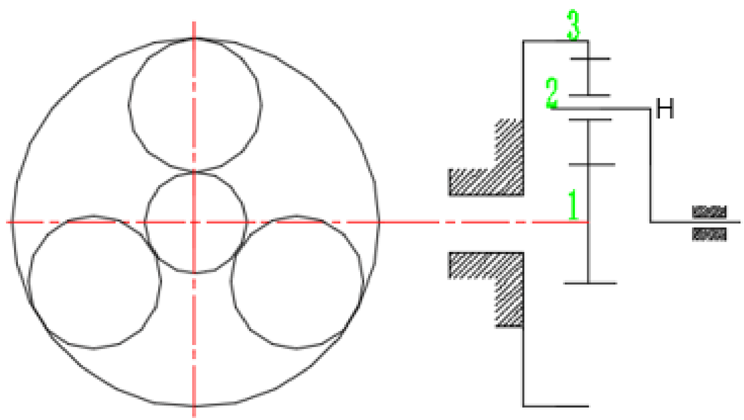

Figure 4.8: Simple planetary gear mechanism

According to the theory of machines and mechanisms, we know:

$$i_{13}^{H} = \frac{n_1^H}{n_3^H} = \frac{n_1 - n_H}{n_3 - n_H} = -\frac{z_3}{z_1} \tag{4.13}$$

where n_1,n_2,n_3 are the speed of sun gear, ring, and plant gear, respectively, z_1 is tooth number of sun gear and z_3 is tooth number of ring.

Since the ring is fixed to the housing, its speed is 0, we can get the planetary gear transmit ratio.

$$\tilde{i_r} = i_{1H} = \frac{n_1}{n_H} = 1 + \frac{z_3}{z_1}. \tag{4.14}$$

After we know the required planetary gear transmit ratio. We can select the tooth number for the sun gear, ring, and plant gear based on Eqn. 4.14 for our design.

The Main Compression Spring Design

The main parameters of pressure spring of impact wrench are shown in Table. 4.2. According to dynamic principles, spring index $C_s = \frac{d_c}{D_c}$; spring constant $k = \frac{GD_c}{8C_s^3 N_2}$, where G is shear modulus of elasticity; the minimum load on spring is $F_1 = kS_1$; the maximum load on spring is $F_2 = kS_2$; the average load on spring is $F_a = (F_1 + F_2)/2$; the resistance torque of the spring to the mandrel $M_F = F_a r_o \tan\beta$. For our electric impact wrench, we need to make sure the torque from the motor to the mandrel is less than the resistance torque of the spring to the mandrel, this is the special requirement for our design. We can follow the mechanical design handbooks to do the compression spring design step by step so we are not going to introduce the procedures in detail. The basic design process is shown in Fig. 4.9.

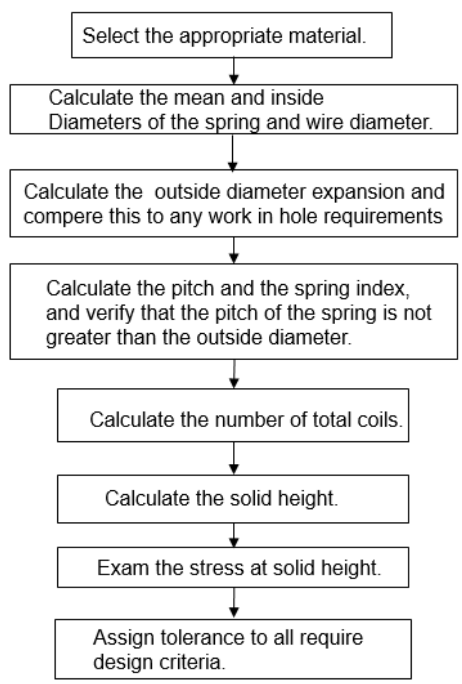

Figure 4.9: The basic spring design procedure

Table 4.2: Parameters of pressure spring

Material	60Si2MnA
Installed length	60mm
Minimum amount of elastic deformation S_1	5mm
Maximum amount of elastic deformation S_2	14mm
Impact stroke length h	9mm
Angle of spiral β	$22\,^{\circ}\mathrm{C}$
Out diameter of a coil D_c	71mm
Inner diameter of a coil d_c	60mm
Total number of winding N_1	6
Number of active winding N_2	3

Shock Block Dynamic Calculation and Design

The shock block shape is shown in Fig. 4.10 (a). Some experience equations are listed below.

$$\begin{cases} l_1 \approx (1-2.5)l_2 \\ l_3 \approx (0.3-0.5)l_s \\ d_1 \approx (1.2-1.5)d_2 \\ D_o \approx (1.2-1.5)d_1 \end{cases} \tag{4.15}$$

For convenient calculations, we simplify it to two steel tubes and two fan-shape claws as shown in Fig. 4.10 (b). The shock block quality is

$$\begin{aligned} m = {} & \frac{p\pi l_1(D_o^2-d_1^2)}{4} + \frac{p\pi l_2(D_o^2-d_2^2)}{4} \\ & + \frac{\alpha p\pi(D_o^2-d_2^2)(l_s-l_1-l_2)}{180\times 4}. \end{aligned} \tag{4.16}$$

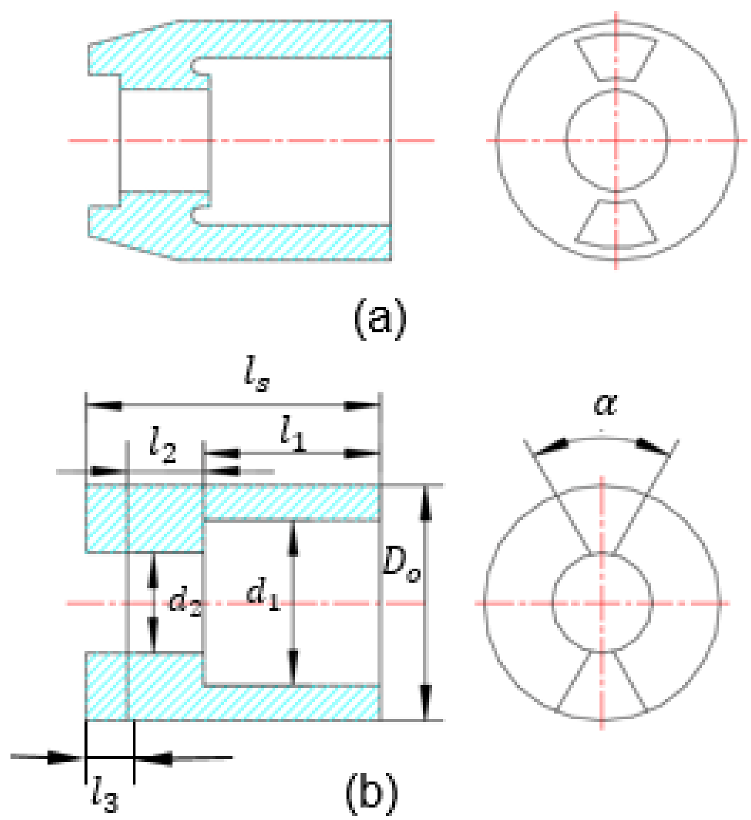

Figure 4.10: Shock block shape

When it is rotating, the steel tube is like the hollow cylinder rotating around the rotation center. The fan-shaped claw is equivalent to a symmetrical fan rotating around the rotation center. We can obtain the moment of inertia of the shock block based on the theory of machines and mechanisms

$$J = \frac{m_1 + m_2 + m_3}{8} D_o^2 + \frac{m_1}{8} d_1^2 + \frac{m_2}{8} d_2^2 + \frac{m_2}{8} d_3^2. \tag{4.17}$$

The absolute angular velocity of the shock block before the impact consists of the average angular velocity of the mandrel and the additional angular velocity of the shock block, that is $\omega_0 = \omega_t + \omega_a$.

The average angular velocity of the mandrel $\omega_t = 2\pi n/(60i)$. The output power of the IPMBLDC is stored in the form of a compressing spring. The stored energy by the compression spring releases into two parts. One part is converted to the kinetic energy of the downward moment of the shock block, and the other part is converted to the kinetic energy of the shock block rotation. According to energy conservation law, we have

$$F_a h = \frac{J\omega_a^2}{2} + \frac{m(Jr\tan\beta)^2}{2} \tag{4.18}$$

after some derivations, we can obtain the additional angular velocity of the shock block

$$\omega_a = \sqrt{\frac{2F_m h}{J + m(r\tan\beta)^2}}. \tag{4.19}$$

We performed the design based on the desired value ω_a. After we pick up coefficients for each parts of length and diameters according to Eqn. 4.15, we put Eqn. 4.16 and Eqn. 4.17 to Eqn. 4.19. Matlab will be numerically calculate the relationship between D_o and l_s. Normally we pick up D_o values according to our IPMBLDC housing diameter; than we can use the relationship between D_o and l_s to get the value of l_s. Finally, we can obtain values of the all parameters.

Impacting shock rod, sleeve, and bolts, in essence, is an elastic collision process of shock block around the rotating center. During the elastic collision, the energy will be transferred. The efficiency of energy transmission is

$$\eta = \frac{\Delta E_1}{E_1}, \tag{4.20}$$

where ΔE_1 is the energy difference before and after impact, E_1 is energy before impact. Assuming the collision is elastic, the recovery coefficient is 1. According to collision theory, we can obtain

$$\eta = \frac{4JJ'}{J+J'}^{\,2} = \frac{4a}{1+a}^{\,2} \tag{4.21}$$

where J' is the converted inertia of the impact system, $a = J/J'$. In the process of disassembly of bolts, J' changes all the time. Therefore a is also variable. Assuming the change range from a_1 to a_2, then we can get the average theory impact efficiency. In our design, the range of a is from 0 to 18.

$$\hat{\eta} = \frac{\int_{a_1}^{a_2} \frac{4a}{(a+1)^2} da}{a_2 - a_1} \tag{4.22}$$

Finally. we get

$$\hat{\eta} = 4[\frac{1}{a_2 - a_1} \ln \frac{a_2 + 1}{a_1 + 1} - \frac{1}{(a_1 + 1)(a_2 + 1)}]. \tag{4.23}$$

If the required tightening torque is T', we can obtain the time of tighten a bolt $t_b = T'/E\hat{\eta}$.

Performance Analysis

Optimization and Simulation

To verify the magnetic circuit model and the design parameters, the 2-D Finite element analysis has been used.

Table 4.3: Calculated results and FEA results

initial design parameters				calculated results			FEA	
k_{ls}	α_m	w_1	w_2	B_δ	k_{ls}	α_m	B_δ	k_{ls}
1.15	0.85	1	0.5	0.598	1.1522	0.861	0.585	1.149
1.15	0.85	1.1	0.5	0.595	1.1539	0.863	0.581	1.1523
1.15	0.85	1.2	0.5	0.591	1.1542	0.865	0.576	1.1531

Table. 4.3 shows the primary design results, calculated results and the FEA results for changing

the magnetic bridge width. We assume the flux density of the bridge is limited to 1.8 Tesla and the flux density of the rib is limited to 2 Tesla. From the table, we can see that the 2-D finite element analysis verifies our calculation and design parameters.

For our IPMBLDC, we evaluate and optimize the motor using ANSYS Maxwell. The dimensions of the IPMBLDC are obtained as shown in Table. 4.4.

Table 4.4: IPMBLDC dimensions

Number of the slots/poles	$6/4$
Stator outer diameter/mm	48
Stator inner diameter/mm	24
Rotor inner diameter/mm	5
Air-gap length/mm	0.5
Magnet width/mm	2.5
Magnet length/mm	9.5
Rotor bridge depth/mm	0.5
Rotor magnet web/mm	1

When we design the motor. The motor must meet the following flux density constraints: (1) Stator tooth flux density lower than 2T; (2) Stator yoke flux density lower that 1.5T; (3) Rotor yoke flux density lower than 1.5T. Through the finite element simulation analysis, the flux distribution of the final designed structure is shown in Fig. 4.11. From the Maxwell 2D simulation results, we can see that the tooth average flux density is $1.62T$, the yoke average flux density is $1.41T$, and the average air-gap flux density is $0.585T$. The web flux density is around $1.76T$, and rib flux density is around $1.95T$. The web flux density is close to the value we assumed. All the results satisfy the requirements.

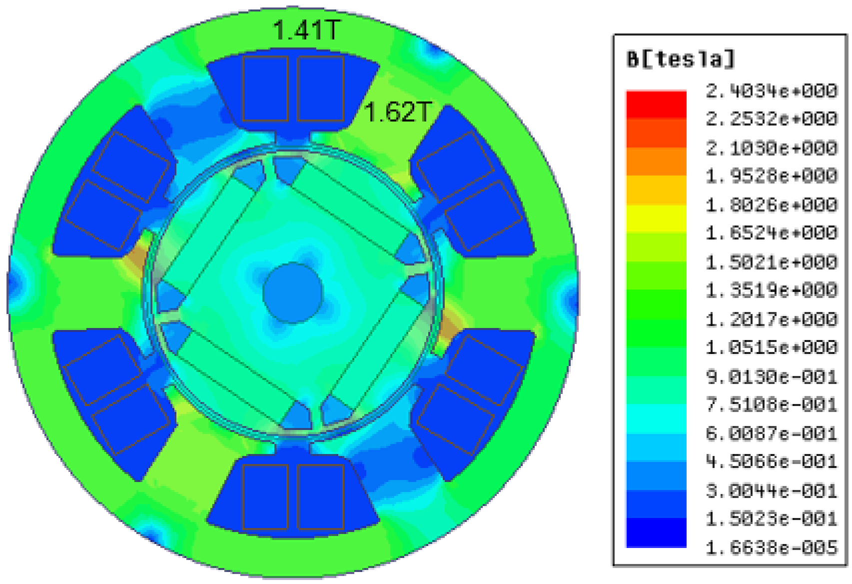

Figure 4.11: Magnetic flux distribution within the proposed magnetic structure:hot magnetic spot

Cogging Torque and No Load Back-EMF

Cogging torque is the consequence of the interaction between the rotor-mounted permanent magnet field and the stator teeth. It will produce a pulsating torque that does not contribute to the net effective torque. The waveform of the cogging torque for the IPMBLDC at rated speed is shown in Fig. 4.12. We know from Fig. 4.12 that the value of cogging torque is around $0.014Nm$, which is about 6.3% ratio of the rated load torque. In order to get high torque, we use concentrated windings, so the value of cogging torque is reasonable for 6-slots, 4-pole motor. For the impact wrench application, there are no critical requirements for cogging torque.

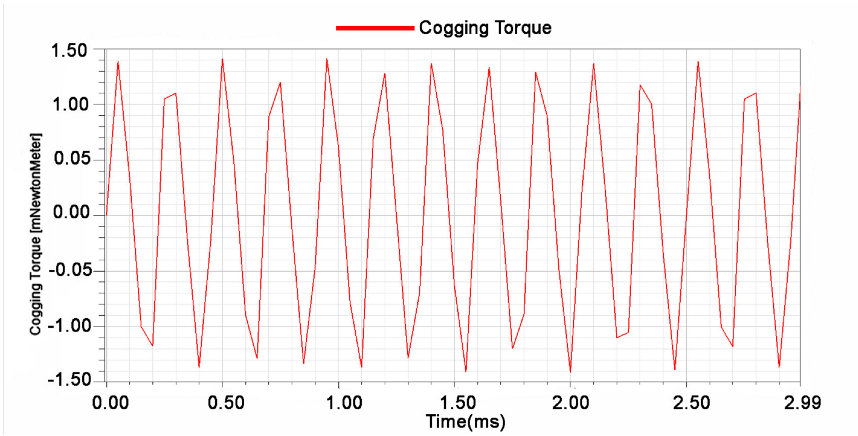

Figure 4.12: Plots of cogging torque

The no-load back-EMF simulation analysis of the IPMBLDC is given in Fig. 4.13. The line to line EMF has a $60°$ flat-top with delta connection.

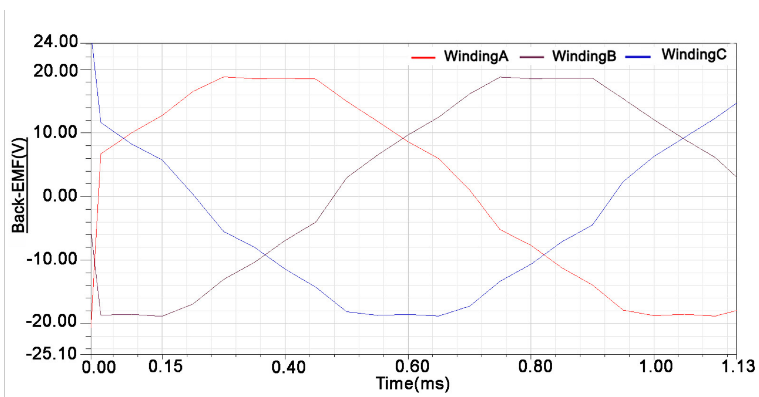

Figure 4.13: The no load back-EMF of the BLDC

In order to avoid demagnetization, the magnet's temperature needs to be kept under control. To preserve the life of the insulation and bearing, excessive heating of the surrounding and injury caused by touch hot surface, the temperature rise of the winding and frame should be kept below a level. In this paper, a fan is used for cooling and power MOSFETs are soldered on aluminum board. We can see from the Fig 4.14 that the maximum temperature appearing in the rotor is around $62\,^{\circ}\mathrm{C}$ after one hour, and the temperature remains stable. Actually, the motor of electric impact wrench is not expected to be in continuous operation, and therefore that maximum temperature will never be reached.

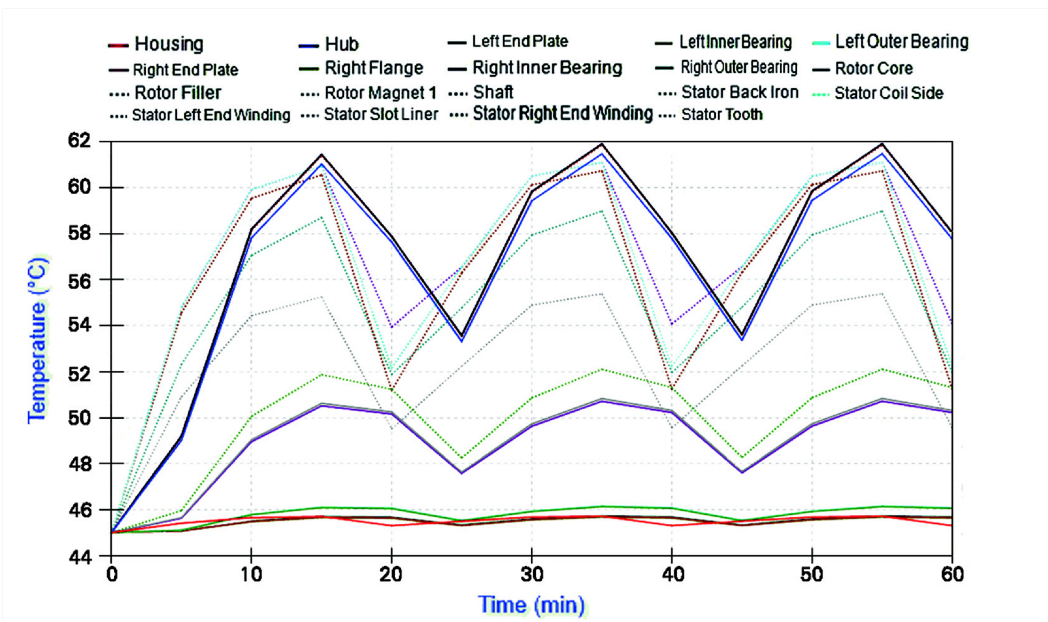

Figure 4.14: Thermal analysis resulting using MotorSolve

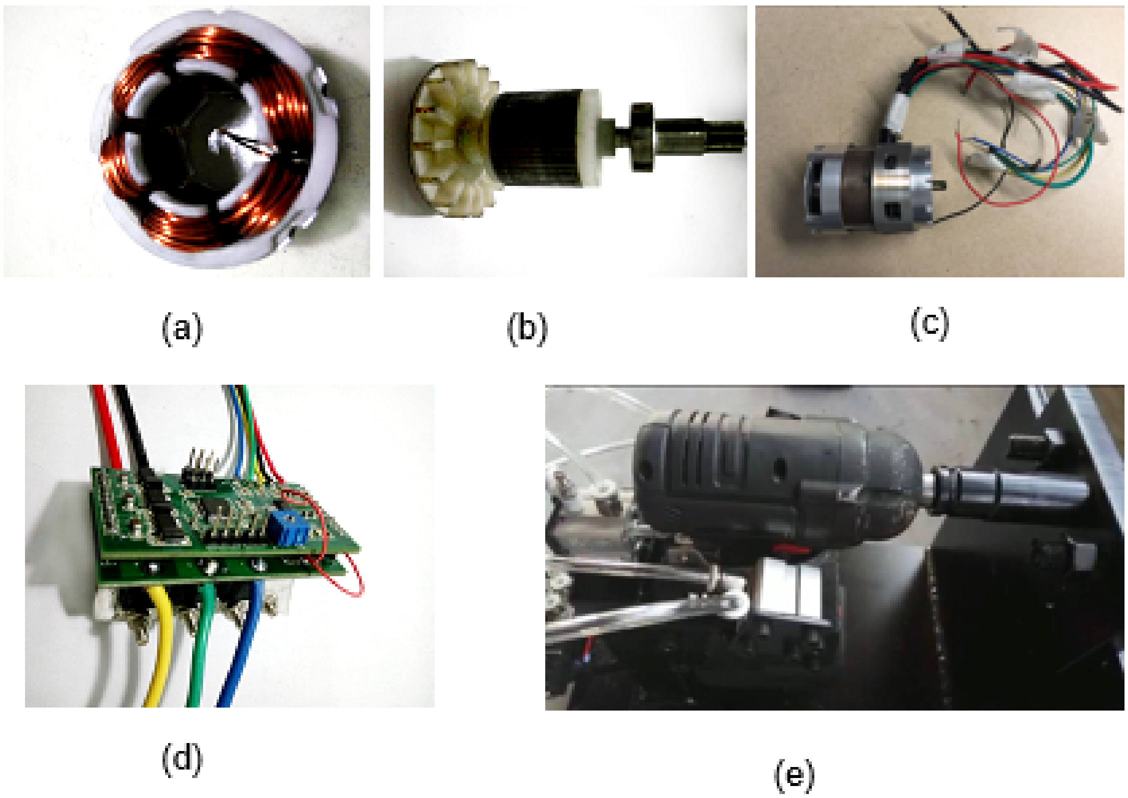

Figure 4.15: Prototype of IPMBLDC for electric impact wrench

The prototype is shown in Fig. 4.15. The induced back EMF of the IPMBLDC motor and hall sensor position of the IPMBLDC control board at low speed are shown in Fig. 4.16. The ampere-conductor distribution of the stator remains constant and fixed in space for a predetermined commutation interval while the magnet rotates past it, producing a linear variation in phase flux-linkage and from it a flat-topped EMF waveform.

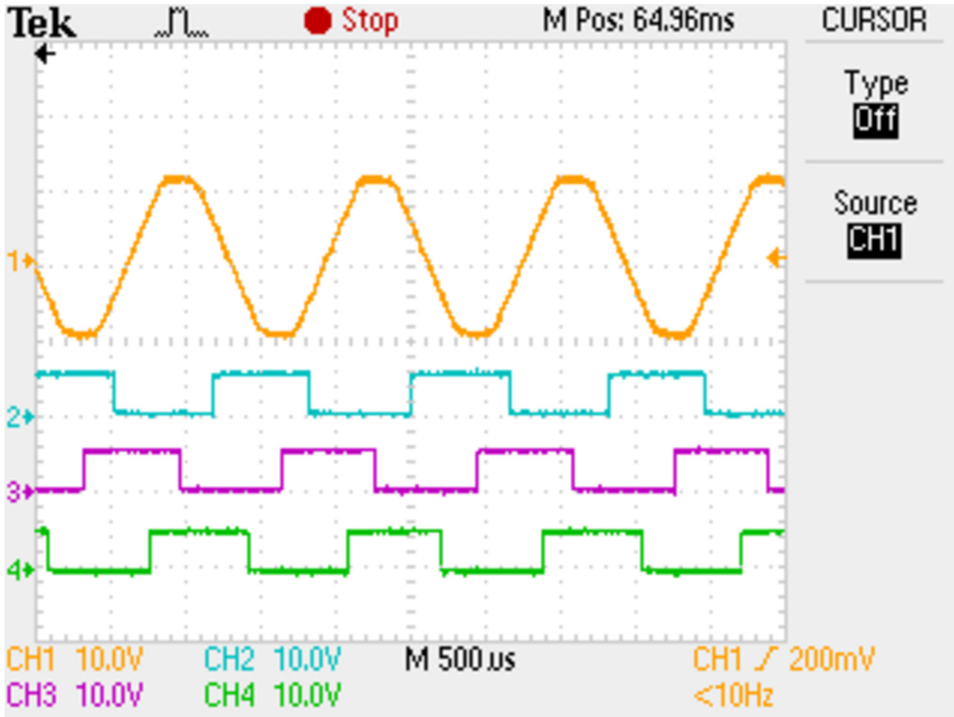

Figure 4.16: Oscilloscope trace of phase a inducted EMF and current waveform and signals form hall sensor board at low speed

We can see the flux density of air gap and Fast Fourier transform analysis of flux density of air gap at no load in Fig. 4.17 (a) and Fig. 4.17 (b) respectively. Even harmonics are canceled, only odd harmonics exist, which indicates the harmonics of air gap flux density distribution is good.

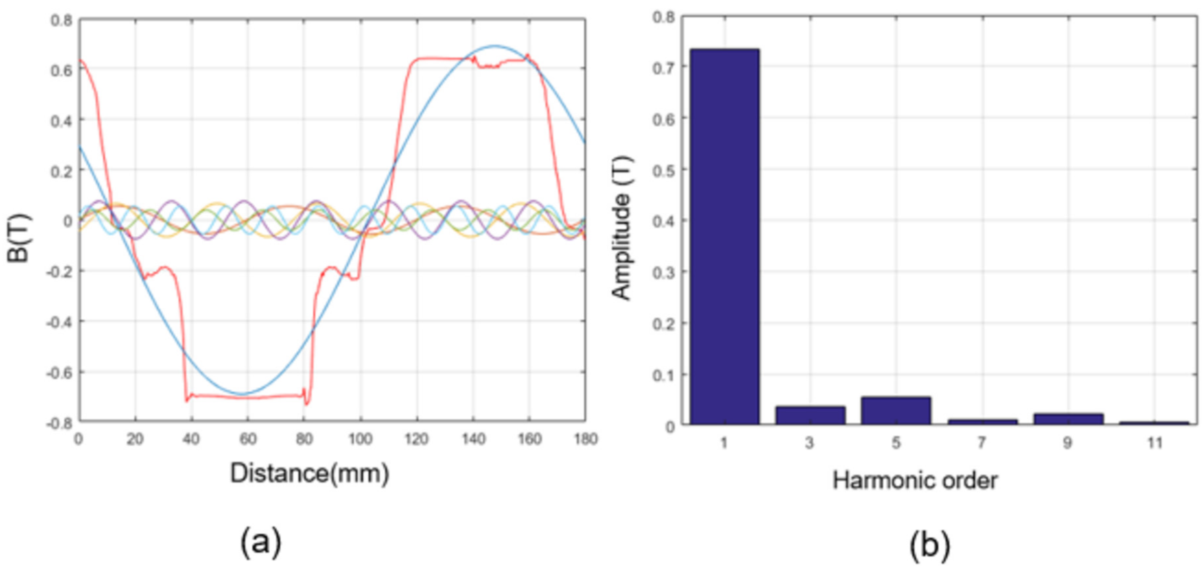

Figure 4.17: (a) The flux density of air gap (b) The FFT analysis of air gap

Fig. 4.18 (a) shows the testing and simulated results of IPMBLDC speed vs torque and current vs torque. We use the fixed torque wrench to load the bolt, then use the impact wrench to unload the bolt. As the torque increases, the motor speed decreases.The simulated speed of IPMBLDC at no load is around 2780 rpm, and the tested speed is a litter lower; the simulated speed decreases to around 1602 rpm, and the tested speed decreased to around 1375 rpm at maximum torque. The simulated current increased to 19A, and the tested current increased to 21A at the maximum torque as we can see from the Fig. 4.18 (b).

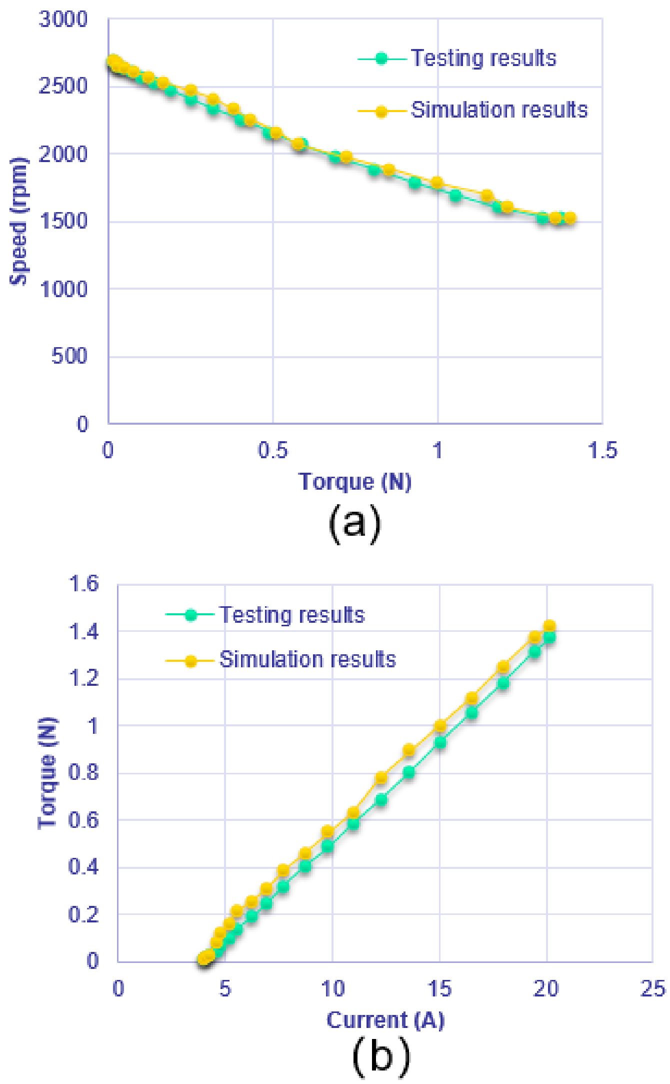

Figure 4.18: (a) Speed Vs torque (b) Torque Vs current

Fig. 4.19 shows the whole system of electrical wrench simulation efficiency is around 72% and testing efficiency is around 67 % at full load. When we do the simulation, we neglect some mechanical transmit losses, that is why the testing efficiency is 5% lower than simulation efficiency. The testing power loss includes the motor power losses, shock block system losses and some other mechanical losses.

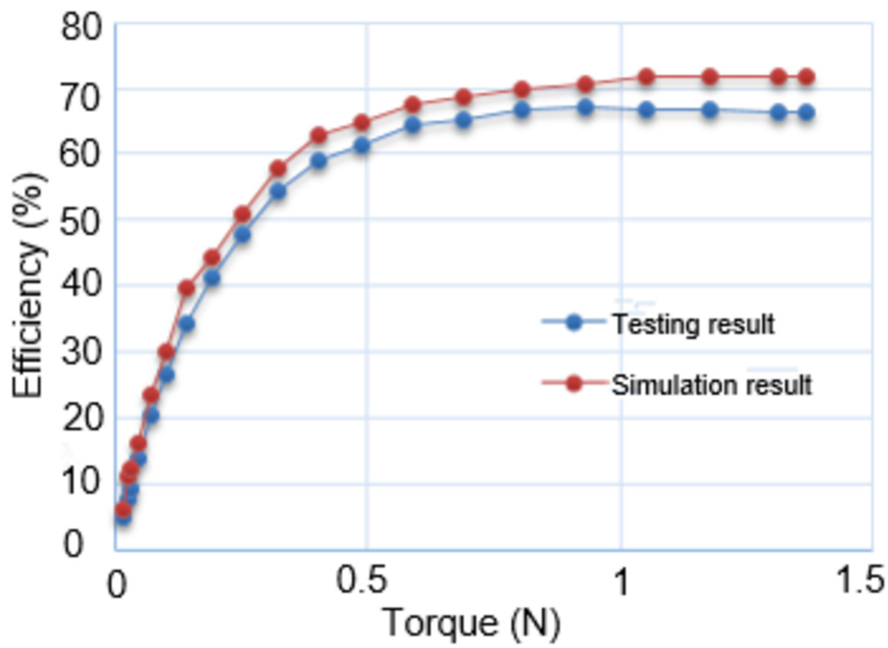

Figure 4.19: Efficiency Vs torque

Summary

In this chapter, an analytical method to design the IPMBLDC motor and a new mechanical transmission structure for electrical impact wrench step by step was introduced. The improved magnetic circuit model has been established to calculate the coefficient of the flux leakage and working point of a permanent magnet. Smaller torque is chosen to get the high pull-out torque. The design has been optimized and verified using MAXWELL 2D analysis based on the finite element method and MotorSlove packages. The motor has also been fabricated and can satisfy all the design requirements for electric impact wrench application. The new impact mechanical structure and working principle, the planetary gear reduce transmission ratio formula, as well as a dynamic model of main pressure spring and shock block in the impact process are also elaborated. The whole system of the impact wrench was fabricated as well.

CHAPTER 5: DESIGN AND ANALYSIS A HIGH EFFICIENCY PERMANENT MAGNET ALTERNATOR AND CONTROL SYSTEM FOR THE TRUCK AUXILIARY UNITS [1]

Introduction

Auxiliary power units(APUs) are normally equipped with the heavy-duty truck as shown in Fig 5.1 to supply power to air conditioners, heaters, electronics appliances and so on.

Figure 5.1: Auxiliary power units equipped with the heavy-duty truck

In this chapter, a 2kw high-efficiency alternator [66] [74] [90] [86] [41] and its control board system are designed, analyzed applying to the truck auxiliary power unit (APU) [106] [19] [48]

[1]The content in this chapter was partly published at *IECON* 2017 [41].

[8]to charge the battery and supply the 12V DC Power units. High-efficiency alternator [67] [77] is required for this application. The surface permanent magnet alternator [34] [31] is designed and fabricated based on the previous chapter theory because the surface permanent magnet alternator has less leakage and higher power density compared with interior permanent magnet alternator [39] [38]. The working point of a permanent magnet [85] [16] [43] should be selected when doing the design. The maximum power is reached when the working point of permanent is 0.5. In order to avoid demagnetization of the magnet [23] [37] [32], the working point should be selected higher than 0.5. A much smaller torque angle δ [82] [63] [111] than that in traditional design at relating load is used, which is between about 2 degrees and about 10 degrees. The design can utilize a smaller torque angle to get high overload capacity , which will increase the magnet thickness and air-gap size. The larger air-gap helps to reduce the wind-age loss and noise level, while the increased magnet thickness contributes to avoiding demagnetization. The relationship among the torque angle δ, working point, and the permanent magnet embrace [18] [112] [49] will be analyzed. The control system has two outputs : 48V DC and 14V DC. The alternator three phase outputs are connected to the there phase active rectifier to get 48V DC. SMO is used to get alternator position. Then, a buck converter with peak current control is applied to get 14V DC. the peak current control has advantage of a fast pulse-by-pulse short circuit and over-current load protection, which enhance the converter reliability. The control topology is shown below:

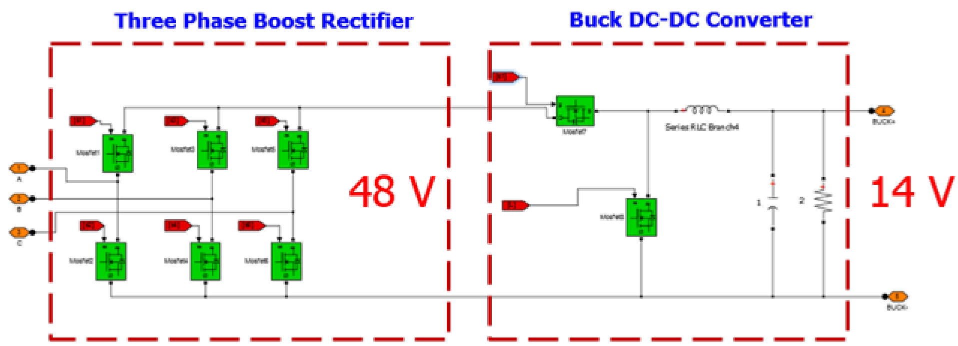

Figure 5.2: Alternator control topology

Copper loss [103] [50] [61] is the most significant of all the losses in low and medium speed electric machines. Reducing the copper loss is the key to build a highly efficient machine. To build a high-efficiency machine, we choose lower current density copper wires that have large wire cross-section, which reduce the copper loss and improve the efficiency. This also makes thermal management easier and avoids to use active cooling methodologies (such as fan, liquid cooling or spray cooling). Small torque angle is selected in design at the rated power and speed, which will result in large air age size, increased thickness of permanent magnets and high pull out torque. The machine will get high load capability, long lifetime, less mechanical noise and is not easy to demagnetization.

Analysis of Mathematic Model

From magnet thickness and air-gap equation, we can know that air-gap magnetic flux density value B_{rh} is a key design factor. The working point of a permanent magnet, permanent magnet embrace value affects the value of B_{rh}. The torque angle δ determines the peak value of the net magnetic

flux density and the peak winding magnetic flux density and it is also related to the pull-out torque and over-load capacity. The smaller the torque angle, the higher the pull-out torque and over-load capacity. The permanent magnet embrace is also related to the cogging torque and efficiency. After selecting the values of the working point and torque angle, the permanent magnet embrace will play a role in the design. Normally we selected the value of magnet embrace is around 0.8. Fig. 5.3 and Fig. 5.4 show how the embrace affects the magnet thickness, air-gap values based on chapter two design equation. The plots are based on a 2Kw, 6000rpm generator with 0.8 working point and selected 10-degree torque angle. We can see that when the value of embrace increase the magnet thickness and air-gap thickness values decrease because the increased embraced value will increase the $B_{a,pk}$ and $B_{g,pk}$ values.

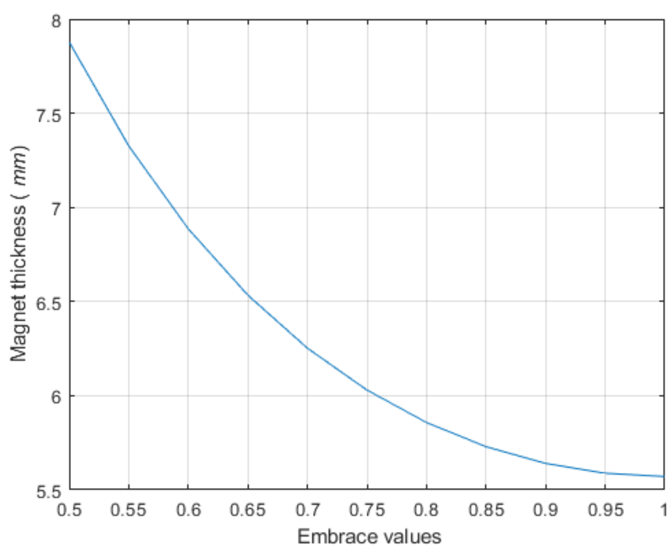

Figure 5.3: Embrace values Vs magnet thickness values

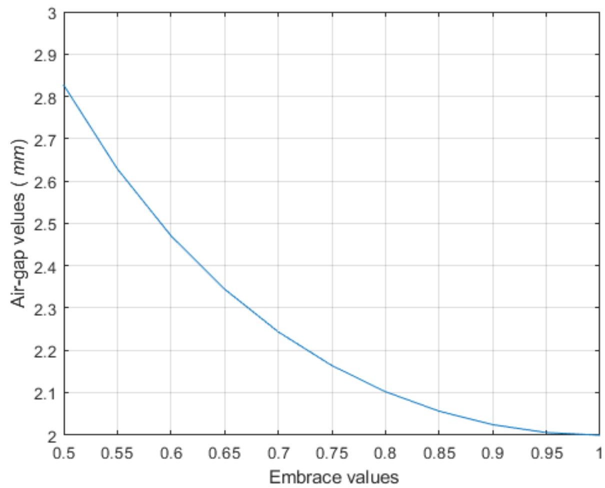

Figure 5.4: Embrace values Vs air-gap values

Alternator Model

Table 5.1: Results of the alternator design

Parameters	Unit	Specification
Magnetic material	-	NdFeB-38
Cool method	-	air
Rated Power	kW	2
Number of magnet poles	-	4
Number of stator slots	-	36
Stator outer diameter	mm	157
Stator inner diameter	mm	79
Airgap length	mm	2
Magnet width	mm	6
Magnet length	mm	23

A alternator with 0.8 working point, 10-degree torque angle, and 0.75 embrace value was designed and fabricated based on the design method. The magnet thickness value is selected to be $6mm$,

and air-gap length is chosen to be $2mm$ after the optimization. The air-gap thickness is slightly less than the simulation value $2.15mm$ considering the fabrication process. After the analysis, the dimensions of the alternator are obtained as shown in Table 5.1. The alternator windings diagrammatic drawing is shown in Fig. 5.5.

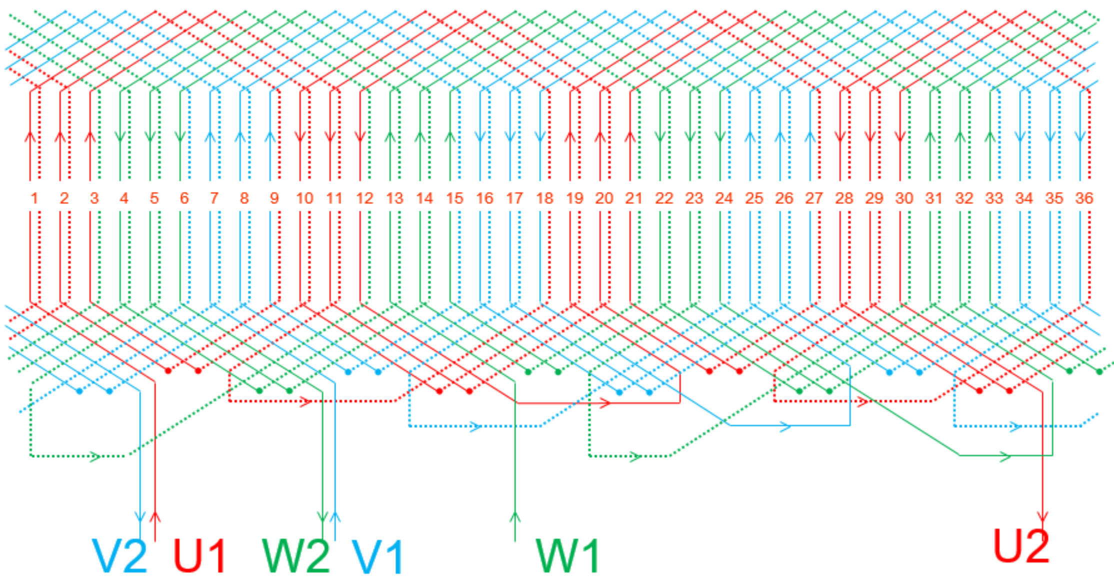

Figure 5.5: Alternator windings connection

ANSYS Maxwell 2D is used to evaluate and optimize our design. Parameters such as slot size and shape, magnet thickness, air-gap size and yoke thickness, and so on have been optimized using the software. Fig 5.6 shows the distribution of magnetic flux density. It can be seen that the tooth flux density is limited to 1.1T and the maximum flux density of the yoke is around 1.45T. Fig. 5.7 shows the calculated efficiency of the alternator versus RMS phase current. It can be seen that the motor has a very high efficiency (around 97%) at the rated power.

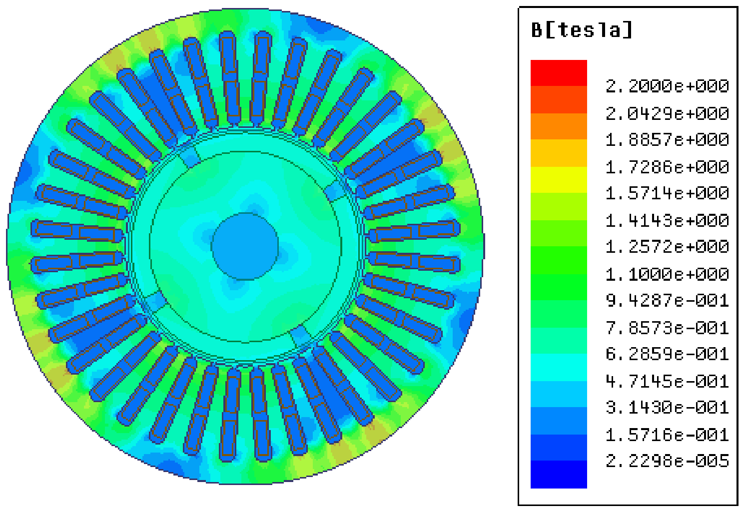

Figure 5.6: Flux density in the alternator

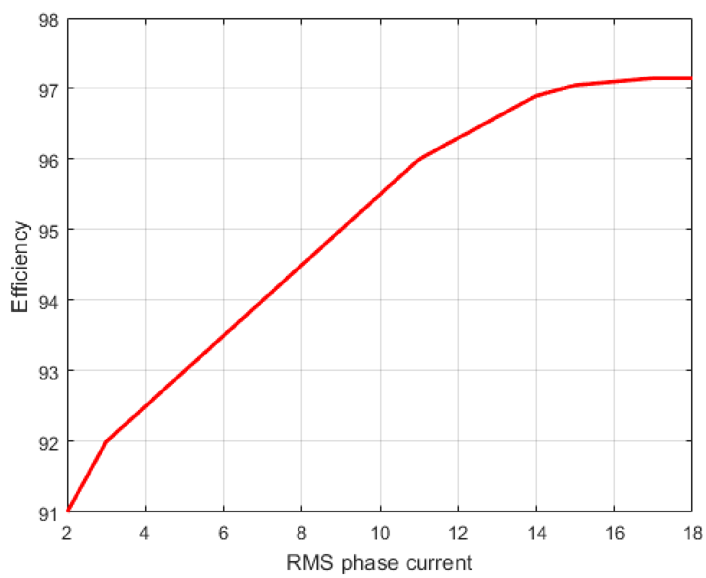

Figure 5.7: Efficiency Vs. RMS phase current

Fig. 5.8 shows flux linkage is good sinusoidal shape, which indicates the magnetic does not saturate with high excitation. Thus, the distortion of EMF should not appear across the zero point. Besides the amplitude of A, B and C phases flux linkage are almost the same, which can be explained as that the fringing effect is minimal. Fig. 5.9 shows the cogging torque versus time. It shows that the cogging torque is low. The cogging torque peak value is around 0.015 N.

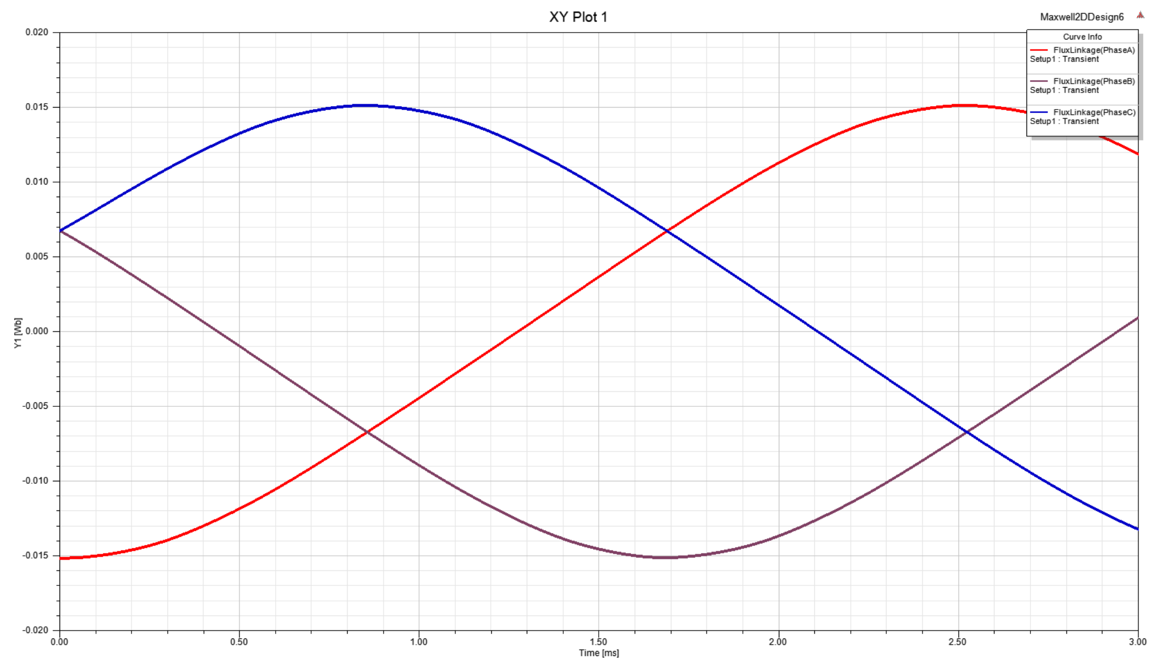

Figure 5.8: Phase flux Vs time

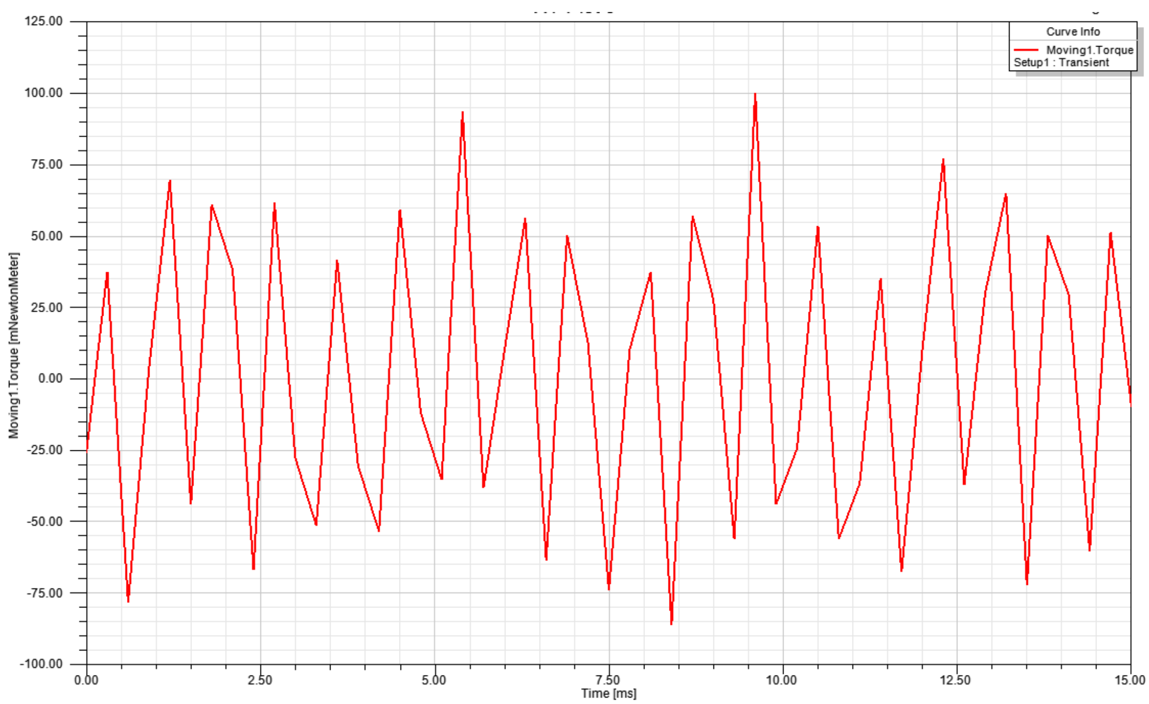

Figure 5.9: Cogging torque Vs time

Thermal Analyze

The housing is designed and the thermal performance of each part of the generator are analyzed as shown in Fig. 5.10. The peak temperature inside the generator is around 342K at the full load, which is below 350K and therefore the active cooling methodologies are not needed.

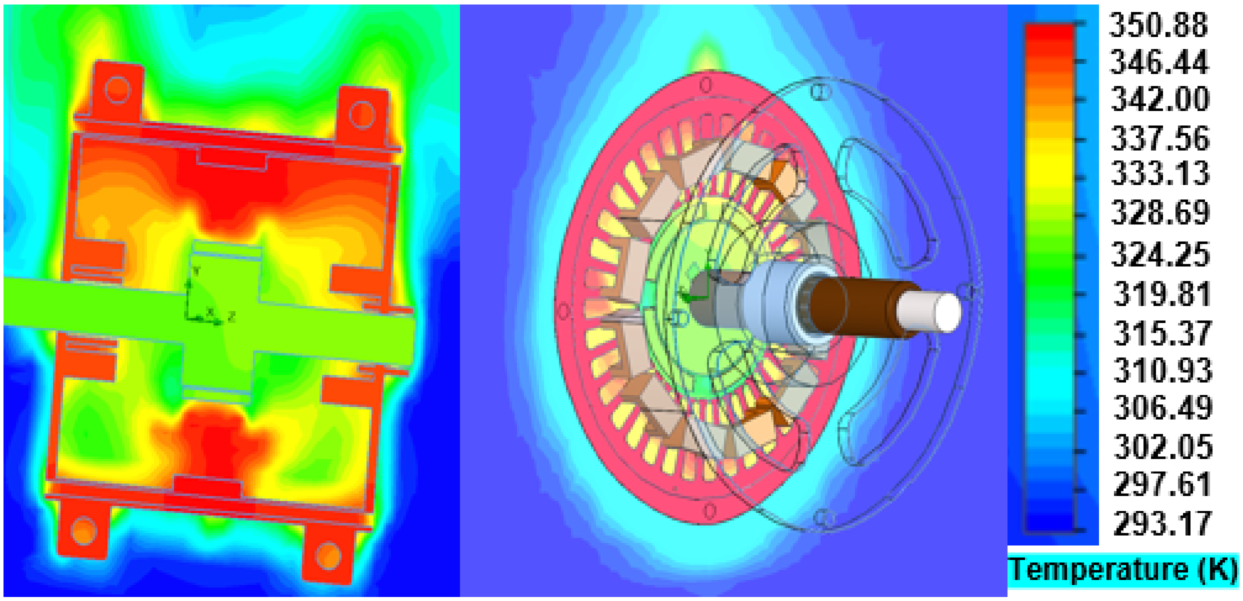

Figure 5.10: The simulation of alternator temperature of each parts

Simulation Control Topology of The Whole Alternator System

The MATLAB simulation model of the whole system control topology was built. It contains two stages : three phase active rectifier and buck converter. The SMO is used to get the rotor position for the fist stage and the filed oriented control is applied to the alternator control. The 48V is transfered from the alternator three phase outputs using the three phase active rectifier. The buck converter is designed as second stage to get 14V DC to charger the 14V unites. The whole control topology is shown below.

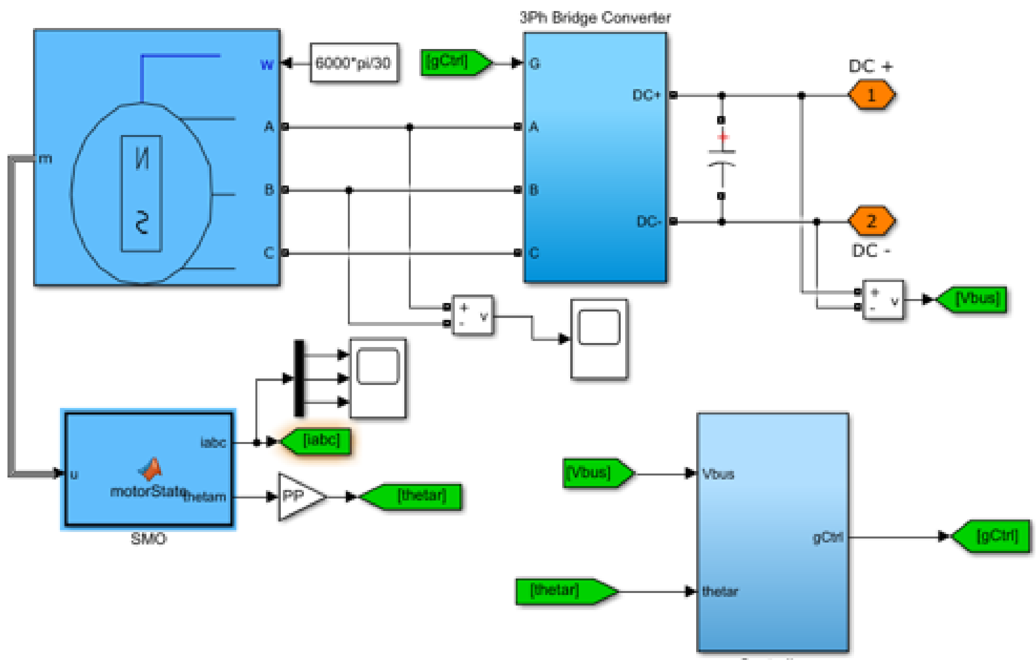

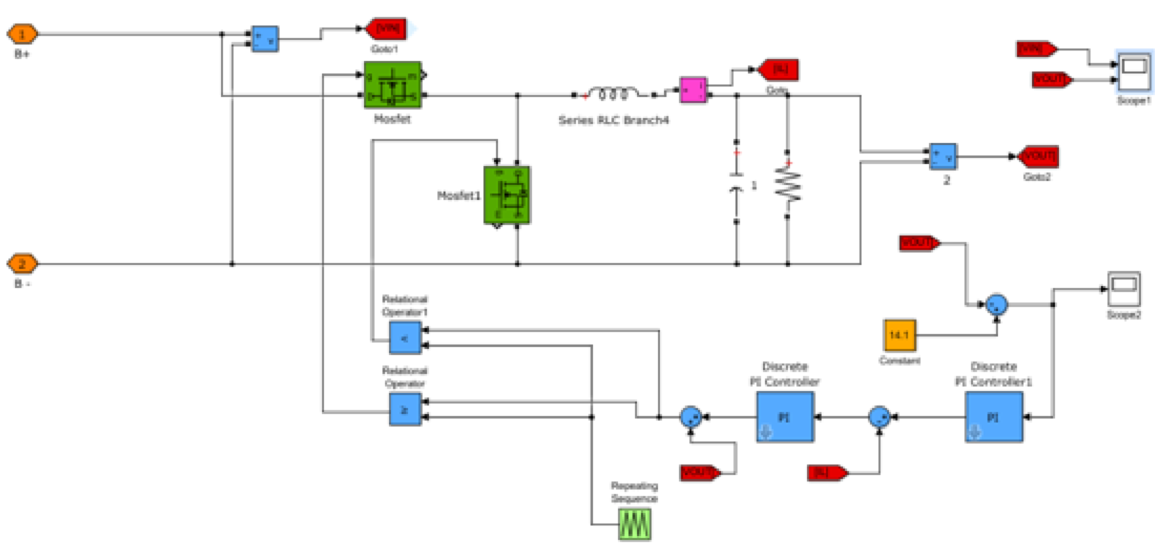

Figure 5.11: The simulation model of the whole alternator control system

The Fig. 5.12 shows the estimated rotor position and the actual rotor position. It can be clearly seen that the rotor position from SMO can match the actual rotor position.

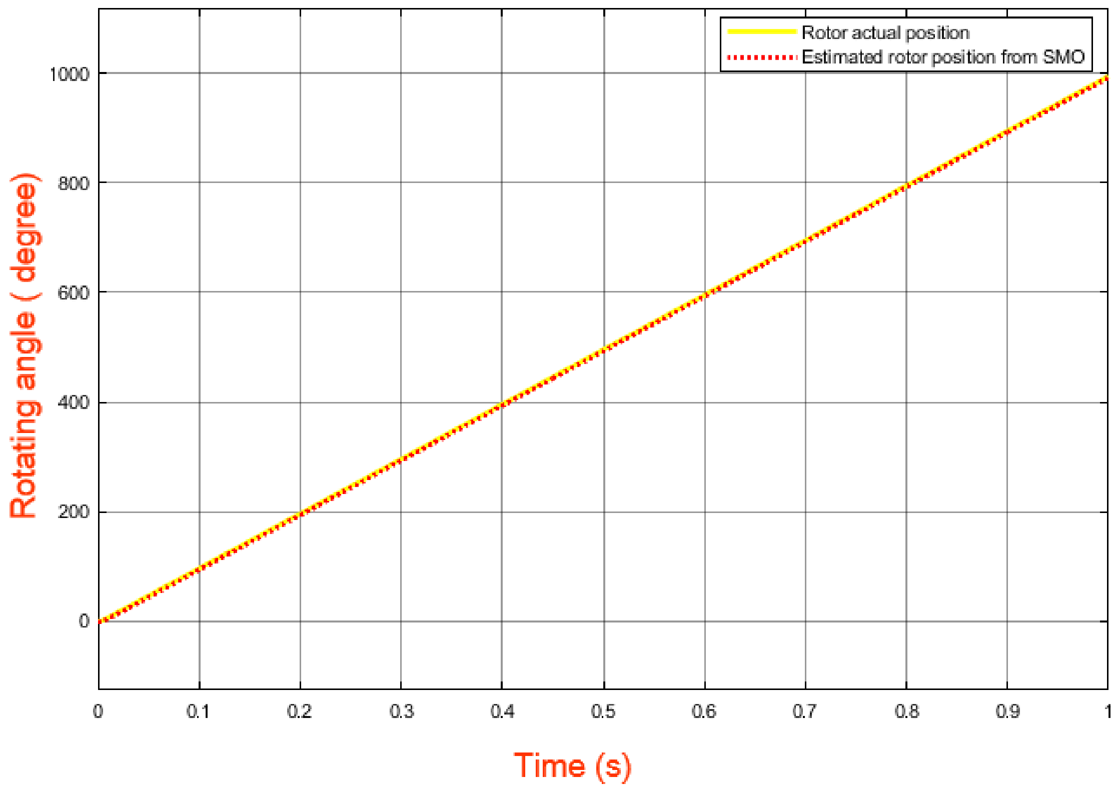

Figure 5.12: The estimated rotor position and the actual rotor position

The correct rotor position information is the key of the control topology, then the 48V can be obtained from field oriented control, which is shown below.

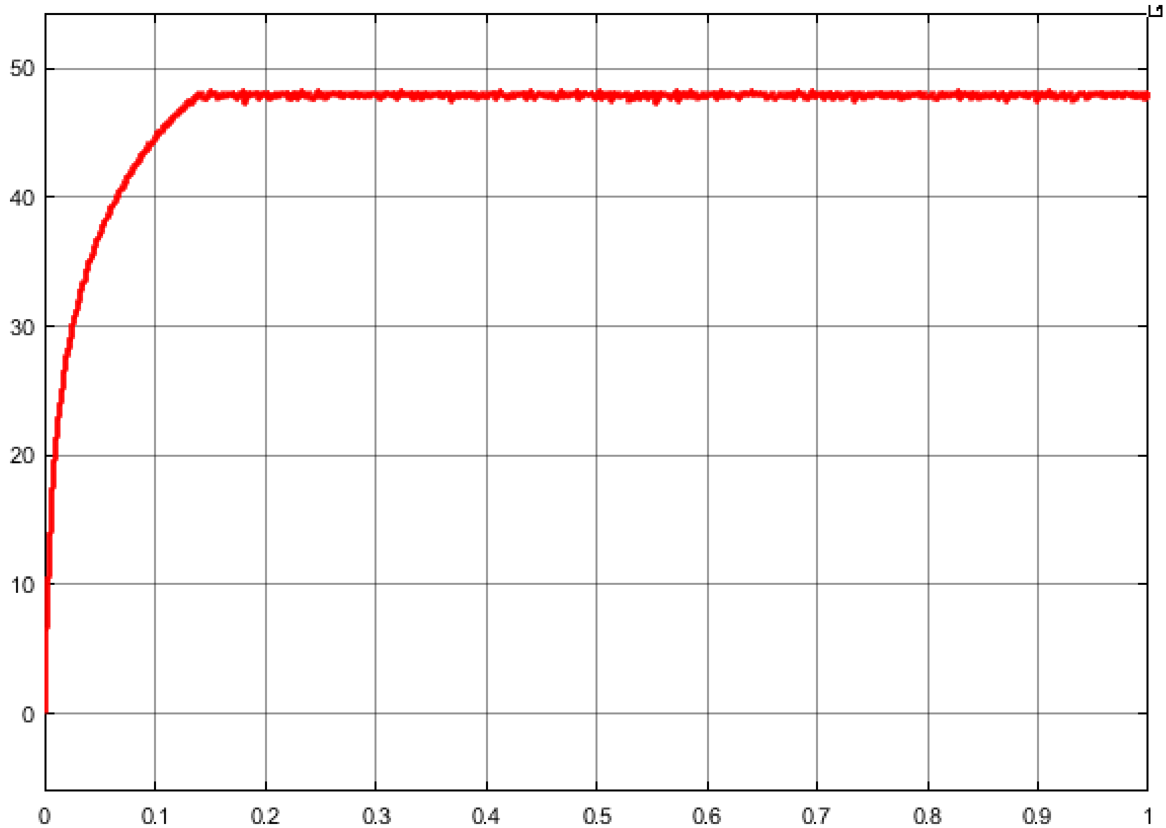

Figure 5.13: Three phase active rectifier output

The peaking current control is applied to buck converter to get the 14V DC. The Fig. 5.14 shows the simulation result from the MATLAB.

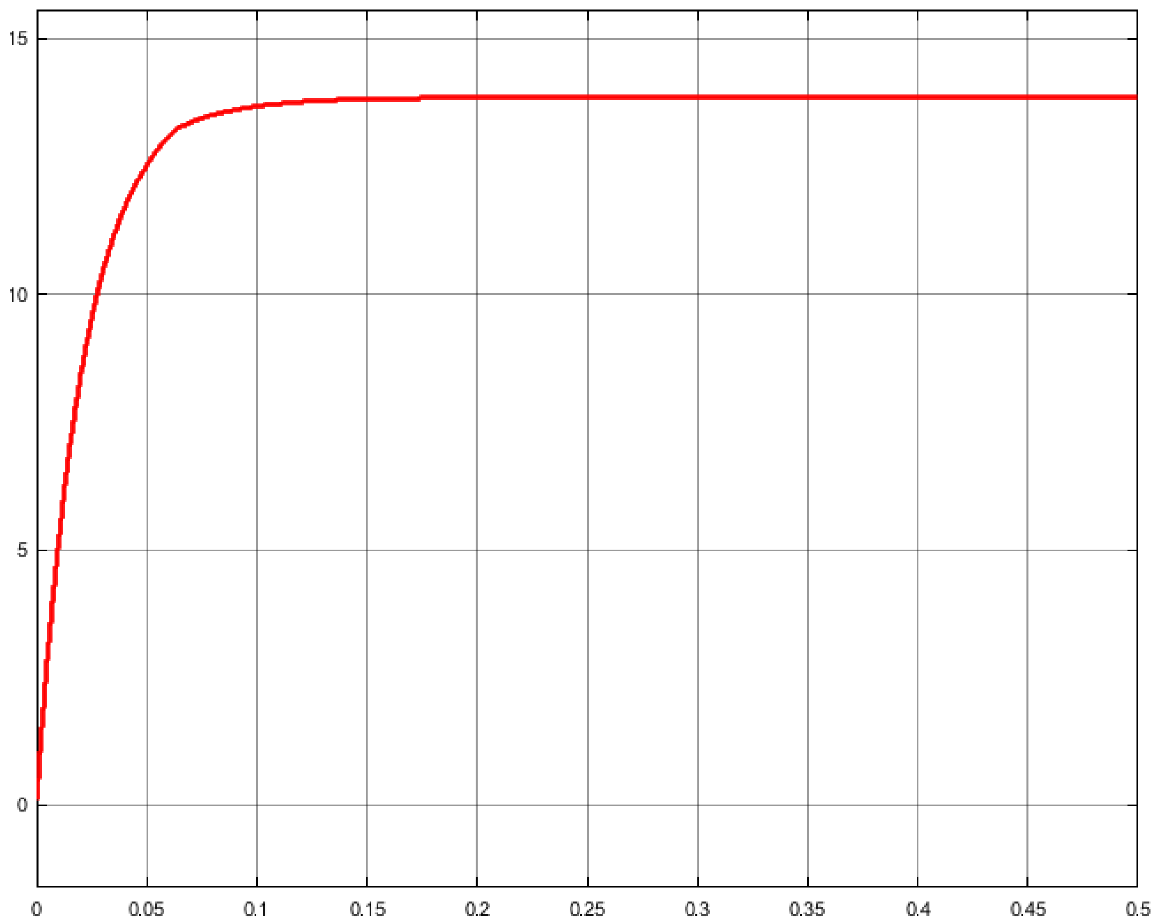

Figure 5.14: The second stage output

The flux density of the air-gap and no-load air-gap flux density Four transform analysis are shown in Fig. 5.15. It indicates that the even harmonics are canceled, only odd harmonics exist.

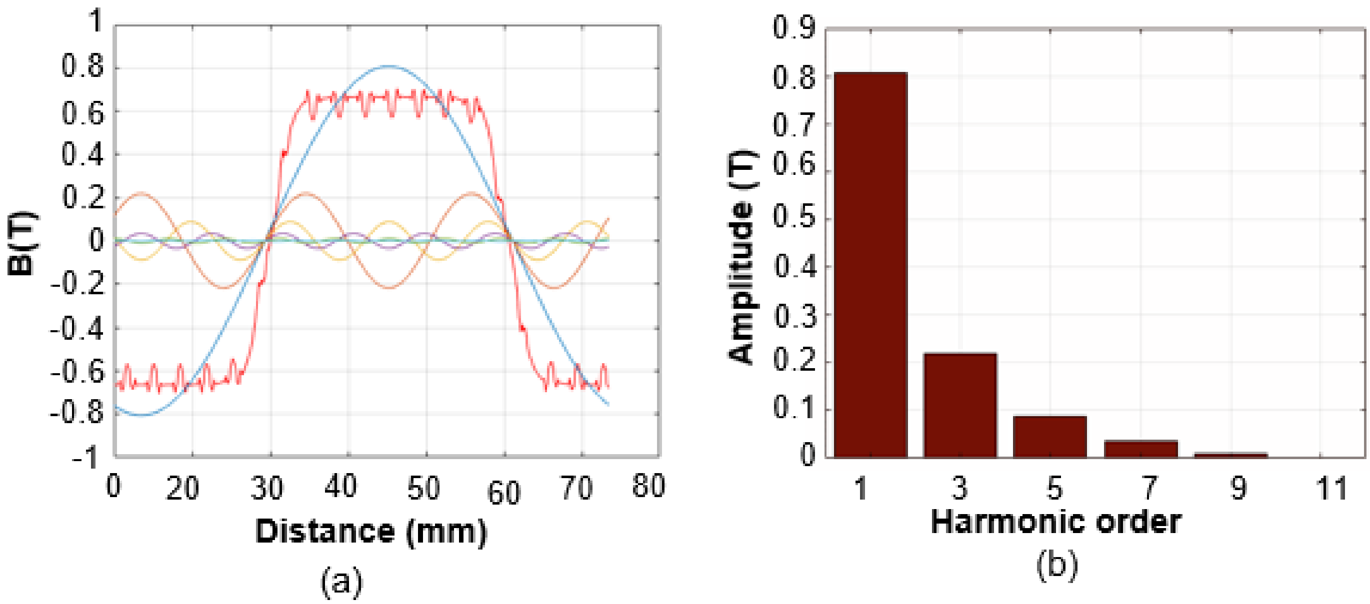

Figure 5.15: (a) The flux density of air-gap and different order harmonic waveforms showing with different color; (b) The fast Fourier transformation (FFT) analysis of air-gap.

Alternator and Control Board Prototype

The alternator prototypes are shown in Fig. 5.16. We use lamination technique to reduce the core loss. The lamination factor is 0.92.

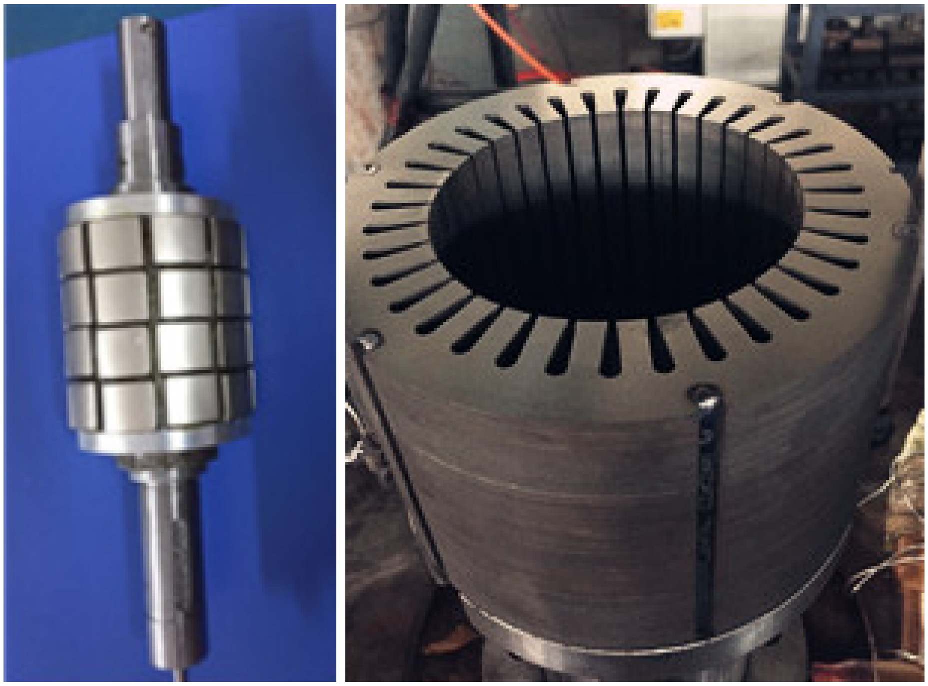

Figure 5.16: The alternator stator and rotor prototype

In order to get perfect heat dissipation performance and increasing load capability and lifetime, we soldered the MOSFETS on the aluminum board for high power and use the copper bars to connect the PCB board and aluminum board.

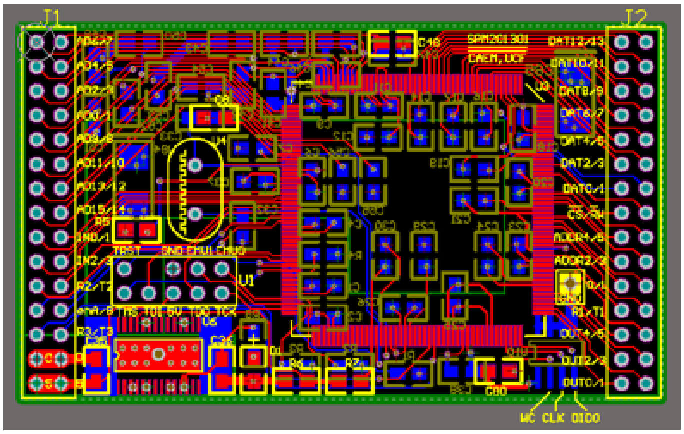

(a) DSP28335 Minimum board

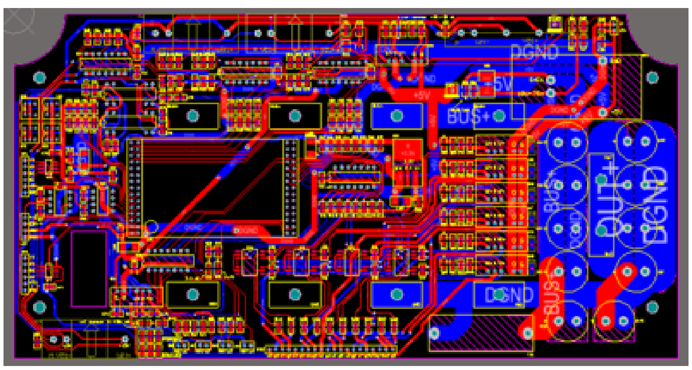

(b) Alternator control board

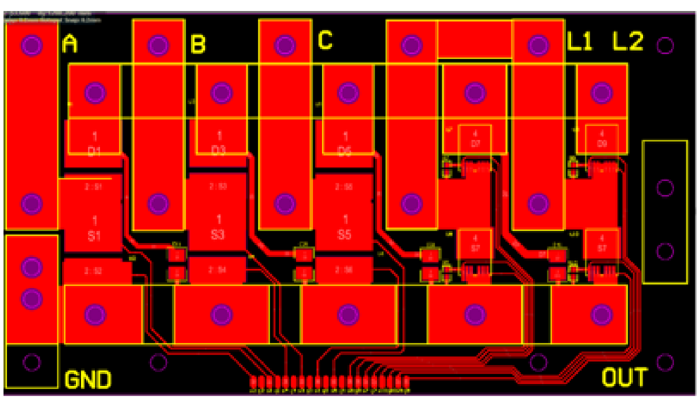

(c) Aluminum board

Figure 5.17: PCB layout of the alternator control board

The fabricated alternator control board is shown in Fig. 5.18. The DSPF28335 is selected as CPU and the DSPF28335 minimum board is connected to the PCB main board. The high frequency and large current inductor also has been designed and fabricated for the buck converter using area production method.

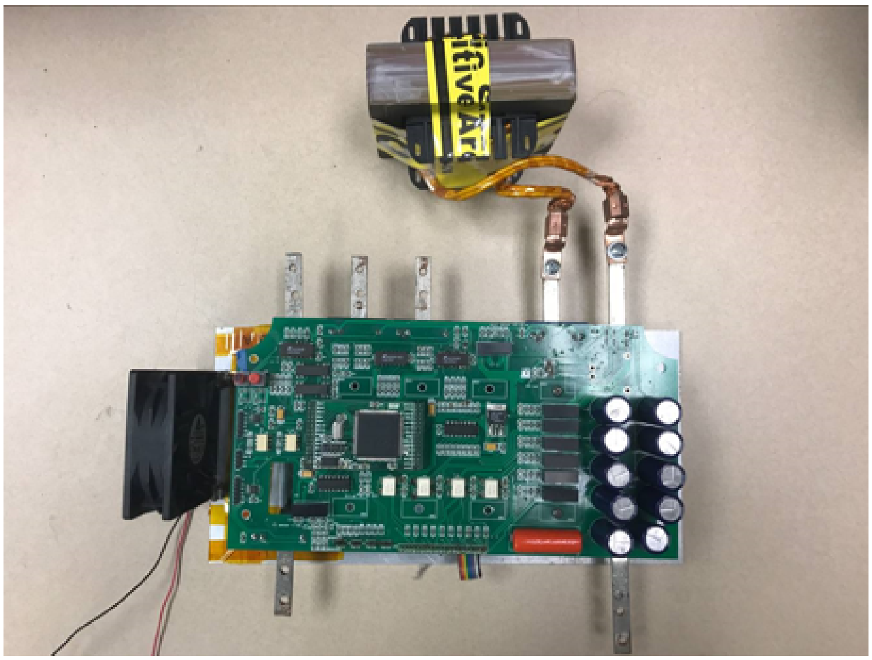

Figure 5.18: The fabricated alternator whole system control board

Alternator Whole System Testing

The whole system control process is shown in Fig. 5.19, the testing was did based on it.

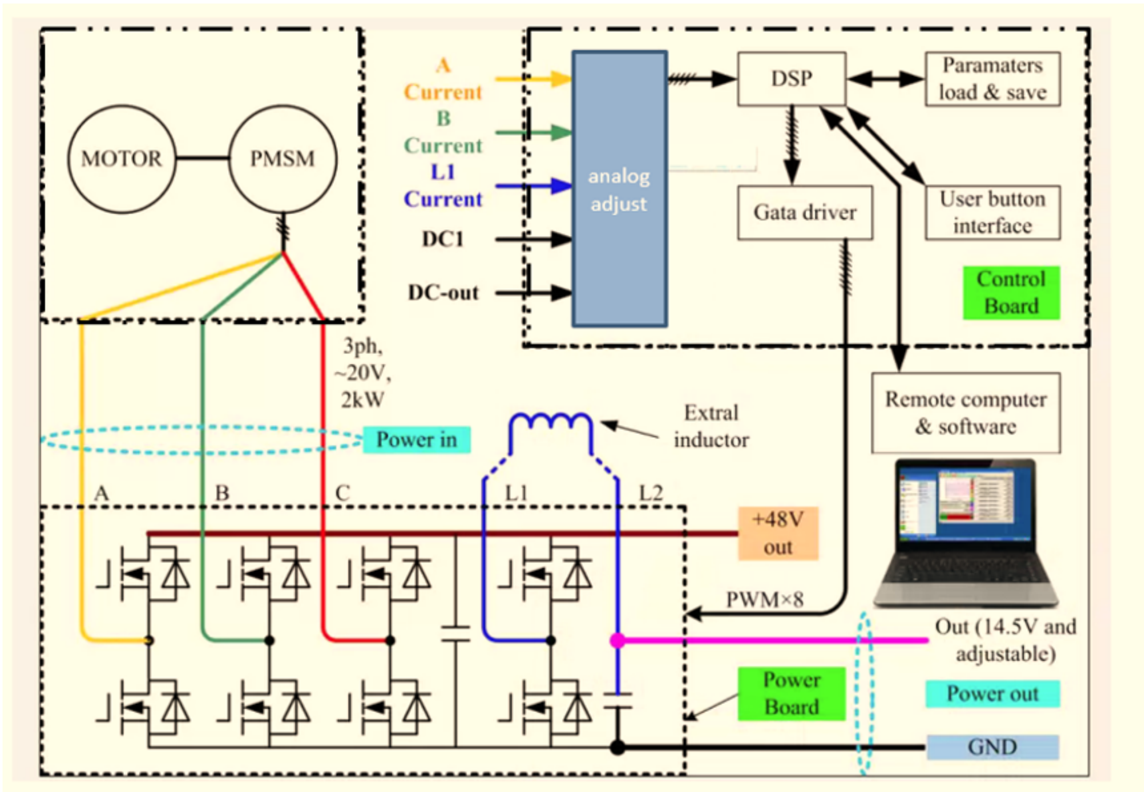

Figure 5.19: The whole system control process

A permanent magnet motor is used to drive the alternator. The alternator three phase outputs are connected to the control board to get DC output. The resistors are connected in parallel as loads as shown in Fig. 5.20.

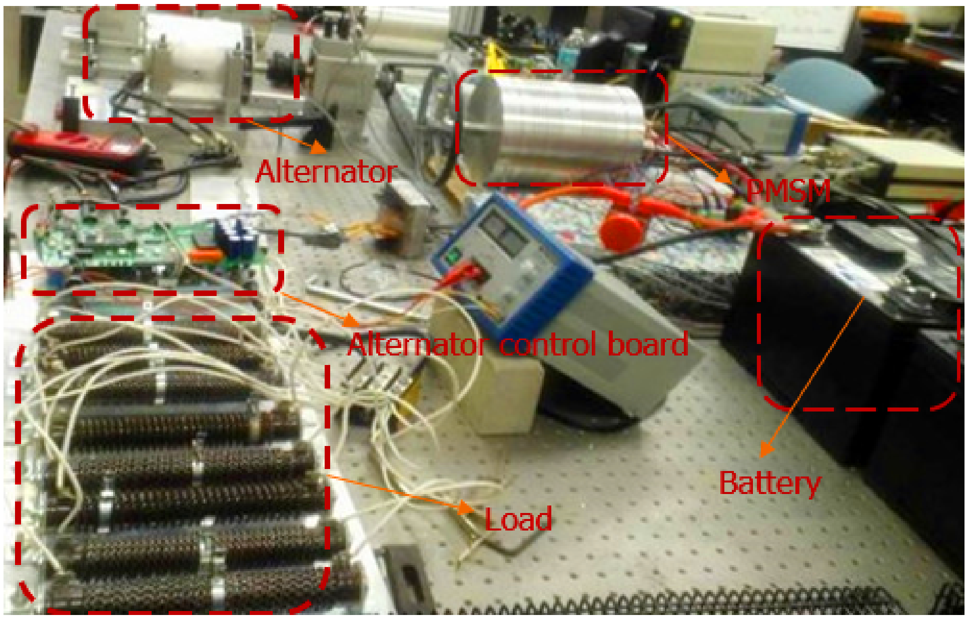

Figure 5.20: The alternator testing system

We can see the three phase currents in Fig. 5.21. The waveforms are not perfect sine wave due to harmonics.

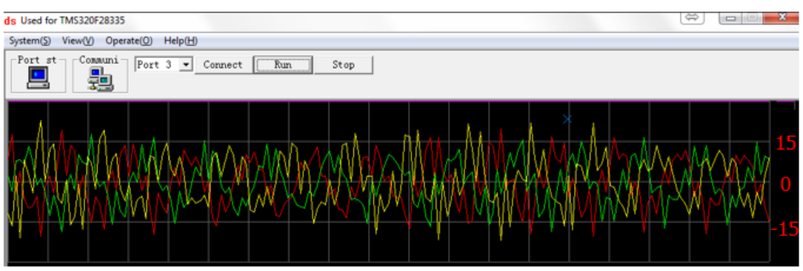

Figure 5.21: Alternator three phase current

Finally, the efficiency of the alternator under different loads has been tested as shown in Fig. 5.22,

which indicates the design of alternator has high efficiency. The efficiency is around 95 % at the rated load, which is 2% lower than the simulation values. Because when we do the simulation, we ignore some factors effect.

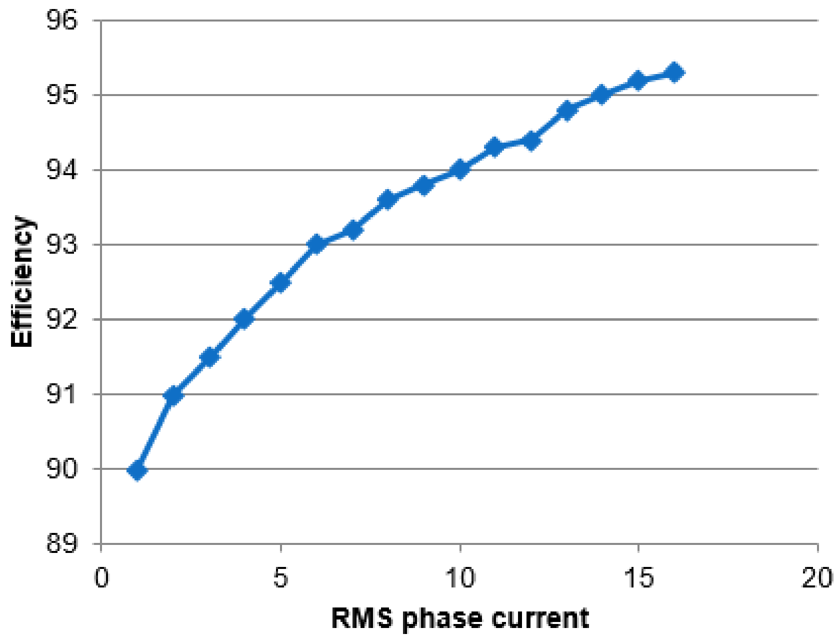

Figure 5.22: Three phase RMS current Vs efficiency

Summary

A truck alternator and its control system applying to APU system has been successfully design, fabricated and tested. 36-slot, 4-pole topology with surface-mounted permanent magnets and a double layer lap winding scheme is selected in our design. Motor structure consideration, key points of design and design procedures are introduced in detail. The design has been optimized and verified using MAXWELL 2D analysis based on the finite element method. We also created the housing and did the thermal analysis for our alternator. The heat dissipation performance of our alternator is pretty good, and no fan is required in our design. The sigmoid function SMO sensor-less control method is applied to the control system. Ti DSP 28335 MCU is selected as control CPU. The control PCB board is designed and fabricated. The Whole alternator system has also been completely fabricated. The simulation and test results show the whole system performers pretty well.

CHAPTER 6: CONCLUSION

The dissertation focus on the high-efficiency electrical machinery design and control. The design method was introduced step by step. The dynamic modeling of the permanent magnet motor was built and analyzed. The advantage of the design method is that it can increase the high load capacity at no cost of increasing the total machine size. A much smaller torque angle than that in the traditional design at relating load is selected, which is between about 2 degrees and about 10 degrees. According to the design method relating to the much smaller torque angle, which will increase air-gap size and larger magnet thickness. The windage loss and noise level will be reduced because of larger air-gap size. The increased magnet thickness is contributed to avoid demagnetization. The larger air-gap sized and increased magnet thickness contribute to increase efficiency and overload capability. Based on the design method, all the parameters will be related to the torque angle, working point of a permanent magnet, and the permanent magnet embrace, which is easier for the designer to make a new design.

An interior permanent magnet brush-less DC electric motor (IPMBLDC) for a kind of electric impact wrench used for loading and unloading car bolts is designed and fabricated based on the design method. This kind of motor works on the discontinuous model. High pull-out torque and small size is required. Based on the design method, that two requirements can be satisfied when doing the BLDC design. Maxwell 2D FEM model is built to simulate and optimize the design. Thermal analysis is given to simulate the temperature rise of all parts of the motor. The new impact wrench mechanical structure is also designed. the It provides an analytical whole system design method for the impact wrench system, which can be used for the other functional electric tools whole system design.

An advanced Sliding Mode Observer (SMO) is designed for the alternator system, which can get

the rotor position more accurate. The high-efficiency alternator is designed and fabricated based on the design method. The alternator system is applied to the truck auxiliary power unit (APU), which has two outputs (48V and 14V). All the Matlab simulation model, MAXWELL 2D model, and PCB board are done. The whole system efficiency is much higher than the traditional system using induction motor.

List of Symbols

A_m	Cross section area of the magnets.
A_g	Cross section area of the air-gap.
b	Pole shoe arc length.
b_m	Magnet width.
$B_{core,pk}$	Core peak flux density.
$B_{g,peak}$	Air-gap peak flux density.
B_{tooth}	Tooth flux density.
B_r	Remanent flux-density.
$B_{a,peak}$	Peak winding magnetic density.
c	Coefficient of firection.
C_s	Spring index.
d_y	Yoke thickness.
d_m	The magnetic thickness.
D	Stator bore inner diameter.
D_r	Total rotor diameter including magnet.
D_i	Rotor inner diameter.
D_c, d_c	Out and inner diameter of a shock block coil.
e_m	Embrace of the permanent magnet.

e_{PM}	The permanent magnet flux linkage induced back EMF.
e_α, e_β	Back EMF in the stationary frame.
$\widetilde{e_\alpha}$, $\widetilde{e_\alpha}$	Back EMF error in α, β frame.
E	Energy produced by shock block every minute.
ΔE_1	Energy difference before and after impact.
E_1	Storing energy before impact.
f_e	Electrical frequency of phase voltage.
F_m	Permanent magnet MMF.
F_g	Air-gap MMF.
F_{total}	The total MMF.
F_g, F_{st}	MMF of air-gap and stator tooth.
F_{sy}, F_{ry}	MMF of stator yoke and rotor yoke.
F_1, F_2, F_3	The minimum, maximum, and average load on the spring.
g	The actual air-gap size.
$\hat{g}_{total}$	Initial total effective air-gap size.
g'_{total}	Effective air-gap size with magnet thickness.
G	Shear modulus of elasticity.
h_m	Magnet length.
H_g	The air-gap magnetic field.

H_m	The PM magnetic field.
H_c	Magnet Coercive field strength.
i_α, i_β	Phase current in the stationary frame.
$\hat{i}_\alpha \ \hat{i}_\beta$	Estimated current in the stationary reference frame.
$\tilde{i}_r$	Planetary gear ratio.
$I_{p,rated}$	Rated phase current.
$\boldsymbol{I_{abc}}$	Stator current in the abc frame.
$\boldsymbol{I_{dq0}}$	Stator current in the dq frame.
i_{dref}	Referenced d axis current.
i_{qref}	Referenced q axis current.
J	Initial moment of the rotor.
J_s	Current density.
J'	Converted inertia of the impact system.
k	Spring constant.
k_w	The winding factor.
k_c	Carter's coefficient.
k_{ls}	The leakage flux coefficient.
k_i	Insulation coefficient.
k_{ph}	Pitch factor for the h^{th} harmonic.
k	spring constant.

K_s	Motor saturation factor.
K_α	Rotor structure factor.
K_ϕ	Air-gap flux waveform factor.
K_h	Coefficient of the hysteresis loss.
l_e	Stator effective length including fringing due to ducts.
L	Stator core length (not including air ducts and fringing).
L_{aa}, L_{bb}, L_{cc}	Stator self-inductances.
L_{ab}, L_{bc}, L_{ac}	Stator-to stator mutual inductances.
L_{lf}	Leakage inductance of field winding.
L_1	Inductance corresponding to the constant component of the air-gap permeance
L_2	Inductance component corresponding to the component of air-gap permeance which varies with rotor angle.
L_s	The stator phase inductance.
L_{im}	Impact stroke length.
m	Shock block quality.
m_1, m_2	One of the two different steel tubes quality.
m_3	Two fan-shape claws quality.
M_F	Resistance torque of the spring to the mandrel.
n_1, n_2, n_3	Speed of sun gear, ring, and plant gear.

$\hat{N}$	The effective number of series turns per phase.
N_s	The number of stator slots.
N_c	The number of turns per coil.
N_a	The number of series turns per phase.
N_p	Number of poles.
N_1, N_2	Total numbers and active numbers of pressure spring winding.
P_r	Required output power.
P_{mecg}	Mechanical power.
P_c	Permeance coefficient.
P_{copper}	Copper loss.
P_h	Hysteresis loss.
P_e	Eddy-current loss.
P_c	The total core loss.
q	The number of the winding groups per pole.
r_a	The inner radius of the rotor.
r_s	Ratio of slot width and slot pitch.
r_g	The radius of the actual air-gap.
r_{is}	The total length of inner radius, magnet thickness and effective air-gap size without magnet thickness.
r_o	Ball to spindle center distance.

R_s	The stator phase resistance.
R_m	Permanent magnet reluctance per pole.
R_g	Air-gap reluctance per pole.
R_{ml}	Reluctances of the magnet end flux leakage.
R_{mm}	Reluctances of the magnet to magnet flux leakage.
R_σ	Magnet end flux leakage reluctance.
R_{sy}	Reluctances of stator yoke.
R_{st}	Reluctances of stator tooth.
R_g	Reluctances of air-gap.
R_{rya}	Reluctances of rotor yoke above the magnet.
R_{ryb}	Reluctances of rotor yoke below the magnet.
R_z	Total reluctance of air-gap.
R_{mo}	Magnet reluctances.
R_0	Sum of magnet end flux leakage reluctances and magnet reluctance.
$\hat{R}_s$	The stator estimated phase resistance in the stationary reference frame.
S_{off}	Slot offsets to other winding phases.
S_c	Nominal coil span in slots.
S	A stator quantity to be transformed (current, voltage, or flux).
S_1, S_2	Minimum and maximum amount of elastic deformation.
t_{lam}	lamination thickness.

t_b	Time of tighten a bolt.
T_m	Related mechanical torque.
T_L	Load torque.
T_a, T_b, T_c	Dwell time.
u_α, u_β	Phase voltage in the stationary frame.
V_Φ	Phase voltage.
$V_{\Phi,rated}$	Rated phase voltage.
$\boldsymbol{V_{abc}}$	Stator winding voltage in the abc frame.
$\boldsymbol{V_{dq0}}$	Stator winding voltage in the dq frame.
z_1	Tooth numbers of sun gear.
z_3	Tooth numbers of ring.
α_p	Pole arc coefficient.
α_m	Working point of permanent magnet.
$\dot{\Gamma}$	The stability condition function.
δ	Torque angle.
η	Efficiency of energy transmission.
$\hat{\eta}$	Average theory impact efficiency.
θ	Power angle.
θ_a	Phase A reference angle.

$\theta_{slot}(k)$	The relative electrical angle(expressed in the range of -180° to 180° of the kth slot
$\theta_{coil}(k)$	The relative electrical angle of in slot of the kth coil
θ_m	Rotor electrical angle.
θ_{me}	Poles/2 times the rotor electrical angle.
$\tilde{\theta_m}$	Position signal obtained through observer without phase delay.
$\boldsymbol{\lambda_{abc}}$	The current flux-linkage in the abc frame.
$\boldsymbol{\lambda_{dq0}}$	The current flux-linkage in the dq frame.
$\boldsymbol{\lambda_{PMabc}}$	The permanent magnet flux-linkage in the abc frame.
$\boldsymbol{\lambda_{dqabc}}$	The permanent magnet flux-linkage in the dq frame.
λ_δ	Main magnetic permeability.
μ_0	Permeability of air.
μ_r	Relative permeability.
ρ_{copper}	The resistivity of the copper.
ρ_{PM}	Magnet electrical angle.
ρ_m	The mass density.
σ	The conductivity.
τ_1	Polar distance.
τ_p	Pole pitch.
τ_s	Slot pitch.

Φ_{core}	Air-gap flux.
$\Phi_{g,pk}$	The peak flux of air-gap.
Φ_{tooth}	One stator tooth flux.
Φ_{σ}	Total flux leakage.
Φ_{ml}	Magnet end flux leakage.
Φ_{mm}	Magnet to magnet flux leakage.
ξ_{δ}	Per-unit value of the main magnetic permeability.
ψ_{f}	Flux linkage of the Permanetn magnet synchronous motor (PMSM).
ϖ_{0}	Cooling coefficient.
φ_{s}	Slot pitch.
ω	The rotor rotational speed.
ω_{r}	Electrical angular velocity of the rotor.
ω_{0}	Absolute angular velocity of the shock block.
ω_{t}	Average angular velocity of the mandrel.
ω_{a}	Additional angular velocity of the shock block.
$\widetilde{\omega_{r}}$	Error of motor angular velocity.

LIST OF REFERENCES

[1] F Abolqasemi-Kharanaq, R Alipour-Sarabi, Z Nasiri-Gheidari, and F Tootoonchian. Magnetic equivalent circuit model for wound rotor resolver without rotary transformer's core. *IEEE Sensors Journal*, 2018.

[2] Kukhyun Ahn, Alparslan Emrah Bayrak, and Panos Y Papalambros. Electric vehicle design optimization: Integration of a high-fidelity interior-permanent-magnet motor model. *IEEE Transactions on Vehicular Technology*, 64(9):3870–3877, 2015.

[3] Ahmed Al-Timimy, Mahir Al-Ani, Michele Degano, Paolo Giangrande, Chris Gerada, and Michael Galea. Influence of rotor endcaps on the electromagnetic performance of high-speed pm machine. *IET Electric Power Applications*, 2018.

[4] Raghu CS Babu Angara, Kirk Wei Hsu, Paul John Villar, and Nimitkumar K Sheth. Influence of soft magnetic material type in fixture components on the magnetization of bonded neo magnet and motor performance. *IEEE Transactions on Magnetics*, (99), 2018.

[5] Milad Niaz Azari, Mojtaba Mirsalim, Seyed Mehdi Abedi Pahnehkolaei, and Sajjad Mohammadi. Optimum design of a line-start permanent-magnet motor with slotted solid rotor using neural network and imperialist competitive algorithm. *IET Electric Power Applications*, 11(1):1–8, 2017.

[6] Todd D Batzel and Kwang Y Lee. Electric propulsion with sensorless permanent magnet synchronous motor: implementation and performance. *IEEE Transactions on Energy Conversion*, 20(3):575–583, 2005.

[7] Raouf Benlamine, Tahar Hamiti, and Franck Vangraefschepe. Design of 60 kw–35,000 rpm interior pm machine for automotive application. In *Optimization of Electrical and Electronic Equipment (OPTIM) & 2017 Intl Aegean Conference on Electrical Machines and Power Electronics (ACEMP), 2017 International Conference on*, pages 311–316. IEEE, 2017.

[8] Laurent Bertoni, Hamid Gualous, David Bouquain, Daniel Hissel, M-C Pera, and J-M Kauffmann. Hybrid auxiliary power unit (apu) for automotive applications. In *Vehicular Technology Conference, 2002. Proceedings. VTC 2002-Fall. 2002 IEEE 56th*, volume 3, pages 1840–1845. IEEE, 2002.

[9] Franck Betin, Gerard-Andre Capolino, Domenico Casadei, Basile Kawkabani, Radu Iustin Bojoi, Lennart Harnefors, Emil Levi, Leila Parsa, and Babak Fahimi. Trends in electrical machines control: Samples for classical, sensorless, and fault-tolerant techniques. *IEEE Industrial Electronics Magazine*, 8(2):43–55, 2014.

[10] Daniele C Brotto, Michael K Forster, Jason K Leh, and Wing W Lin. Controlled power fade for battery powered devices, June 30 2015. US Patent 9,071,069.

[11] Brad Bryant and Marian K Kazimierczuk. Modeling the closed-current loop of pwm boost dc-dc converters operating in ccm with peak current-mode control. *IEEE Transactions on Circuits and Systems I: Regular Papers*, 52(11):2404–2412, 2005.

[12] Brad Bryant and Marian K Kazimierczuk. Voltage loop of boost pwm dc-dc converters with peak current-mode control. *IEEE Transactions on Circuits and Systems I: Regular Papers*, 53(1):99–105, 2006.

[13] Massimo Caruso, Antonino Oscar Di Tommaso, Fabio Genduso, Rosario Miceli, and Giuseppe Ricco Galluzzo. A dsp-based resolver-to-digital converter for high-performance electrical drive applications. *IEEE Transactions on Industrial Electronics*, 63(7):4042–4051, 2016.

[14] JT Chen and ZQ Zhu. Winding configurations and optimal stator and rotor pole combination of flux-switching pm brushless ac machines. *IEEE Transactions on Energy Conversion*, 25(2):293–302, 2010.

[15] Junhua Chen, Jian Li, and Ronghai Qu. Analysis, modeling, and current trajectory control of magnetization state manipulation in variable-flux permanent magnet machines. *IEEE Transactions on Industrial Electronics*, 2018.

[16] Xiao Chen, Jiabin Wang, Bhaskar Sen, Panagiotis Lazari, and Tianfu Sun. A high-fidelity and computationally efficient model for interior permanent-magnet machines considering the magnetic saturation, spatial harmonics, and iron loss effect. *IEEE Trans. Industrial Electronics*, 62(7):4044–4055, 2015.

[17] Monica Chinchilla, Santiago Arnaltes, and Juan Carlos Burgos. Control of permanent-magnet generators applied to variable-speed wind-energy systems connected to the grid. *IEEE Transactions on energy conversion*, 21(1):130–135, 2006.

[18] Liang Cong, Hongyue Jin, Pete Fitsos, Timothy McIntyre, Yuehwern Yih, Fu Zhao, and John W Sutherland. Modeling the value recovery of rare earth permanent magnets at end-of-life. *Procedia CIRP*, 29(C), 2015.

[19] Aashish Dalal and Jordan Smith. Design and development of a plug-in auxiliary power unit for heavy duty vehicle applications and stationary vocational equipment. In *Vehicle Power and Propulsion Conference (VPPC), 2011 IEEE*, pages 1–5. IEEE, 2011.

[20] Mengmeng Du, Hoi Lee, and Jin Liu. A 5-mhz 91% peak-power-efficiency buck regulator with auto-selectable peak-and valley-current control. *IEEE Journal of Solid-State Circuits*, 46(8):1928–1939, 2011.

[21] Haibin Duan and Lu Gan. Orthogonal multi-objective chemical reaction optimization approach for the brushless dc motor design. *Synthesis*, 1:2, 2015.

[22] Mario J Duran and Federico Barrero. Recent advances in the design, modeling, and control of multiphase machines—part ii. *IEEE Transactions on Industrial Electronics*, 63(1):459–468, 2016.

[23] Jawad Faiz and H Nejadi-Koti. Demagnetization fault indexes in permanent magnet synchronous motors—an overview. *IEEE Transactions on Magnetics*, 52(4):1–11, 2016.

[24] Ying Fan, Chenxue Li, Weixia Zhu, Xiangyang Zhang, Li Zhang, and Ming Cheng. Stator winding interturn short-circuit faults severity detection controlled by ow-svpwm without cmv of a five-phase ftfscw-ipm. *IEEE Transactions on Industry Applications*, 53(1):194–202, 2017.

[25] Jian Feng, Kun Liu, and Qing Wang. Scheme based on buck-converter with three-phase h-bridge combinations for high-speed bldc motors in aerospace applications. *IET Electric Power Applications*, 12(3):405–414, 2017.

[26] Indra Ferdiansyah, Era Purwanto, and Novie Ayub Windarko. Fuzzy gain scheduling of pid (fgs-pid) for speed control three phase induction motor based on indirect field oriented control (ifoc). *EMITTER International Journal of Engineering Technology*, 4(2):237–258, 2016.

[27] Fabien Gabriel. High-frequency effects in modeling ac permanent-magnet machines. *IEEE Transactions on Industrial Electronics*, 62(1):62–69, 2015.

[28] Steven J Galioto, Patel B Reddy, Ayman M El-Refaie, and James P Alexander. Effect of magnet types on performance of high-speed spoke interior-permanent-magnet machines designed for traction applications. *IEEE Transactions on Industry Applications*, 51(3):2148–2160, 2015.

[29] Miguel García-Gracia, Miguel Angel Cova, Maria Teresa Villen, and Antonio Uson. Novel modular and retractable permanent magnet motor/generator for flywheel applications with reduced iron losses in stand-by mode. *IET Renewable Power Generation*, 8(5):551–557, 2014.

[30] Joel P Gegner and CQ Lee. Linear peak current mode control: A simple active power factor correction control technique for continuous conduction mode. In *Power Electronics*

Specialists Conference, 1996. PESC'96 Record., 27th Annual IEEE, volume 1, pages 196–202. IEEE, 1996.

[31] Jacek F Gieras, Rong-Jie Wang, and Maarten J Kamper. *Axial flux permanent magnet brushless machines*. Springer Science & Business Media, 2008.

[32] Taner Goktas, Mohsen Zafarani, and Bilal Akin. Discernment of broken magnet and static eccentricity faults in permanent magnet synchronous motors. *IEEE Transactions on Energy Conversion*, 31(2):578–587, 2016.

[33] Halil Gör and Erol Kurt. Preliminary studies of a new permanent magnet generator (pmg) with the axial and radial flux morphology. *international journal of hydrogen energy*, 41(17):7005–7018, 2016.

[34] P Grmela, M Mach, and V Hajek. Permanent magnet dc motor re-design by femm. In *Electrical Machines and Power Electronics and 2011 Electromotion Joint Conference (ACEMP), 2011 International Aegean Conference on*, pages 666–669. IEEE, 2011.

[35] O Gutfleisch, D Eckert, R Schäfer, KH Müller, and V Panchanathan. Magnetization processes in two different types of anisotropic, fully dense ndfeb hydrogenation, disproportionation, desorption, and recombination magnets. *Journal of Applied Physics*, 87(9):6119–6121, 2000.

[36] Oliver Gutfleisch, Matthew A Willard, Ekkes Brück, Christina H Chen, SG Sankar, and J Ping Liu. Magnetic materials and devices for the 21st century: stronger, lighter, and more energy efficient. *Advanced materials*, 23(7):821–842, 2011.

[37] Sara Hamidizadeh, Natheer Alatawneh, Richard R Chromik, and David A Lowther. Comparison of different demagnetization models of permanent magnet in machines for electric vehicle application. *IEEE Transactions on Magnetics*, 52(5):1–4, 2016.

[38] Chengyuan He and Thomas Wu. Design, analysis and experiment of a permanent magnet brushless dc motor for electric impact wrench. In *Electrical Machines (ICEM), 2016 XXII International Conference on*, pages 1591–1597. IEEE, 2016.

[39] Chengyuan He and Thomas Wu. Design and analysis of a v-type fractional-slots ipmsm with distributed winding for electric vehicles. In *Electrical Machines (ICEM), 2016 XXII International Conference on*, pages 1459–1465. IEEE, 2016.

[40] Chengyuan He and Thomas Wu. Permanent magnet brushless dc motor and mechanical structure design for the electric impact wrench system. *Energies*, 11(6):1360, 2018.

[41] Chengyuan He, Thomas Wu, Wei Wu, Louis Chow, Jon Harms, and Donald R Taylor. Design, analysis and experiment of a high efficiency permanent magnet truck alternator. In *Industrial Electronics Society, IECON 2017-43rd Annual Conference of the IEEE*, pages 1905–1910. IEEE, 2017.

[42] James R Hendershot and Timothy John Eastham Miller. *Design of brushless permanent-magnet machines*. Motor Design Books, 2010.

[43] Hui Huang, Yu-Sheng Hu, Yong Xiao, and Hang Lyu. Research of parameters and antidemagnetization of rare-earth-less permanent magnet-assisted synchronous reluctance motor. *IEEE Transactions on Magnetics*, 51(11):1–4, 2015.

[44] Ziyuan Huang, Jiancheng Fang, Xiquan Liu, and Bangcheng Han. Loss calculation and thermal analysis of rotors supported by active magnetic bearings for high-speed permanent-magnet electrical machines. *IEEE Transactions on Industrial Electronics*, 63(4):2027–2035, 2016.

[45] Andrea Roberto Insinga, Rasmus Bjørk, Anders Smith, and CRH Bahl. Globally optimal segmentation of permanent-magnet systems. *Physical Review Applied*, 5(6):064014, 2016.

[46] Seok-Myeong Jang, Han-Wook Cho, and Sang-Kyu Choi. Design and analysis of a high-speed brushless dc motor for centrifugal compressor. *IEEE Transactions on Magnetics*, 43(6):2573–2575, 2007.

[47] Praveen Joseph and Jaison Mathew. Review of current control strategies for a vector controlled three phase upf rectifier. In *Power, Instrumentation, Control and Computing (PICC), 2015 International Conference on*, pages 1–7. IEEE, 2015.

[48] M Kabisch, M Heuer, G Heideck, and ZA Styczynski. Energy management of vehicle electrical system with auxiliary power unit. In *Vehicle Power and Propulsion Conference, 2009. VPPC'09. IEEE*, pages 358–363. IEEE, 2009.

[49] YL Karnavas, ID Chasiotis, CD Korkas, and SK Amoutzidis. Modelling and multiobjective optimization analysis of a permanent magnet synchronous motor design. *International Journal of Numerical Modelling: Electronic Networks, Devices and Fields*, 30(6):e2232, 2017.

[50] H Katagiri, H Sano, K Semba, N Mimura, K Matsunaga, K Tani, and T Yamada. Fast calculation method of ac copper loss for high speed machines. In *Electrical Machines and Systems (ICEMS), 2016 19th International Conference on*, pages 1–6. IEEE, 2016.

[51] Helena A Khazdozian, Ravi L Hadimani, and David C Jiles. Development of rare earth free permanent magnet generator using halbach cylinder rotor design. *Renewable Energy*, 112:84–92, 2017.

[52] Dae-Woo Kim, Gyeong-Jae Park, Ji-Han Lee, Jong-Wook Kim, Yong-Jae Kim, and Sang-Yong Jung. Hybridization algorithm of fireworks optimization and generating set search for optimal design of ipmsm. *IEEE Transactions on Magnetics*, 53(6):1–4, 2017.

[53] Hong-seok Kim and Byung-il Kwon. Optimal design of motor shape and magnetisation direction to obtain vibration reduction and average torque improvement in ipm bldc motor. *IET Electric Power Applications*, 11(3):378–385, 2017.

[54] Hong-seok Kim, Yong-Min You, and Byung-Il Kwon. Rotor shape optimization of interior permanent magnet bldc motor according to magnetization direction. *IEEE Transactions on Magnetics*, 49(5):2193–2196, 2013.

[55] Kyung-Tae Kim, Kwang-Suk Kim, Sang-Moon Hwang, Tae-Jong Kim, and Yoong-Ho Jung. Comparison of magnetic forces for ipm and spm motor with rotor eccentricity. *IEEE Transactions on Magnetics*, 37(5):3448–3451, 2001.

[56] Seung-Wook Kim, Sun Young Park, and Junghyun Han. Magnetization dynamics for magnetic object interactions. *ACM Transactions on Graphics (TOG)*, 37(4):121, 2018.

[57] Jae-Sub Ko, Jung-Sik Choi, and Dong-Hwa Chung. Maximum torque control of an ipmsm drive using an adaptive learning fuzzy-neural network. *Journal of Power Electronics*, 12(3):468–476, 2012.

[58] Y Kono, T Sakakibara, CP Aoyama, C Hotta, MM Turnbull, CP Landee, and Y Takano. Field-induced quantum criticality and universal temperature dependence of the magnetization of a spin-1/2 heisenberg chain. *Physical review letters*, 114(3):037202, 2015.

[59] Nagaiyar Krishnamurthy and Chiranjib Kumar Gupta. *Extractive metallurgy of rare earths*. CRC press, 2015.

[60] Vikas Kumar, Prerna Gaur, and AP Mittal. Ann based self tuned pid like adaptive controller design for high performance pmsm position control. *Expert Systems with Applications*, 41(17):7995–8002, 2014.

[61] Andras Kuthi, Jason M Sanders, and Martin A Gundersen. Core and copper loss effects on the stepped impedance transmission line pulse generator. In *Power Modulator and High Voltage Conference (IPMHVC), 2016 IEEE International*, pages 22–25. IEEE, 2016.

[62] Yoon-Seok Lee, Kyung-Tae Kim, and Jin Hur. Finite-element analysis of the demagnetization of ipm-type bldc motor with stator turn fault. *IEEE transactions on magnetics*, 50(2):889–892, 2014.

[63] Dawei Li, Ronghai Qu, Jian Li, Linyuan Xiao, Leilei Wu, and Wei Xu. Analysis of torque capability and quality in vernier permanent-magnet machines. *IEEE transactions on industry applications*, 52(1):125–135, 2016.

[64] Haitao Li, Wenzhuo Li, and Hongliang Ren. Fault-tolerant inverter for high-speed low-inductance bldc drives in aerospace applications. *IEEE Transactions on Power Electronics*, 32(3):2452–2463, 2017.

[65] Silong Li, Yingjie Li, and Bulent Sarlioglu. Performance assessment of high-speed flux-switching permanent magnet machine using ferrite and rare earth permanent magnet materials. *Electric Power Components and Systems*, 43(6):711–720, 2015.

[66] Xiyuan Li, Shumei Cui, and Liwei Song. High-efficiency control strategy of an air-core pulsed alternator pair. *IEEE Transactions on Plasma Science*, 45(12):3342–3348, 2017.

[67] Feng Liang, John M Miller, and Xingyu Xu. A vehicle electric power generation system with improved output power and efficiency. *IEEE Transactions on Industry Applications*, 35(6):1341–1346, 1999.

[68] Dong-Kuk Lim, Kyung-Pyo Yi, Sang-Yong Jung, Hyun-Kyo Jung, and Jong-Suk Ro. Optimal design of an interior permanent magnet synchronous motor by using a new surrogate-assisted multi-objective optimization. *IEEE Transactions on Magnetics*, 51(11):1–4, 2015.

[69] Conggan Ma, Qing Li, Haifeng Lu, Yuewen Liu, and Haibo Gao. Analytical model for armature reaction of outer rotor brushless permanent magnet dc motor. *IET Electric Power Applications*, 12(5):651–657, 2018.

[70] Tatsuo Maetani, Shigeo Morimoto, Kichiro Yamamoto, Yoshinori Isomura, and Akihiko Watanabe. Comparing brushless dc motors: A method of suppressing the shaft voltage even in a grounded motor frame. *IEEE Industry Applications Magazine*, 21(6):29–35, 2015.

[71] Wound Radial-flux Halbach Permanent Magnet. Multi-objective optimal design of a toroidally wound radial-flux halbach permanent magnet array limited angle torque motor. *IEEE Transactions on Industrial Electronics*, 64(4), 2017.

[72] Charalampos Manolopoulos, Matteo F Iacchetti, Alexander C Smith, Paul M Tuohy, Xiaoze Pei, Mark Husband, and Paul Miller. Design of superconducting ac propulsion motors for hybrid electric aerospace. In *2018 AIAA/IEEE Electric Aircraft Technologies Symposium*, page 5000, 2018.

[73] Charalampos D Manolopoulos, Matteo F Iacchetti, Alexander C Smith, Kévin Berger, Mark Husband, and Paul Miller. Stator design and performance of superconducting motors for aerospace electric propulsion systems. *IEEE Transactions on Applied Superconductivity*, 28(4):1–5, 2018.

[74] Koki Matsushita. Development of a new mos rectifier for high-efficiency alternators. Technical report, SAE Technical Paper, 2017.

[75] Yasser Abdel-Rady Ibrahim Mohamed. Design and implementation of a robust current-control scheme for a pmsm vector drive with a simple adaptive disturbance observer. *IEEE transactions on industrial electronics*, 54(4):1981–1988, 2007.

[76] Mahmood H Nagrial, Jamal Rizk, and Ali Hellany. Design and performance of interior permanent magnet motors with saturating magnetic bridge. In *Electric Machines and Drives Conference, 2009. IEMDC'09. IEEE International*, pages 922–927. IEEE, 2009.

[77] Malakondaiah Naidu, Nady Boules, and Rassem Henry. A high-efficiency high-power-generation system for automobiles. *IEEE Transactions on Industry Applications*, 33(6):1535–1543, 1997.

[78] Reza Nasiri-Zarandi, Mojtaba Mirsalim, and Andrea Cavagnino. Analysis, optimization, and prototyping of a brushless dc limited-angle torque-motor with segmented rotor pole tip structure. *IEEE Transactions on Industrial Electronics*, 62(8):4985–4993, 2015.

[79] Feng Niu, Bingsen Wang, Andrew S Babel, Kui Li, and Elias G Strangas. Comparative evaluation of direct torque control strategies for permanent magnet synchronous machines. *IEEE Transactions on Power Electronics*, 31(2):1408–1424, 2016.

[80] Satoshi Ota and Yasushi Takemura. Evaluation of easy-axis dynamics in a magnetic fluid by measurement and analysis of the magnetization curve in an alternating magnetic field. *Applied Physics Express*, 10(8):085001, 2017.

[81] Jun-Kyu Park, Thusitha Randima Wellawatta, Zia Ullah, and Jin Hur. New equivalent circuit of the ipm-type bldc motor for calculation of shaft voltage by considering electric and magnetic fields. *IEEE Transactions on Industry Applications*, 52(5):3763–3771, 2016.

[82] Pragasen Pillay and Ramu Krishnan. Application characteristics of permanent magnet synchronous and brushless dc motors for servo drives. *IEEE Transactions on industry applications*, 27(5):986–996, 1991.

[83] Mariia Polikarpova, Pia Lindh, Chris Gerada, Marko Rilla, Ville Naumanen, and Juha Pyrhönen. Thermal effects of stator potting in an axial-flux permanent magnet synchronous generator. *Applied Thermal Engineering*, 75:421–429, 2015.

[84] Daniel Puzio, Robert J Opsitos, Robert G Kusmierski, Robert S Gehret, John Cox, Craig A Schell, Michael Haupt, and Joseph Kelleher. Quick release socket attachment for impact wrench, June 14 2016. US Patent 9,364,942.

[85] Juha Pyrhönen, Sami Ruoho, Janne Nerg, Martti Paju, Sampo Tuominen, Harri Kankaanpää, Raivo Stern, Aldo Boglietti, Nikita Uzhegov, et al. Hysteresis losses in sintered ndfeb permanent magnets in rotating electrical machines. *IEEE Transactions on Industrial Electronics*, 2015.

[86] Luís Carlos M Sales, Edilson P Pacheco, Luis Gustavo C Monteiro, Lícia G Souza, and Moises S Mota. Evaluation of the influence of an alternator with mechanical decoupling on energy consumption and co 2 emission in a flex fuel vehicle. Technical report, SAE Technical Paper, 2017.

[87] S Sashidhar and BG Fernandes. Braking torque due to cross magnetization in unsaturated ipm bldc machines and its mitigation. *IEEE Transactions on Magnetics*, 53(1):1–9, 2017.

[88] Hyun-Soo Seol, Dong-Woo Kang, Hyun-Woo Jun, Jongsuk Lim, and Ju Lee. Design of winding changeable bldc motor considering demagnetization in winding change section. *IEEE Transactions on Magnetics*, 53(11):1–5, 2017.

[89] Kyung-Hun Shin, Jang-Young Choi, and Han-Wook Cho. Characteristic analysis of interior permanent-magnet synchronous machine with fractional-slot concentrated winding considering nonlinear magnetic saturation. *IEEE Transactions on Applied Superconductivity*, 26(4):1–4, 2016.

[90] William Edward Simpkin and Donald R Wilson. High efficiency power generation system and system upgrades, November 24 2016. US Patent App. 15/225,571.

[91] Kevin W Smith, Thomas O Bales Jr, Matthew A Palmer, and Derek Dee Deville. Battery-powered hand-held ultrasonic surgical cautery cutting device, April 28 2015. US Patent 9,017,355.

[92] Jeffrey R Smithanik, Timothy A Harrris, Gregory W Smith, Udell So, and Eric B Mazzei. Angular position detector including a variable reluctance resolver-encoder, July 4 2017. US Patent 9,696,183.

[93] Tao Sun, Ji-Min Kim, Geun-Ho Lee, Jung-Pyo Hong, and Myung-Ryul Choi. Effect of pole and slot combination on noise and vibration in permanent magnet synchronous motor. *IEEE Transactions on magnetics*, 47(5):1038–1041, 2011.

[94] Ren Yuan Tang et al. Modern permanent magnet machines: Theory and design. *Beijing: Machine Industry Press*, 1997.

[95] Luca Tarisciotti, Pericle Zanchetta, Alan Watson, Jon C Clare, Marco Degano, and Stefano Bifaretti. Modulated model predictive control for a three-phase active rectifier. *IEEE Transactions on Industry Applications*, 51(2):1610–1620, 2015.

[96] Fengxiang Wang, Zhenbin Zhang, Xuezhu Mei, José Rodríguez, and Ralph Kennel. Advanced control strategies of induction machine: Field oriented control, direct torque control and model predictive control. *Energies*, 11(1):120, 2018.

[97] Ruili Wang, Patarachai Chevathamanon, and László Farkas. Sensorless adaptive field-oriented control schemes on asynchronous machine: A comparative study. In *Intelligent Human-Machine Systems and Cybernetics (IHMSC), 2016 8th International Conference on*, volume 1, pages 468–471. IEEE, 2016.

[98] Xinghua Wang, Qingfu Li, Shuhong Wang, and Qunfeng Li. Analytical calculation of air-gap magnetic field distribution and instantaneous characteristics of brushless dc motors. *IEEE Transactions on Energy Conversion*, 18(3):424–432, 2003.

[99] Y Wang, JH Feng, SY Guo, YF Li, ZC Chen, and ZQ Zhu. Investigation of optimal split ratio for high-speed permanent-magnet brushless machines. *IEEE Transactions on Magnetics*, (99):1–5, 2018.

[100] Zheng Wang, Jian Chen, Ming Cheng, and KT Chau. Field-oriented control and direct torque control for paralleled vsis fed pmsm drives with variable switching frequencies. *IEEE Transactions on Power Electronics*, 31(3):2417–2428, 2016.

[101] Achmad Widodo and Bo-Suk Yang. Application of nonlinear feature extraction and support vector machines for fault diagnosis of induction motors. *Expert Systems with Applications*, 33(1):241–250, 2007.

[102] Miroslaw Wlas, Zbigniew Krzeminski, and Hamid A Toliyat. Neural-network-based parameter estimations of induction motors. *IEEE Transactions on Industrial Electronics*, 55(4):1783–1794, 2008.

[103] Rafal Wrobel, Daniel E Salt, Antonio Griffo, Nick Simpson, and Phil H Mellor. Derivation and scaling of ac copper loss in thermal modeling of electrical machines. *IEEE Transactions on Industrial Electronics*, 61(8):4412–4420, 2014.

[104] Shuai Wu, Xiangyu Zhao, Chunfang Li, Zongxia Jiao, and Fengyu Qu. Multiobjective optimization of a hollow plunger type solenoid for high speed on/off valve. *IEEE Transactions on Industrial Electronics*, 65(4):3115–3124, 2018.

[105] Xiaopeng Wu, Chengning Zhang, Yupu Wang, Dongyu Gang, Weiguang Zhu, and Liwen Pan. The electromagnetic losses analysis of surface-mounted brushless ac pm machine driven by pwm. In *Transportation Electrification Asia-Pacific (ITEC Asia-Pacific), 2014 IEEE Conference and Expo*, pages 1–4. IEEE, 2014.

[106] Li Yu, Zhuoran Zhang, Zhihui Chen, and Yangguang Yan. Analysis and verification of the doubly salient brushless dc generator for automobile auxiliary power unit application. *IEEE Transactions on Industrial Electronics*, 61(12):6655–6663, 2014.

[107] Zhiyong Zeng, Weiyi Zheng, and Rongxiang Zhao. Space-vector-based hybrid pwm strategy for reduced dc-link capacitor current stress in the postfault grid-connected three-phase rectifier. *IEEE Transactions on Industrial Electronics*, 63(8):4989–5000, 2016.

[108] Dongdong Zhang, Tianhao Liu, Chengyuan He, and Thomas Wu. A new 2-d multi-slice time-stepping finite element method and its application in analyzing the transient characteristics of induction motors under symmetrical sag conditions. *IEEE Access*, 6:47036–47046, 2018.

[109] Fengge Zhang, Guanghui Du, Tianyu Wang, Fengxiang Wang, Wenping Cao, and James L Kirtley. Electromagnetic design and loss calculations of a 1.12-mw high-speed permanent-magnet motor for compressor applications. *IEEE Transactions on Energy Conversion*, 31(1):132–140, 2016.

[110] Pinjia Zhang, Yi Du, Thomas G Habetler, and Bin Lu. A survey of condition monitoring and protection methods for medium-voltage induction motors. *IEEE Transactions on Industry Applications*, 47(1):34–46, 2011.

[111] Yu Zhou, Huaishu Li, Guangwei Meng, Shi Zhou, and Qing Cao. Analytical calculation of magnetic field and cogging torque in surface-mounted permanent-magnet machines accounting for any eccentric rotor shape. *IEEE transactions on industrial electronics*, 62(6):3438–3447, 2015.

[112] Yu Zou and Jiangbiao He. Comprehensive modeling, simulation and experimental validation of permanent magnet synchronous generator wind power system. In *Industrial and Commercial Power Systems Technical Conference (I&CPS), 2016 IEEE/IAS 52nd*, pages 1–9. IEEE, 2016.